



OCEAN ENGINEERING
TEXAS A&M UNIVERSITY

Deep-Draft Vessel Wake and Wind Wave Hydrodynamics Near a Mixed-Sediment Embankment in Galveston Bay, Texas

Final Report

Prepared by

Jens Figlus and William P. Fuller

Department of Ocean Engineering

Texas A&M University (TAMU) / Texas A&M Engineering Experiment Station (TEES)
Galveston, TX 77553

Prepared for

U. S. Army Corps of Engineers – Galveston District (SWG) with funding provided under Cooperative Ecosystem Studies Unit (CESU) agreement No. W912HZ-17-2-0023: “In-Situ Measurements of Physical Forces and Biological Parameters in Coastal and Estuarine Systems, Galveston District.”

June 2019

Abstract

Vessel-generated wake waves are well-documented sources for a substantial amount of the energy impacting shorelines and embankments lining shipping channels. An approximately year-long study was conducted in Galveston Bay, Texas adjacent to the Houston Ship Channel, one of the busiest commercial navigation lanes in the United States. Hydrodynamic data measurements were collected at two research platforms just offshore of a beneficial-use mixed sediment dike approximately one kilometer eastward of the ship channel. Collected data were analyzed for correlations with vessel traffic information, thereby providing direct associations between the observed wake effects and the specific deep-draft vessel inducing the wake event. Hydrodynamic data were then analyzed through time-localizing signal analysis techniques known as wavelet transforms to obtain energy budgets. Wavelet transforms facilitate the use of time-frequency domain transformations on nonstationary data (i.e., hydrodynamic bursts containing vessel wake signatures). Time-localizing abilities are the major shortcoming to the standard signal-analysis techniques utilizing Fourier-based transformations. Results of this study provide a better understanding of the wind wave and ship wake energy impacting the field site and allow more precise numerical modeling of wind wave and ship wake impacts in shallow bay systems in the future.

The contents of this report have been adapted from the M.Sc. thesis proposal document with the same title written by William P. Fuller.

Highlights

- A year-long hydrodynamic study was conducted about a kilometer east of a heavily-trafficked deep-draft navigation channel in Galveston Bay, Texas.
- Automatic identification system (AIS) recorded vessel parameters and vessel-induced wake energy measured at the field site were correlated; wake events from inbound vessels presented the strongest correlations including an $R^2 = 0.25$ between hull length and significant wave height, $R^2 = 0.37$ between hull length and maximum cross-shore velocity magnitude, and $R^2 = 0.30$ between vessel deadweight tonnage weight and maximum cross-shore velocity magnitude.
- Vessel wake-generated energy levels were contrasted with fetch-limited wind wave energy levels during calm and windy conditions. Inbound vessel wakes were the leading source for measured energy at the site, reinforcing the importance of vessel traffic considerations during embankment design.

Table of Contents

1. Introduction	11
1.1. Background	11
1.2. Motivation	12
1.3. Literature Review	13
1.3.1. Vessel Wakes	13
1.3.2. Wavelet Analysis	23
1.4. Environmental Considerations	33
2. Research Questions	37
3. Field Site	38
3.1. General Information	38
3.1.1. Geography	38
3.1.2. Vessel Traffic	40
3.1.3. Meteorological Setting	40
3.1.4. Tidal Hydrodynamics	41
3.2. Instrumentation	42
3.2.1. Platform Configuration	42
3.2.2. Acoustic Doppler Current Profiler Operation	43
3.2.3. Data Availability	46
3.3. Measured In-Situ Conditions	47
3.3.1. Wind	47
3.3.2. Hydrodynamics	54
3.3.3. Vessel Traffic	55
4. Methodology	62
4.1. Data Quality Assurance and Control	62
4.1.1. General	62
4.1.2. Velocity Data Processing	62
4.1.3. Pressure Data Processing	65
4.2. Wake Identification	66
4.2.1. Decision Algorithm Overview	66
4.2.2. Multiresolution Analysis	67
4.2.3. Burst Hydrodynamic Statistics	69
4.2.4. Mid Frequency Bin Alignments	72
4.2.5. High Frequency Bin Moving Variance	74
4.2.6. Windowed Max Displacement of Water Surface Elevations	74
4.2.7. Velocity Component Span Approach	75
4.2.8. Decision Synthesis	83
5. Results and Discussion	85
5.1. Wake Hydrodynamics of the Two Transit Directions	85
5.1.1. Inbound	85
5.1.2. Outbound	89
5.1.3. General Discussion	93

5.2.	Correlating AIS Vessel Data with Observed Wake Characteristics	95
5.2.1.	Vessel Length	96
5.2.2.	Vessel Draft.....	96
5.2.3.	Vessel Summer Deadweight Tonnage	97
5.2.4.	Froude Numbers	98
5.2.5.	General Discussion – Research Question 1.....	100
5.3.	Determining Wave-Condition Contributions Towards the Total Energy Budget.....	101
5.3.1.	Wave Conditions Normalized as Max Total Energy Per Minute.....	101
5.3.2.	General Discussion – Research Question 2.....	103
6.	<i>Acknowledgments</i>	104
7.	<i>References</i>	105

Table of Figures

Figure 1.1: Orbital fluid motions induced by wave propagation under deep-water simplifications (left) and either transitional or shallow-conditions (right). Deep-water orbitals attenuate prior to reaching the bottom and thus have negligible bed impacts. Figure adapted from Chadwick (2017).....	15
Figure 1.2: Wave-field pattern generated by a vessel moving from left-to-right as described by Lord Kelvin [Thompson, 1887]. The respective oblique and stern-normal propagation directions for diverging and transverse waves are readily seen; the cusp-line interaction of the two wake components formed roughly 19.47° away from the bow is indicated by the dashed lines forming the outer reach of the wake field. Figure adapted from Torsvik et al. (2015)...	16
Figure 1.3: Bed shear stress magnitudes and directions as modeled by ERDC for a deep-draft vessel transiting the Houston Ship Channel inbound (i.e., from bottom to top of image). Figure adapted from Tate et. al (2008).....	22
Figure 1.4: The complex Morlet wavelet (ψ) partitioned into phase (i.e., imaginary) components in red and amplitude (i.e., real) components in black. The unmanipulated mother wavelet at a frequency of 0.85 is plotted in panel A; changes in wavelet frequency with dilation and translation each held constant are found in B1-2; changes in dilation with frequency and translation constant are shown in C1-2; the wavelet energy spectrum ($ \psi(f) ^2$) of the mother wavelet A is shown in D. Axis values for panels A, B1-2, and C1-2 are identical while the panel D axis values are found to the bottom and right. Figure modified from a similar figure in Addison (2017).	26
Figure 1.5: The Mexican hat wavelet undergoing transformations during signal analysis; positive and negative contribution explanations highlighted in the top panel (A) are shown during four distinct time point translations yielding strong positive (b_1), weak positive or negative (b_2), and strong negative (b_3 - b_4) values. Figure adapted from Addison (2017).	27
Figure 1.6: One iteration of additive decomposition from the algorithm used to synthesize the multiresolution analysis technique. An approximation of the variability in the original signal (A_j) attributable to forces existing in the frequency detail bin D_j is the result of a high-pass filter (G) convolved with the approximation for the signal function calculated in the previous bin (A_{j+1}). The filtered data then tosses every other point, leaving half the total number of points relative to the previous bin. Figure adapted from Mallat (1989a).	30
Figure 1.7: Three wavelet functions (ψ) (bottom three panels) along with their corresponding scaling functions (Φ) (top three panels) that were examined as potential wavelets for the multiresolution analysis performed in this proposal. During the discrete wavelet transform, the convolution of the wavelet function (ψ) and the data signal ($f(t)$) is scaled via multiplication of the scaling function (Φ).	32
Figure 3.1: Field site location in Galveston Bay, Texas, and photo of “Garfunkel” platform.	38
Figure 3.2: Topographic map of Texas overlaid with the delineated Galveston Bay watershed. Irrelevant waterways are neglected in this map.	39

Figure 3.3: Tidal elevation time series from March 09th – 28th, 2018 as recorded by NOAA Station #8771013 located at Eagles Point, TX. The datum is set to mean tide level (i.e., the arithmetic mean of mean high water and mean low water). Vertical red lines indicate the start of a new day.42

Figure 3.4: Platform and instrument schematic.....43

Figure 3.5: Photos of ADCP pressure transducer (black circle in left panel) and ADCP head with three velocity transducers (right panel).....44

Figure 3.6: Photo (left panel) and schematic (right panel) of platform section with ADCP mounting arm. The approximate ADCP control volume for burst measurements is indicated by the orange box.45

Figure 3.7: Illustration of how the maximum effective fetches were calculated for the irregular shoreline of Galveston Bay using the method recommended by ERDC (1977).48

Figure 3.8: Seasonal histograms of the wind direction at the site overlaid by the corresponding mean wind velocity for each directional bin. Values recorded by NOAA meteorological station MGPT2, located near Morgan’s Point, Texas.49

Figure 3.9: Average wind directions (panel A), maximum gust velocities (B), and mean sustained velocities (C) during the subset of bursts organized by measurement timestamp. Values recorded by NOAA meteorological station MGPT2, located near Morgan’s Point, Texas.52

Figure 3.10: Archived forecast from the morning of March 19th showing the arrival of a marine polar frontal system at the project site.....53

Figure 3.11: The maximum wind gust velocity (panel A), maximum sustained velocity (B), and mean sustained velocity (C) during each burst organized by wind direction. Values recorded by NOAA meteorological station MGPT2, located near Morgan’s Point, Texas.54

Figure 3.12: Wind rose styled plots of the wind (left) and current (right) measurements during the subset of bursts.....55

Figure 3.13: Schematic detailing the principles of AIS. Marine traffic control information can be observed passing between the vessels and shore-based station. Image adapted from IMO (2019).....56

Figure 3.14: Extents of AIS data collection.....57

Figure 3.15: Distribution of selected cargo and tanker vessel parameters.....59

Figure 3.16: Inbound transit photo of cargo vessel MSC Heidi taken by the camera mounted to platform Simon on July 28th, 2018 at 15:05 (top) and high-resolution image of the same vessel for reference (bottom).60

Figure 3.17: Outbound transit photo of tanker vessel Zaliv Baikal taken by the camera mounted to platform Simon on July 28th, 2018 at 14:55 (top) and high-resolution image of the same vessel for reference (bottom). The surface wake component of the event can be seen rounding the embankment as a white-capped broken wave.61

Figure 4.1: Histograms of the Easting, Northing, and Upward directed beam amplitude strengths of the ADCP during the first deployment (i.e., between November and December of 2017). 64

Figure 4.2: Illustration of ENU (i.e., white arrows) and uv (i.e., red arrows) axes orientations at the site. Each set of arrows originate at one of site platforms.65

Figure 4.3: Multiresolution analysis of a water surface elevation time series containing a vessel-generated wake event arriving just after 02:36.68

Figure 4.4: The decomposed signal regrouped into 3 main frequency bins. High frequency (panel D) now contains 1-8 second periods, mid frequency (C) contains 8-32 second periods, while the low (B) contains the remaining 32-256 second periods. Original detrended water surface elevation show on top (A).69

Figure 4.5: Statistical comparison of 10 bursts containing wake events (black), 10 wind-only bursts (blue), and 2 examples of bursts with unusually weak wake events (red). Summaries include total magnitude (panels D and G), maximum variance calculated from a 12-second moving window (E and H), kurtosis (F and I), and bin energies relative to the total energy of the entire signal (B and C).71

Figure 4.6: Alignments of the 5th, 6th, and 7th detail frequency bins for an arriving wake. Thin lines indicate troughs of at least 5% relative prominence, bold lines indicate trough alignments with potential linkage to a wake arrival event.73

Figure 4.7: Comparing the high frequency bin with the value of a 12-second moving variance window.74

Figure 4.8: A detrended and smoothed pressure signal with a clear VGW arrival (panel A) that has undergone a 90-second moving window max magnitude threshold exceedance inspection (panel B).75

Figure 4.9: Depiction of the velocity span approach where upward moving spans are green and downward spans blue.78

Figure 4.10: Visual representation for the various components of a vessel-generated wake event, notably the bow and stern portions. Figure adapted from Sorensen (1973).81

Figure 4.11: Outcome of the span merging and trimming process designed to identify periods of extended unidirectional velocity behavior. The connection point identified in the u component is noted as having been shifted backward during corrective analysis after initially appearing later than expected. The shift is observed by the mid-span location of the u component connection point (circled) instead of an end of span location as would normally be expected. The correction positions the u and v component connections within the necessary proximity to be considered a potential wake; the wake passes the inspection.82

Figure 5.1: Multiresolution analysis of a burst with an inbound wake event between 19:13-19:17. For comparison to quiescent conditions, a comparable timespan between 19:22-19:26 was selected.85

Figure 5.2: Wind rose styled plots of the quiescent wind-driven current (left) compared to the current resulting from an inbound wake event (right). Both hydrodynamic periods were recorded in the same 17-minute burst of ADCP data.....86

Figure 5.3: Wind rose styled plots of the current during the two main wake components, the low-frequency Bernoulli wave drawdown (left) and the high-frequency Havelock surface wave packet (right).....87

Figure 5.4: Multiresolution analysis of a burst with an outbound wake event between 16:33-16:38. For comparison to quiescent conditions, a comparable timespan between 16:27-16:32 was selected.....89

Figure 5.5: Wind rose styled plots of the quiescent wind-driven current (left) compared to the current resulting from an outbound wake event (right). Both hydrodynamic periods were recorded in the same 17-minute burst of ADCP data.....90

Figure 5.6: Wind rose styled plots of the current during the two main wake components, the low-frequency Bernoulli wave drawdown (left) and the high-frequency Havelock surface wave packet (right).....91

Figure 5.7: Numerical model output of a wake disturbance field for an inbound vessel defined using current velocities. The right half of the disturbance appears to lag behind the left half due to the influence of the adjacent boundary. Figure adapted from Tate et al. (2008).94

Figure 5.8: Correlations between the vessel length and hydrodynamic parameters total energy, significant wave height, max u velocity magnitude, and max v velocity magnitude (Panels A-D respectively). Inbound transits in red, outbound transits in black.....96

Figure 5.9: Correlations between the vessel draft and hydrodynamic parameters significant wave height, mean period of high frequency waves, max u velocity magnitude, and max v velocity magnitude (Panels A-D respectively). Inbound transits in red, outbound transits in black. ...97

Figure 5.10: Correlations between the vessel Summer Deadweight Tonnage and hydrodynamic parameters significant wave height, drawdown duration, max u velocity magnitude, and max v velocity magnitude (Panels A-D respectively). Inbound transits in red, outbound transits in black.....97

Figure 5.11: Dimensionless correlation between an empirical parameter gH/V^2 and 3 different Froude Number variants. The empirical parameter in the left column uses significant wave height while the right uses max wave height. Vessels organized by transit heading (red inbound, black outbound) and ship type (circles cargo, asterisks tanker).....98

Figure 5.12: R^2 regression results for the correlations between Froude numbers and empirical gH/V^2 parameter organized by vessel heading directions and vessel types. Regression attempts included 1st and 2nd degree exponential fits, a 2nd degree polynomial fit, and 1st and 2nd degree power function fits..... 100

Figure 5.13: The maximum amount of wave energy measured during wind only (black), inbound wake events (blue), and outbound wake events (red) using a 30-second window (top panel)

and 2-minute window (bottom panel). Wave energies are normalized into a per minute timescale.....102

Table of Tables

Table 1-1: Aspects of the project related to Engineering With Nature and corresponding beneficial effects.	13
Table 3-1: Details on frontal system types likely to impact the field site.....	40
Table 3-2: Platform instrumentation.	43
Table 3-3: Description of ADCP operation modes.	44
Table 3-4: Availability of quality-controlled data used in this report.....	46
Table 3-5: Distribution of binned seasonal wind directions normalized to frequency per bin degree.....	49
Table 3-6: Seasonal velocities (mean and maxima) in each directional bin grouping.	51
Table 3-7: Statistics of selected cargo and tanker vessel parameters	58
Table 4-1: Potential sources of faulty ADCP velocity data measurements and respective solutions.	63
Table 4-2: Comparison of 4 statistical measures for the combined high frequency bin using the minimum value for bursts with strong or weak wake events and the maximum value for bursts that are wind only.	71
Table 4-3: Comparison of 4 statistical measures for the combined mid frequency bin using the minimum value for bursts with strong or weak wake events and the maximum value for bursts that are wind only.	71
Table 4-4: Comparison of 4 statistical measures for the combined high frequency bin using the mean value for bursts with strong or weak wake events and the maximum value for bursts that are wind only.	72
Table 4-5: Comparison of 4 statistical measures for the combined mid frequency bin using the mean value for bursts with strong or weak wake events and the maximum value for bursts that are wind only.	72
Table 4-6: Three- and two-span test condition details.....	76
Table 4-7: Velocity component span connection details for the bow portion of wake events in each transit direction.	80
Table 5-1: Comparison of velocity statistics during and after (wind waves only) an inbound wake event.....	86

Table 5-2: Comparison of frequency of occurrence and mean direction per velocity bin during and after (wind waves only) an inbound wake event.....	87
Table 5-3: Comparison of velocity statistics between the low frequency drawdown and high frequency surface wave components of the inbound wake event.	88
Table 5-4: Comparison of frequency of occurrence and mean direction per velocity bin during the low frequency drawdown and high frequency surface wave component of an inbound wake event.....	88
Table 5-5: Comparison of velocity statistics during and after (wind waves only) an outbound wake event.....	90
Table 5-6: Comparison of frequency of occurrence and mean direction per velocity bin during and after (wind waves only) an outbound wake event.	91
Table 5-7: Comparison of velocity statistics between the low frequency drawdown and high frequency surface wave components of the outbound wake event. Each component “Difference” row is relative to the quiescent, wind-driven conditions.	92
Table 5-8: Comparison of frequency of occurrence and mean direction per velocity bin during the low frequency drawdown and high frequency surface wave component of an outbound wake event. Each component “Difference” row is relative to the quiescent, wind-driven conditions.	92
Table 5-9: Best-fit regression results for the depth Froude number and empirical gH/V^2 parameter.	99
Table 5-10: Best-fit regression results for the length Froude number and empirical gH/V^2 parameter.	99
Table 5-11: Best-fit regression results for the modified Froude number and empirical gH/V^2 parameter.	99
Table 5-12: Summary of noteworthy correlations between vessel parameters and hydrodynamic statistics for wake events generated by inbound vessel transits.	101
Table 5-13: Summary of the maximum and average total wave energies found during full inbound and outbound wake events along with the maximum and average wave energy measured per inbound wake, outbound wake, and wind-only events using a 30-second and 2-minute window duration normalized into a per minute timescale.....	102

1. INTRODUCTION

1.1. Background

Contemporary studies estimate that the maritime transportation industry facilitates upwards of 80% of all international trade by volume [UN, 2017]. Societal reliance on the bulk carriers comprising the global fleet indicates these vessels will remain common throughout our local waterways and navigation channels into the foreseeable future. Along with the economic opportunities arising from these massive vessels are also several undesirable consequences. One of the main concerns is the inevitable generation of wake phenomena along shorelines and embankments.

The aim of this work is to advance our state-of-the-art coastal protection capabilities by providing novel insights on the impacts of vessel-generated wake (herein VGW) events along a beneficial-use mixed sediment dike placed adjacent to a deep-draft navigation channel in an enclosed shallow-bay. Novel additions to the broader VGW knowledgebase include:

Substantive correlation between the long-term marine traffic history and corresponding in-situ hydrodynamic data. Allocation of the field site's total energy budget into the constituent wave-energy sources including VGW waves, fetch-limited wind waves, and storm or frontal wind waves. Detailed analysis results of hydrodynamic measurements at the field site resulting from inbound and outbound deep-draft vessel motions utilizing wavelet transforms.

The research is structured around investigations into hypothesized links between VGW and corollary hydrodynamics. Vessel parameters considered during analysis range from hull shape and draft size to the recorded transit speed of the vessel at the point of wake generation. Wake hydrodynamics are quantified with statistics such as wave heights or wave periods along with relevant environmental conditions described in weather reports or water depths. The hydrodynamic statistics presented are the product of Fourier and wavelet analyses performed on recorded in-situ measurements. Essentially continuous hydrodynamic data collection occurred throughout the 11 months of field deployments spanning November of 2017 through October of 2018.

The overarching field research objective called for assessing the impacts of wind waves and VGW events around a recently constructed beneficial-use, mixed-sediment dike enclosing an incipient beneficial-use marsh. Encouraging dredgers to commit increasing amounts of extracted sediments to beneficial-use endeavors effectively limits the rate of wasteful dumping and therefore constitutes a favorite precept for the Engineering With Nature (herein EWN) initiative [ERDC, 2019]. The next section further explains the benefits realized from the adherence to EWN principles.

1.2. Motivation

A growing recognition that nature-centric engineering designs enjoy augmented long-term outcomes is steadily galvanizing the proliferation of EWN. By choosing to either work with - or actually employ - naturally occurring processes to attain project objectives, engineers are observing benefits ranging from cost savings due to less original construction and later maintenance efforts to engineered structures exhibiting longer lifespans. Principles both embraced by the EWN community and applicable to this project are tabulated in Table 1-1.

Researchers have lamented on the relative scarcity of long-term, real-world coastal hydrodynamic data for decades, particularly high-fidelity data exhibiting the distinct signatures of VGW phenomena [Herbich & Schiller, 1984; Velegrakis et al., 2006; Garel et al., 2008]. Successfully executing data collection thus furnished the first meaningful contribution by addressing longstanding in-situ VGW data deficiencies. The coalescence of the nearly year-long hydrodynamic measurement campaign into a vast data repository supporting the observations and conclusions of this study may be but the “tip of the iceberg” for the findings to be ultimately derived from this dataset.

Coastal Texas planners and engineers face a looming crisis instigated by the long-term exposure of GB to what we would consider today as substandard dredge material disposal and similar bed-use practices. This unsustainable past creates a future potentially lacking in the subaqueous space needed for local developmental or industrial needs. This issue is not necessarily unique to GB or Texas; any body of water experiencing extensive historical development is likely encountering such problems, especially if dredging operations use local areas as disposal grounds. Usage of these underwater spaces may involve laying new pipelines for the oil and gas industries common to Gulf states, installing new oyster reefs to combat water quality issues and attenuate wave energy while supporting the shellfish industry, or simply providing the open channels required for safe navigation around the waterbody. Embracing beneficial use endeavors for dredge material presents a viable method for aiming to ensure the long-term vitality of coastal environments.

Although beyond the scope of this report, a desirable goal is currently envisioned as taking the form of a robust sediment transport model specifically pertinent to closed coastal systems hosting large navigation or shipping channels. The model’s inclusion of parameters such as hull design, vessel transit speed, and local bathymetry would yield increasingly high-resolution estimations for sediment transport resulting from theoretical navigation scenarios [Tate et. al, 2008]. Short-term studies such as the high-resolution VGW example would allow researchers and scientists to glean fresh perspectives on the instantaneous mechanisms modulating vessel wake generation. The converse side to the short-term model is naturally a long-term variant, specifically one operating on multi-month to multi-year scales. Establishing novel linkages between observed hydrodynamics and the responsible marine traffic patterns (localized in both time and space, i.e., site-specific) would directly aid in long-term model formulations. Longevity models will likely attempt to resolve large-scale dynamics (such as those occurring across an

entire bay system) into small or local scaled effects such as shoreline erosion, increased water surface fluctuation variabilities, and habitat degradation rates.

Table 1-1: Aspects of the project related to Engineering With Nature and corresponding beneficial effects.

Feature	Phase	Effects	Impacts
Dredged Material Beneficial Use	Dike construction	Dike composed of mixed sediments dredged from HSC rather than hauling in rip-rap	Reduced rip-rap purchase and transport; reduced transport of dredged sediments to disposal site; increased on-station time of dredge
Dredged Material Beneficial Use	Wetland construction	Previous area low in biological value transformed into highly productive habitat	Habitat for migratory birds; new spawning grounds for bay fish supporting fishing and ecotourism industry; aesthetically pleasing
Avoids Hard-Armoring	Dike construction and erosion	Temporary protection for enclosed tidal marsh before naturally eroding	Incipient vegetation given chance to take root and grow while sheltered; dike erodes after several years, connecting the marsh to the Bay and forming open habitat supporting wildlife

1.3. Literature Review

The following subsections present a review of relevant literature for vessel wakes and their impacts on shallow bay environments. Additional focus is placed on the wavelet analysis technique for discontinuous timeseries of wind- and wake-generated wave hydrodynamics as this analysis forms an essential component of the presented work. Literature exploring the ecological impacts related to wind- and wake-waves in shallow bay systems is briefly introduced for completeness, with the understanding that the principal research thrust of this report is the hydrodynamic analysis of measured field data on wind waves and vessel wakes.

1.3.1. Vessel Wakes

Investigations into wake-related topics began with efforts to resolve experimental relationships between scaled models and the original object [Froude, 1874]. From these attempts came the realization of linkages between ship size, vessel speeds, and hydrodynamic resistance (associated with the wave-making tendencies of the fluid [Sorensen, 1973]), coined the Froude number when organized in equation form. The Froude number, a dimensionless ratio between inertial (ratio numerator) and gravitational (ratio denominator) forces, is frequently manipulated into slightly variant forms so as to best address the unique hydrodynamic flow-regime conditions to be investigated. Two basic forms of the Froude number are useful in vessel wake studies: the depth (1a) and vessel length (1b) formulations:

$$Fr_h = \frac{V_s}{(gh)^{0.5}} \quad (1a)$$

$$Fr_l = \frac{V_s}{(gl)^{0.5}} \quad (1b)$$

Wherein V_s is the velocity of the disturbance (i.e., ship), g is the gravitational acceleration, h is the water depth at the point of initial disturbance (i.e., navigation channel), and l is the disturbance length-scale (i.e., vessel hull length). Notably arising from (1a) is a form of the equation known as the depth-limiting Froude number. The equation's depth-limiting version is useful for approximating the threshold depth where orbital fluid motions created by propagating waves fail to interact with the seafloor – thereby providing quantitative justification for whether to employ depth-dependent simplifications as shown in Figure 1.1 [McConchie & Toleman, 2003; Torsvik et al., 2006]. Substituting the linear wave theory (herein LWT) depth-to-wavelength ratio (h/λ) threshold of no less than 0.5 in the depth Froude number transforms the equation such that along the vessel's sailing line:

$$Fr_h = \frac{V_s}{(gh)^{0.5}} = \frac{(g\lambda/2\pi)^{0.5}}{(gh)^{0.5}} = 0.56 \quad (1c)$$

At first glance, a logical conclusion to the (1c) result appears to be that deep-water assumptions are only viable for $Fr_h \leq 0.56$, however in practice this threshold is actually closer to 0.6 or 0.7 due to shallow water (i.e., refraction or diffraction) considerations [Weggel & Sorensen, 1984]. Hence, deviations of in-situ Froude behavior from the general theory often exist.

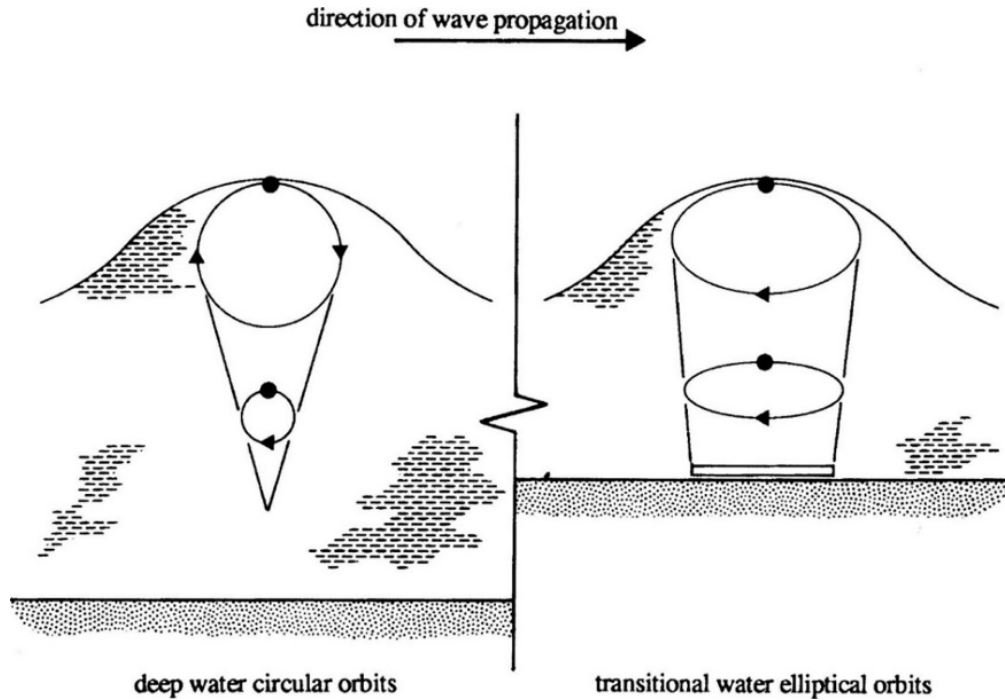


Figure 1.1: Orbital fluid motions induced by wave propagation under deep-water simplifications (left) and either transitional or shallow-conditions (right). Deep-water orbitals attenuate prior to reaching the bottom and thus have negligible bed impacts. Figure adapted from Chadwick (2017).

An additional form of the Froude number that further includes a coefficient summarizing the ship hull form, described as a “modified” Froude number [Kriebel & Seelig, 2005], has also proven useful in VGW analysis (1d):

$$Fr_m = Fr_l * \exp\left(\alpha \frac{d}{h}\right) \quad (1d)$$

$$\alpha = 2.35(1 - C_b) \quad (1e)$$

$$C_b = \frac{\nabla}{lbd} \quad (1f)$$

$$\nabla = \frac{w}{\rho} \quad (1g)$$

Wherein d is the vessel draft, α is the hull-form empirical coefficient, C_b is the block coefficient, ∇ is the vessel displacement, b is the vessel beam, w is the vessel weight (i.e., tonnage), and ρ is the water density. The block coefficient (1f) is commonly used during vessel-related

investigations as it aggregates the vessel length, width, draft, and weight into a single, comprehensive value.

After the successes of the 1874 scale-model experiments came the first investigation into wave-field formation by a deep-water point source [Froude, 1877]. The key distinction between short-period wake components moving either “forward and out” from, or “in the direction of” the generation source was presented for the first time – the former providing the basis for what are known as divergent waves while the latter as transverse waves (Figure 1.2).

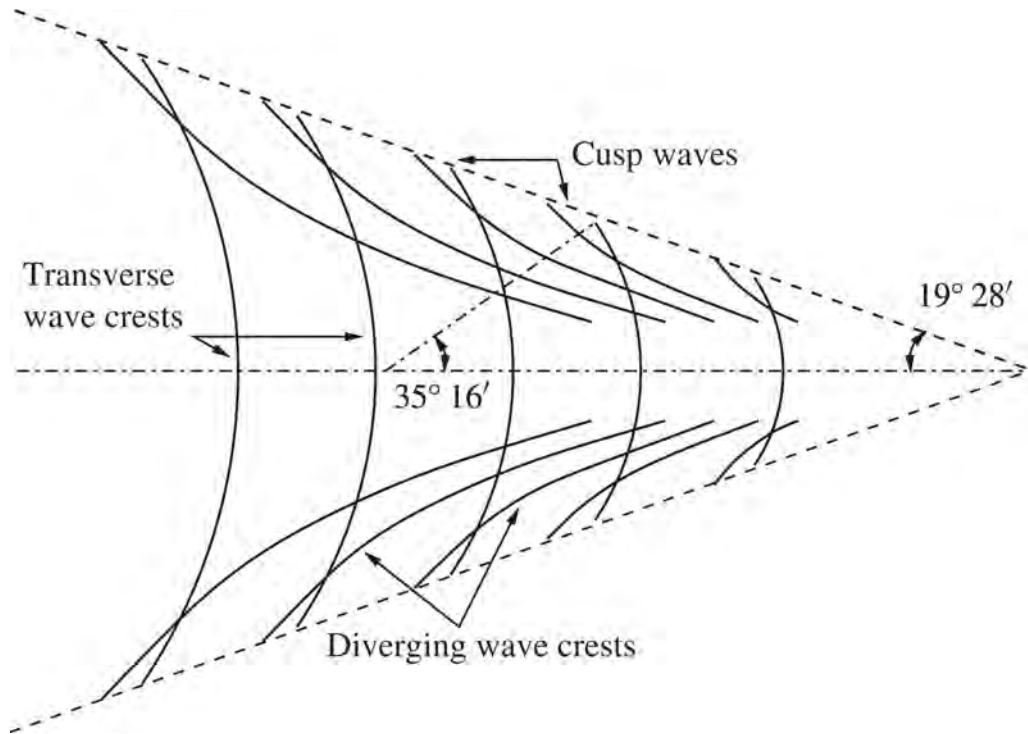


Figure 1.2: Wave-field pattern generated by a vessel moving from left-to-right as described by Lord Kelvin [Thomson, 1887]. The respective oblique and stern-normal propagation directions for diverging and transverse waves are readily seen; the cusp-line interaction of the two wake components formed roughly 19.47° away from the bow is indicated by the dashed lines forming the outer reach of the wake field. Figure adapted from Torsvik et al. (2015).

Thomson, known through his moniker Lord Kelvin, next introduced the seminal theory for articulating how wave fields introduced by Froude (1877) develop in conjuncture with a transiting vessel [Thomson, 1887]. This framework shed further light on bow-induced divergent and stern-induced transverse VGW waves, as well as describing the notion of an empirically definable cusp line. The two surface wake components and the cusp line eventually formed are sketched in Figure 1.2. Bearing no relation to the shoreline features having the same name, the cusps are understood to arise along the locations of interaction by the divergent and transverse waves. The delineation of where this cusp line will materialize can prove highly valuable during wave-energy investigations; the largest wave heights (i.e., energy transmissions) measured during wake events

generally spawn from superimposing waves along these cusps [Sorensen, 1973; Stumbo & Fox, 1998].

Although the Thomson (1887) wake theory sufficiently described much of the wake generation process, major deficiencies remained, especially when attempting to calculate cusp amplitudes. Inherent “mathematical limitations” in Lord Kelvin’s framework would translate into singularities cropping up during cusp-line amplitude calculations, precluding the maximum wave height calculations critical to engineering design [Sorensen, 1973]. Furthermore, as his methodology assumed constant depth, the VGW theory neglected the effects of water depths essential to wave-generation and propagation processes. Failing to include depth effects would not present an issue assuming only deep-water conditions were considered, however this is certainly not the case as depths grow shallower (Figure 1.1).

A solution for the drawbacks of Lord Kelvin’s theory came during attempts to resolve the wake generation process while only considering shallow water conditions [Havelock, 1908]. It was found that when generated in successively shallower (i.e., increasing Fr_h) conditions, the VGW response would be to proportionally shift the diverging wave propagation angle forward until a right-angle is formed with the sailing line. The empirical description for the deviation of the divergent wave away from Kelvin’s theory is found in (2a-b):

$$\cos^2(\alpha) = \frac{8(1 - \beta)}{(3 - \beta)^2} \quad (2a)$$

$$\beta = \frac{2kh}{\sinh(2kh)} \quad (2b)$$

Wherein α and k denote the divergent wave propagation angle away from the ship and LWT wavenumber, respectively. The creation of a right-angled diverging wave will only occur at a Fr_h ratio of unity, signifying the flow regime has jumped from subcritical to critical flow. An additional VGW response can be expected once the diverging bow-waves and sailing line reach orthogonality – physical limitations (as derived from LWT) that govern propagating waves have determined that while at a depth (h), a wave may not have a velocity surpassing the shallow water wave celerity $(g * h)^{0.5}$. This limiting threshold effectively defines the demarcation between trans-critical and critical flow regimes, as is quickly confirmed via the relation in (3):

$$C = C_g = (gh)^{0.5} \quad \forall h \mid Fr_h = 1 \quad (3)$$

Wherein C quantifies wave celerity, C_g the wave group velocity, and the qualifying notation is read as “for all depths (h) such that the depth Froude number equals unity.” Such flow regime transitions become especially pertinent during nonlinear vessel wake effect considerations; standing waves are one of several known nonlinear processes to potentially form along the

border separating a fluid body existing in multiple regime states [Torsvik & Soomere, 2008]. The majority of further detail discussing nonlinear VGW phenomena presented in this proposal are found in a later section.

While revising Lord Kelvin’s original deep-water VGW wave-field theory for the facilitation of shallow-water applications (i.e., Havelock wave-fields), Havelock managed to also formulate the approximation for VGW wave-amplitude decay rates while in deep-water conditions [Havelock, 1908]. He found that as a transverse VGW component propagates along the sailing line, but in the direction reverse to that of the source vessel, then wave amplitudes will exhibit an inversely proportional decay rate relative to the square-rooted distance that the wave has traveled from stern. This fundamental characteristic of deep-water VGW waves is readily validated using the wave energy equation derived from LWT (4):

$$E = \frac{\rho g H^2}{8} \lambda \quad (4)$$

Wherein E defines the average energy transmitted per unit wavelength λ and H defines the wave height (i.e., twice the amplitude). Equation 4 provides a common technique for quantifying the mechanical energy transferred by wind and VGW events onto local shorelines. Justification for employing (4) in lieu of other wave-energy equations is the inclusion of the wave height variable. Key energy flux parameters such as water depth and bed bathymetry intrinsically factor into the in-situ wave heights, and thus indirectly modulate the calculated energy value (4). The indirect inclusion of parameters known to be strong influencers in wave development and propagations should intuitively enhance the analysis’ robustness.

Sorensen (1973) is perhaps the earliest study to attempt identifying the variables associated with influencing VGW formations. A field investigation into the maximum VGW wave amplitudes observed after transits by relatively smaller vessels concluded that the vessel velocity and water depth parameters constituted the only factors significant in deciding wave amplitude evolution. Vessel hull-dimension parameters were explicitly noted as producing wave amplitudes with minimal variability while velocities and depths were held constant, regardless of how dissimilar the vessel sizes and shapes may have been. After the study attempted to search for the parameters controlling VGW wave periods, it was concluded that as with wave amplitudes, the vessel transit velocities and water depths were likewise filling significant roles during the formation process. Wave periods, however, would additionally respond to “the angle between the sailing line and the direction of advance of the wave at the point in question.” An equation then derived for theoretically estimating the dominant surface (i.e., transverse or diverging) wave period from a VGW event is given in (5a and 5b):

$$V_s \cos(\theta) = \left(\frac{gT}{2\pi}\right) \tanh\left(\frac{2\pi h}{V_s T \cos(\theta)}\right) \quad (5a)$$

$$V_s \cos(\theta) = \left(\frac{gT}{2\pi} \right) \quad (5b)$$

Wherein the left-hand-side is recognized as the phase velocity for the constituent waves contained in a wave packet and the right-hand-side is known to define the wave celerity for linearly simplified free-surface waves organized as a function of wavelength and water depth. Equation 5a is simplified to (5b) for shallow water conditions (6a-b):

$$kh \leq \frac{\pi}{10} \quad (6a)$$

$$\frac{h}{L} \leq \frac{1}{20} \quad (6b)$$

$$k = \frac{2\pi}{L} \quad (7)$$

Wherein k defines a hydrodynamic parameter known as the wave number.

Perhaps the first attempt at improving deep-draft ship wave design information initially investigated the dependence of ship wave characteristics on vessel design and operation parameters, followed-up by a revised iteration of preliminary results [Sorensen & Weggel, 1984; Sorensen & Weggel, 1986]. Results included a set of equations for use when VGW wave heights are desired when only the vessel's displacement and depth Froude numbers are known (8a-i):

$$\dot{H} = \dot{\alpha} \dot{x}^{\dot{n}} \quad (8a)$$

$$\dot{h} = \frac{h}{\gamma^{1/3}} \quad (8b)$$

$$\dot{n} = \beta \dot{h}^{\nabla} \quad (8c)$$

$$\beta = \begin{cases} -0.225 Fr_h^{-0.699}, & 0.20 \leq Fr_h \leq 0.55 \\ -0.342, & 0.55 \leq Fr_h \leq 0.8 \end{cases} \quad (8d)$$

$$\delta = \begin{cases} -0.118Fr_h^{-0.356}, & 0.20 \leq Fr_h \leq 0.55 \\ -0.146, & 0.55 \leq Fr_h \leq 0.8 \end{cases} \quad (8e)$$

$$\log(\dot{\alpha}) = \dot{a} + \dot{b} \log(\dot{h}) + \log^2(\dot{h}) \quad (8f)$$

$$\dot{a} = \frac{-0.6}{Fr_h} \quad (8g)$$

$$\dot{b} = 0.75Fr_h^{-1.125} \quad (8h)$$

$$\dot{c} = 2.6531Fr_h - 1.95 \quad (8i)$$

Wherein variables \dot{a} , \dot{b} , \dot{c} , $\dot{\alpha}$, β , δ , and \dot{n} define empirical coefficients and variables \dot{H} , \dot{x} , and \dot{h} define the dimensionless wave height, distance from sailing line, and water depth, respectively. Implied in the piecewise-defined inequalities bounding the acceptable range of depth Froude numbers (8d-e) is the caveat of this VGW wave-height estimation procedure only being intended for conditions where the depth Froude number remains between 0.2 and 0.8. Notably, a study using the same dataset to evaluate 9 various empirically-derived VGW wave height prediction models found that results calculated from the procedure listed in (8a-i) returned the most generalized-yet-accurate model for predicting VGW wave heights [Sorensen, 1997].

An erosion study completed along the Sabine-Neches Waterway in East Texas provides an early example of site-specific VGW investigations [Herbich & Schiller Jr., 1984]. Observations of surges as high as 3.5 meters (herein m) with durations lasting upwards of 20 minutes were reported in the narrow channel. Conclusions confirmed both long period waves as the dominant mode of vessel wake erosion and that surge heights formed as functions of the depth Froude number and vessel draft.

Upon discovering unexpectedly high sedimentation rates after widening (400 feet to 530 feet) and deepening (40 feet to 45 feet) the Houston Ship Channel (herein HSC) in 2005, the U.S. Army Corps of Engineers at the Engineering Research and Development Center (herein ERDC) completed a two-phased sedimentation study with site extents notably overlapping those of this thesis. Phase 1 began in 2006 with goals of determining the channel sedimentation rates pre- and post-enlargement, identifying the factors leading to the unexpected sedimentation, using data collection to update the 3D sedimentation model previously utilized for sedimentation rate predictions, and lastly re-running the updated model to investigate how much closer the predicted rate would be relative to the measured in-situ rate [Tate & Berger, 2006]. Of the factors listed as potentially affecting sedimentation rates, increases in vessel transit speeds through the enlarged channel altering near-channel erosion rates was identified as a primary concern. Erosion

rates were assumed to be dependent on the bed-level shear stresses via the current velocity initiated by the VGW drawdown and return surge. Equations (9a-c) were used to calculate the current velocity, bed-level shear stress, and corresponding erosion depth, respectively:

$$V_s A_c = (V_r + V_s) A_s \quad (9a)$$

$$\tau_b = \frac{1}{2} C_f \rho V^2 \quad (9b)$$

$$d_s = \frac{1}{\rho_s} \int_0^{t_p} K_e (\tau_b - \tau_{cr}) dt \quad (9c)$$

Wherein A_c defines the channel cross-sectional width, A_s the cross-sectional area of the ship at mid-length, V_r the velocity of the drawdown's return current, τ_b the bed-level shear stress, C_f the coefficient of friction, d_s the depth of erosion per vessel passage, t_p the time of passage as estimated by dividing the vessel length by its transit velocity, K_e the erosion rate, and τ_{cr} the critical shear stress. Both K_e and τ_{cr} are as estimated using Partheniades (1962). Solving (9a-c) for several ships indicated that reductions in erosion rates (d_s) due to the new vessel transit velocities post-channel enlargement would only increase deposition rates by roughly 5% [Tate & Berger, 2006]. Phase 2 of the study began in 2008 and primarily focused on validating the model updated in Phase 1 [Tate et. al, 2008]. Conclusions from the phase 2 model validation included determining that sediment suspension due to wind-wave action was not a primary driver of sediment transport, while vessel traffic was a primary driver. The confirmation of vessel impacts was found after modeling bed-level shear stresses caused by a vessel transit along the channel (Figure 1.3). The remaining discrepancy between the modeled sedimentation post-enlargement and the in-situ observations was theorized as possibly stemming from fluidized mud flowing into the channel.

Several researchers have specifically considered vessel wake issues through the scope of local ferry services. Most notable of the ferry studies, the original investigation into "no harm wash criteria" for the Puget Sound, first introduced the now widespread concept of wake limits. Consultant engineers were tasked with determining whether a new high-speed ferry was damaging local shorelines with generated wake events. Although finding no directly attributable shoreline damage over a six-week period, engineers determined that wakes generated at maximum operational speeds significantly contributed to the energy impacting the shoreline and over time would likely result in degradation. Considering this determination along with the observation that at reduced speeds of 11-12 knots the wake energy was essentially negligible, the consultant team established the concept of "no harm" wake wash at the 11-12 knot threshold for the site's depth [Stumbo & Fox, 1998]. The team also underscores a "no harm" wake speed for one site has no direct bearing on what the "no harm" wake speed should be for a different site.

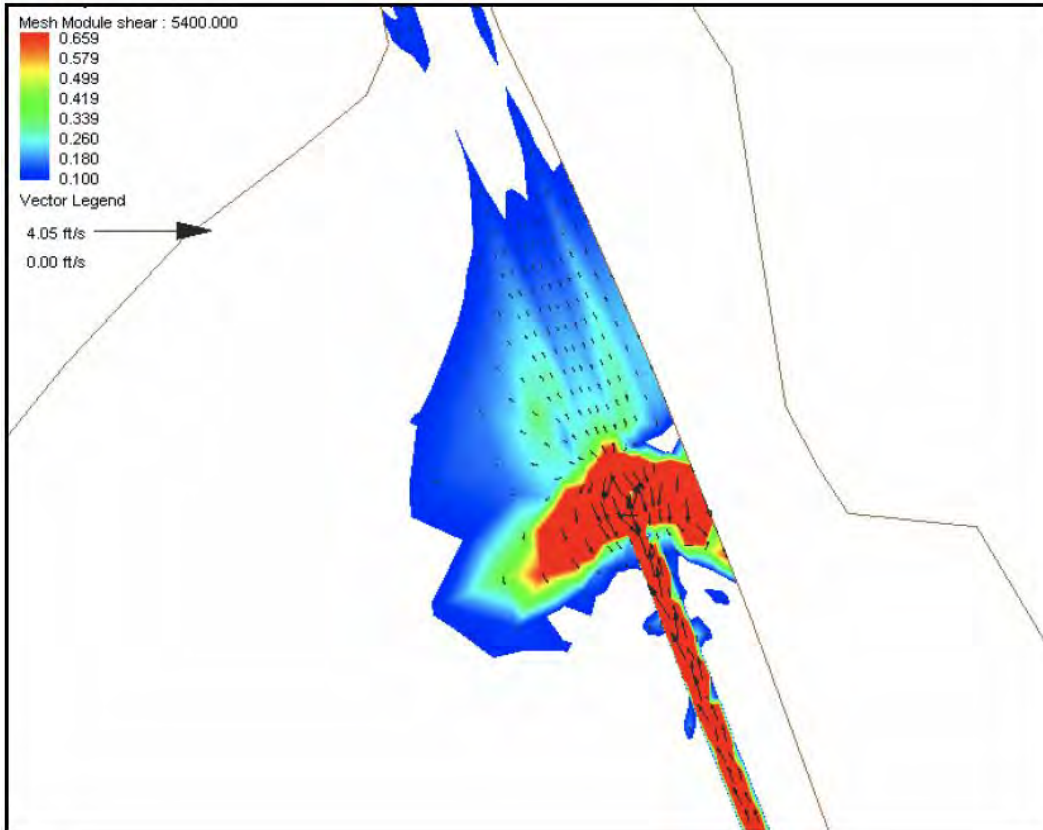


Figure 1.3: Bed shear stress magnitudes and directions as modeled by ERDC for a deep-draft vessel transiting the Houston Ship Channel inbound (i.e., from bottom to top of image). Figure adapted from Tate et. al (2008).

Additional instances of ferry-related studies are the wake comparisons between “slow” and “fast” ferries along a Greek microtidal beach [Velegrakis et al., 2006], simulated slow and fast ferry wake events for monitoring run-up effects [Erikson et al., 2004], sediment resuspension effects by ferry wakes in deep-draft, narrow channels [Garel et al., 2008], and directional-dependence of ferry wakes due to transitions in Froude regimes [Torsvik & Soomere, 2008]. From these studies, the potential for multiple wave packets to be generated from a single fast-moving wake event was confirmed, along with most high-speed ferry wakes having an intermediate grouping of wave periods of 7-10 seconds where most of the propagating energy was found to be concentrated.

A series of Alaskan studies began in the early 2000’s with an investigation into how design parameters for small, semi-planing boats (i.e., loading distribution, site basin geometry, distance from shore, hull type, and travel direction) affected VGW in a local river and lake [Maynard, 2001]. The study reported hull type as the vessel parameter most effective at sorting the groups of distinctly varying wave characteristics. Initial study results then provided the basis for developments in techniques to estimate wave heights of smaller semi-planing vessels [Maynard, 2005; Maynard, 2007].

One of the initial attempts to succeed in modeling VGW was tasked with investigating pressure field impacts resulting from deep-draft vessel navigation in the Corpus Christi Ship Channel [Fenical et al., 2001]. Validation of the model consisted of replicating the successive phases of water motions expected from a VGW, for instance ensuring the proper hydrodynamics occurred during drawdown, resultant surge, and during the arrival of the short-period wave groups. By coupling a pressure field distribution simulation with a numerical model of surfzone processes (i.e., wave transformation, runup, and overtopping), the researchers were able to satisfactorily reproduce expected shoreline hydrodynamic conditions during a VGW. Modifications to the model (i.e., deriving phase-averaged governing equations yet still solving in the time-domain) immediately followed the initial publication [Fenical et al., 2002]. With the newfound time-localization abilities the model was then able to predict low frequency drawdown and high frequency surface wakes with much better agreement to in-situ data.

Torsvik & Soomere (2008) note several key conclusions on complex nonlinear vessel wake processes, including how wakes generated during transitions from subcritical to supercritical Froude number regimes (and *vice versa*) differ from wakes wholly generated in subcritical regimes. How these regime transitions correlate to transit direction is further explored; outbound transits start slow and accelerate as leaving port while inbound transits start fast and decelerate as entering the Bay. Two additional publications detailing similar conclusions regarding nonlinear vessel wake topics will be mentioned: the first provides conclusions on discussions for limitations of LWT with respect to vessel wake generation, nonlinear wake phenomena examples (i.e., precursor soliton waves, wake envelope packets, and turbulence), and also superposition effects of long nonlinear waves in shallow conditions [Soomere, 2007]. The other article presents comparisons for how a varying Froude number (i.e., varying vessel accelerations and/or varying bathymetry) impact nonlinear wave amplitudes, how wave patterns are influenced by vessel accelerations or decelerations while near the critical Froude regime, and how nonlinear solitary waves can be captured by the pressure distribution field surrounding a moving vessel [Torsvik et al., 2006]. An exhaustive history of nonlinear VGW topics is presented in Soomere (2007).

The final VGW literature article of note presents the first major ERDC study incorporating AIS vessel data into methodologies. ERDC researchers proposed using AIS data to form a realistic VGW energy contribution model based on extrapolated local harbor traffic; the model would then be employed across the different options available for the Charleston Harbor deepening to help create the best-informed decision [Scully & McCartney, 2017]. Interestingly, the study concluded that the larger VGW heights induced by the new class of vessels was offset by the efficiency gains and effect on boats not changing size (but channel deepened hence lowering Froude number).

1.3.2. Wavelet Analysis

As with Fourier transforms (herein FT), wavelets transforms (herein WT) are time-to-frequency domain transformations packaged into two overarching varieties – continuous (CWT) and discrete (DWT) transforms. CWT operate as their name implies, continuously across an infinite

range of wavelet-modulating parameters to be discussed shortly. DWT instead consider transforms narrowly defined by a finite set of parameters. Consequently, CWT analyses are typical for when qualitative results are desired (i.e., high-resolution contour plots showing the temporal evolution of a signal across an infinite set of frequencies). When quantitative results are the end-goal (i.e., the temporal evolution of a signal contributed by a specific frequency), a DWT is then the tool of choice. Notably different than the infinitely continuous FT is the temporal localization possible by WT. Signals containing chirps, discontinuities, or otherwise nonstationary evolutions (such as VGW events) are by definition non-continuous and thus violate the assumption of a continuously stationary signal fundamental to Fourier-based methodologies. Both versions of the WT technically rely on two governing mathematical constructs, a mostly analogous initial wavelet function (ψ) and a wavelet size/shape modulating function (ϕ) that assumes slightly different behaviors depending on a continuous or discrete method of operation.

WT introductions begin with motivation and findings of seminal papers from J. Morlet and A. Grossman [Grossman & Morlet, 1984; Grossman et al., 1985; Grossman & Morlet, 1985]. These papers first propose the use of wavelets during a seismic trace analysis via first introducing the pair of fundamental dilation (a) and translation (b) parameters requisite for a CWT, respectively used to manipulate the scale of the wavelet resolution and to translate the wavelet along the time series temporally. Implementing the two manipulations was as simple as combining them with the index of each data point (t) into a single term and substituting the modified index for the original time point (10):

$$t = \frac{t - b}{a} \quad (10)$$

With the necessary wavelet modulations in place, the base, or “mother,” continuous Morlet wavelet function prior to modulation was derived (ψ ; 11a), along with the post-modulation version ($\psi_{a,b}$; 11b). The generalized form for a CWT function was then extrapolated from the Morlet wavelet and can be found in (12):

$$\psi(t) = \left(\frac{1}{\pi^{0.25}}\right) * \exp(i * 2\pi * f_0 * t) * \exp\left(\frac{-t^2}{2}\right) \quad (11a)$$

$$\psi\left(\frac{t - b}{a}\right) = \left(\frac{1}{\pi^{0.25}}\right) * \exp\left(i * 2\pi * f_0 * \frac{t - b}{a}\right) * \exp\left(\frac{-1^2}{2} * \frac{t - b}{a}\right) \quad (11b)$$

$$\psi_{a,b}(t) = \left(\frac{1}{\sqrt{a}}\right) * \psi * \left(\frac{t - b}{a}\right) \quad (12)$$

Wherein variables i , f_0 , and t , respectively, represent the imaginary unit, central mother wavelet frequency, and arbitrary time point. Mother wavelets define the initial, basic structure of the

wavelet function whereby all translated and dilated forms of the wavelet can be traced back to. Verbally, (11a) reads as the wavelet function at time t equates to the (wavelet-dependent) normalization factor multiplied by the mother wavelet and a Gaussian bell curve, each at time t (i.e., the Gaussian bounds the wavelet envelope) [Addison, 2017]. Resulting from the infinitely shrinking time steps assumed during the transform, the behavior of the shape modulation function ϕ for a CWT simplifies to a continuous vector of all real numbers bounded by the user-defined range of the dilation parameter (a). As will be seen shortly, the DWT equivalent of the scale function ϕ has no such simplification due to discretization of the constituent signal frequencies.

The Morlet wavelet is classified as an analytic function due to the complex nature of the sinusoidal term allowing for a selective analysis able to limit frequency considerations to sets of only positive components [Kaiser, 1994]. The choice between a real- or complex-valued function centers around the goal of the analysis; real-valued wavelets are useful for signals exhibiting sudden discontinuities while complex-valued wavelets specialize in relaying the phase and amplitude information for signals of a more steady, oscillatory nature [Farge, 1992]. Unlike their real-valued counterparts, complex functions such as the Morlet wavelet are often employed to examine both phase and amplitude information.

Figure 1.4 displays the complex Morlet wavelet in terms of the real (i.e., signal amplitude; black line) and imaginary (i.e., signal phase; red line) components for a mother wavelet (panel A) varying in frequency (B1), dilation (B2), or scale (C1-2). The energy spectrum of the wavelet in panel A is also plotted in panel D, resembling the Fourier spectrum but with relatively lower frequency resolution. The derivation of the wavelet energy spectrum (panel D) is given by (13):

$$|\hat{\psi}(f)|^2 = (2\pi^{0.5}) * \exp(-(2\pi * f - 2\pi * f_0)^2) \quad (13)$$

Wavelet spectra resulting from (13) similarly adheres to the statistical relationship described in Percival's Theorem (also mandatory to Fourier spectra) in that the variance of a signal process is equal to the integrated spectrum [Percival, 1995].

The loss in frequency resolution is a direct impact of temporal localizations. The time and frequency domain resolutions are governed by an implication of Heisenberg's Uncertainty Principle, effectively boiling down to any change to the resolution of one must be offset by an equal and opposite change to the other. The imaginary component is observed maintaining a one-quarter forward phase-shift relative to the real, behavior attributed to the normalization factor term forcing unit energy in the wavelet (11a) [Addison, 2017].

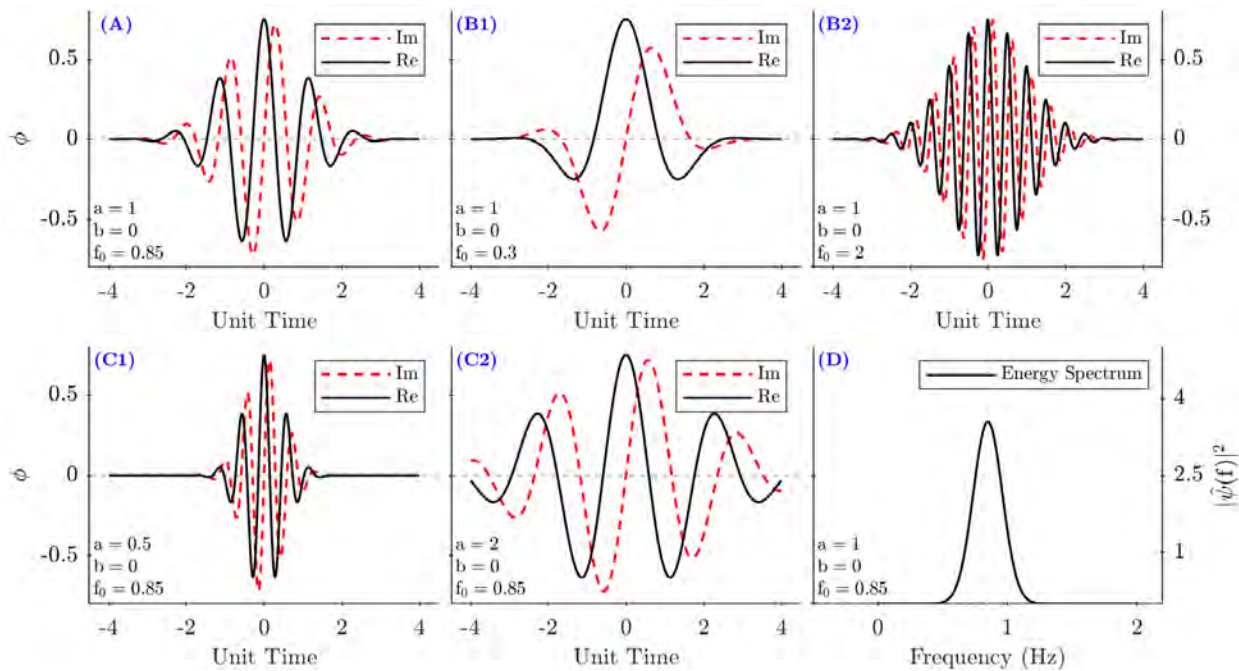


Figure 1.4: The complex Morlet wavelet (ψ) partitioned into phase (i.e., imaginary) components in red and amplitude (i.e., real) components in black. The unmanipulated mother wavelet at a frequency of 0.85 is plotted in panel A; changes in wavelet frequency with dilation and translation each held constant are found in B1-2; changes in dilation with frequency and translation constant are shown in C1-2; the wavelet energy spectrum ($|\hat{\psi}(f)|^2$) of the mother wavelet A is shown in D. Axis values for panels A, B1-2, and C1-2 are identical while the panel D axis values are found to the bottom and right. Figure modified from a similar figure in Addison (2017).

Further illustration of the fundamental WT operations is given in Figure 1.5. In the figure, an arbitrary signal (i.e., the water surface elevation for a fixed location) propagating through time is overlaid with an analyzing wavelet, in this case the Mexican hat wavelet. The upper panel (a) visually relates how the WT calculates quantitative values using translations and dilations; as the magnitude in wavelet translation increases the wavelet “slides” across the abscissa, while changes to the wavelet dilation magnitude control how the wavelet scales in size relative to the unaltered signal. Instances of strong positive or negative agreement between the wavelet and signal produce large values in the transformed wavelet coefficients, while strong disagreement then output large negative values.

The lower panel (b) focuses on the translation of the wavelet at a fixed dilation at four separate points in time (b_1 - b_4). The wavelet has strong agreement with the signal at b_1 , and thus a large positive value results from the WT. A rough split of the wavelet by the signal during a zero-upcrossing event at point b_2 yields a relatively small value after the split in agreement effectively cancels out for much of the wavelet. Disagreement between the wavelet and signal signs at all locations in b_3 coinciding with the mirrored concavity produces a large negative WT result. Lastly, another source of large negative values is given at b_4 due to sign disagreement at the wavelet edges and concavity disagreements at the wavelet maximum. The “continuous” in “continuous

wavelet transform” is justified at this step in the analysis – the lower panel in Figure 1.5 has just a single scale dilation with only 4 translations and would therefore yield just 4 data points; a CWT in theory yields an infinite number of dilations along an infinite number of translations.

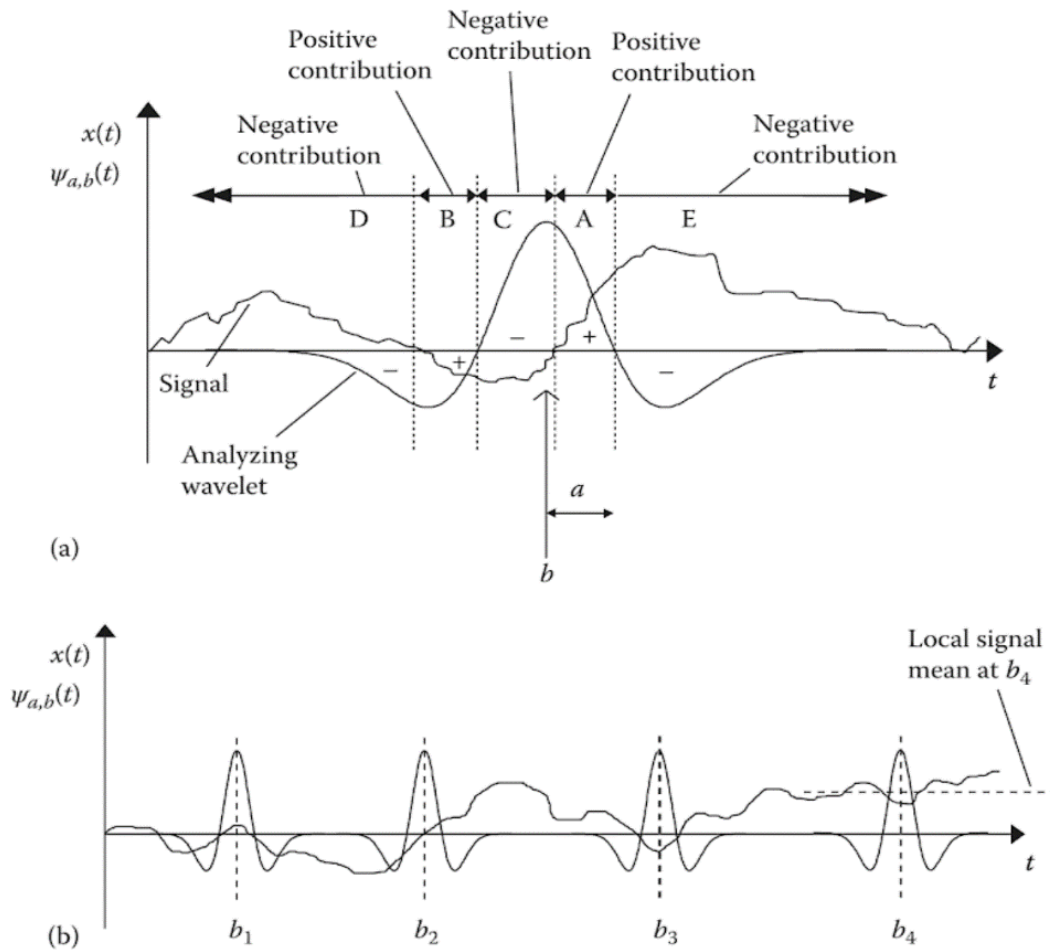


Figure 1.5: The Mexican hat wavelet undergoing transformations during signal analysis; positive and negative contribution explanations highlighted in the top panel (A) are shown during four distinct time point translations yielding strong positive (b_1), weak positive or negative (b_2), and strong negative (b_3 - b_4) values. Figure adapted from Addison (2017).

Further advancements for wavelet analysis took place with the advent of wavelet “frames” following the linkage of wavelet functions to preexisting linear algebra mapping constructs known as subspaces [Daubechies et al., 1986]. Essentially, when the components forming a signal are disaggregated (i.e., projected) into their relative contributions, the resulting components exist in the subspace created during the projection. The incredible mathematical power inherent to these subspaces rapidly facilitated new wavelet applications as researchers quickly realized the benefits of a narrowly defined set of orthonormal subspaces known as Hilbert space (\mathcal{H}) were now relevant to WT analyses. Although mostly beyond the scope of this proposal, an articulation

of the Hilbert space criteria is given in (14) as the orthonormality of H_u with respect to wavelets substantiates a key DWT technique central to this proposal.

$$H_u \equiv \{ f: \mathbb{R} \rightarrow \mathbf{C}: f \text{ is measurable and } \|f\|^2 \equiv \int_{-\infty}^{\infty} dt |f(t)|^2 < \infty \} \quad (14)$$

Which is read as when a set of numbers with individual points (t) potentially spanning all real numbers (\mathbb{R}), Hilbert subspaces (H_u ; i.e., orthonormal spaces) will:

- equate to functions (f) having a viable complex number (\mathbf{C}) for each point ($f(t)$)
- be measurable (i.e., finite)
- Have a squared inner-product (i.e., squared norm) ($\|f\|^2$) equal to the integration of the sampling increment (dt) multiplied by the absolute value of the sample magnitude of each point squared ($|f(t)|^2$) over all real numbers.

A set of values forming a coherent signal (i.e., water surface elevation timeseries) meeting the criteria required by Hilbert spaces (14) by definition has orthonormality [Daubechies, 1988]. In layman's terms, signals or data series meeting the requisite criterion above are effectively guaranteed to be decomposable into an arbitrary number of scaled subsets; these subsets represent the proportional contribution by the local forcing processes operating at the given scale of the overall signal at any given point in time. This translates to the water surface elevation measurements recorded by coastal researchers having the ability to be broken up into various ranges, or bins, that contain the energy imparted on the water surface by waves propagating at a period within the bounds of the particular bin.

Consequentially, these orthonormal bases would unlock the necessary proofs required for showing DWT could be performed with high fidelity signal decompositions. The basic wavelet function for a discrete wavelet is similar to that of a continuous wavelet, and is given in (15a):

$$\psi_{m,n}(t) = \left(\frac{1}{\sqrt{a_0^m}} \right) * \psi * \left(\frac{t - nb_0 a_0^m}{a_0^m} \right) \quad (15a)$$

Wherein m and n are both integers respectively controlling the dilation and translations, a_0 is a discretized dilation step (i.e., scale factor), and b_0 is the discretized spatial coordinate. Common protocols for selecting discretized values for a_0 and b_0 stem from the power of 2 composition of the DWT frequency subbands, whereby respective values of 2 and 1 are chosen to preserve logarithmic relationships. The updated form of the DWT general equation using a_0 and b_0 parameter values of 2 and 1 is provided in (15b):

$$\psi_{m,n}(t) = (2^{-m/2}) * \psi * ([2^{-m} * t] - n) \quad (15b)$$

As was mentioned in the WT introduction, the scaling function (ϕ) of a DWT is not simplified to unity as is possible with the CWT scaling function. Instead, the scaling function ($\phi(t)$) is presented

as a summation of all scaling equations derived during dilation and translation modulations of the original $\phi(t)$ (16):

$$\phi(t) = \sum_k c_k * \phi(2t - k) \quad (16)$$

Wherein “contracted versions” of the scaling function ($\phi(t)$) defines the $\phi(2t-k)$ term. These contracted versions have undergone translation manipulations at the interval step (k) according to the relative scaling coefficient (c_k). Addison (2017) notes that the implications from (16) confirm unique scaling functions at a certain scale can be derived from one or more scaling equations at the previous scale. This concept of a finite number of scaling equations (ϕ) superimposing to form the scaling function ($\phi(t)$) was first discovered by I. Daubechies in what she coined “compactly supported wavelets” [Daubechies, 1988].

Partitioning a non-stationary data series into orthonormal subsets was first accomplished shortly after I. Daubechies derived the first orthonormal wavelet functions and came in the form of the multiresolution analysis (herein MRA) [Mallat, 1989a; Mallat, 1989b; Meyer, 1989]. Derivations of the MRA algorithm employed to split the initial data series, a process referred to as “additive decomposition,” were first formed during an image processing application known as digital compression.

In the MRA, S. Mallat was able to prove that by setting bounded frequency filters increasing by sequential powers of 2 (i.e., octaves, or bins with either twice or half the frequency of adjacent bins), variations in the overall signal resulting from a specific octave (D_j) could be discerned and separated from the octave one scale coarser in resolution ($A_{2^{i+1}}$). The algorithm used for additive decomposition is given in Figure 1.6.

Considering both high-pass (\tilde{G}) and low-pass (\tilde{H}) filters are used to bound the frequency bins, each iteration of the algorithm effectively establishes a band-pass filter doubling in bin frequency range size (Figure 1.6). When the filters combining to form the band-pass are also “mirrors” of each other (i.e., in the sense that they are each half an octave away from the mean of the corresponding frequency bin), they are known as quadrature mirror filters [Mallat, 1989a]. Starting with the last (i.e., lowest resolution) frequency bin, the full signal ($f(t)$) undergoes the first decomposition beginning with the highest possible frequency; in most cases this frequency is determined by the sampling rate of the data.

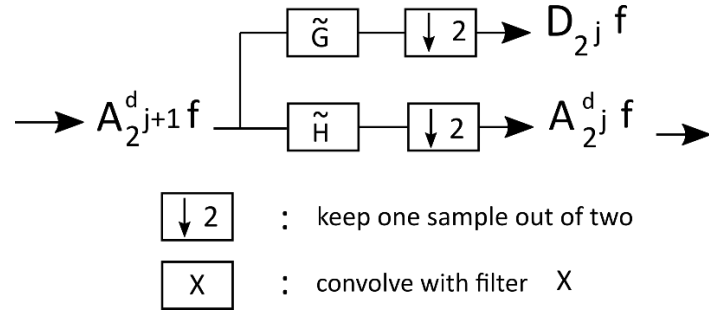


Figure 1.6: One iteration of additive decomposition from the algorithm used to synthesize the multiresolution analysis technique. An approximation of the variability in the original signal (A_j) attributable to forces existing in the frequency detail bin D_j is the result of a high-pass filter (\tilde{G}) convolved with the approximation for the signal function calculated in the previous bin (A_{j+1}). The filtered data then tosses every other point, leaving half the total number of points relative to the previous bin. Figure adapted from Mallat (1989a).

Data sampling rates that are powers of 2 allow for considerably simpler operations due to the quadrature nature of the bounding filters working more efficiently around octave expansions. In practice, this implies the highest viable frequency (i.e., the low-pass filter for the first detail bin) possible is given in (17-18):

$$\tau_j = 2^{j-1} , \quad j = 0, \dots, J \quad (17)$$

$$f_{max} = \tau_j * \Delta t , \quad j = 0, \dots, J \quad (18)$$

Wherein J defines the total number of frequency subbands, known as levels, to be calculated from the original signal ($f(t)$), j defines the index of the current iteration of the algorithm, τ_j scales the length of the j^{th} detail subband (i.e., number of data points), and Δt represents the sampling rate of the original data. Therefore, if an MRA of level 9 is performed for data collected by a 2 Hz sampling regime, the highest possible frequency in the first detail subband would be $2^{1-1} * 0.5$ or 0.5 seconds (i.e., the sampling frequency) while the lowest possible frequency in the final detail subband (i.e., level J) would be $2^{9-1} * 0.5 * 2$ or 256 seconds (doubled due to the low-pass filter doubling the high-pass). From there, the frequency thresholds sequentially increase by $2^j * 0.5$ seconds, giving the first three bands as between 0.5 through 1 second, 1 through 2 second, and 2 through 4 second periods, respectively.

Referring back to the algorithm (Figure 1.6) and coming full circle, each iteration j receives the resulting signal from the previous ($j+1$) detail band and determines a maximum allowed frequency (low-pass threshold) that is twice that of the previous band due to the length scale parameter increasing as an octave (18). In setting this maximum frequency, the algorithm removes any signal variations of the original signal due to lower order subbands (i.e., $j-1, -2, -3,$

..., $J-(J-1)$), thereby ensuring the only information remaining is per force corresponding to the current bandpass frequency range. This remaining data forms the orthonormal subset defined by (13) for all but the highest subband; the highest subband J first requires the second half of the quadrature mirror, namely the high-pass filter that sets the lowest allowable frequency for the current subband.

As the first iteration (i.e., subband J) enacts its high-pass filter, all information failing due to association with an undesirably low frequency is collected and stored in a $(J^{\text{th}}+1)$ dataset. For data series that did not undergo mean-value removal prior to the MRA (i.e., such that the inputted signal does not fluctuate around zero), any non-zero mean information is similarly dumped into this $J^{\text{th}}+1$ subband. Therefore, the $J^{\text{th}}+1$ subband basically acts as a catch-all for any signal variation information not included in the MRA. For a mean-extracted data series with a properly determined level size, this $J^{\text{th}}+1$ subband should be negligible; without a background mean value and any signal variation worth considering existing somewhere between the first and last subbands, there is no forgotten or leftover variation left to be collected.

All of the data failing the current low-pass threshold (i.e., insinuating relevance to a lower subband level) is aggregated into the leftover signal approximation dataset and passed along to the next subband iteration (i.e., to $j-1$). Now that both the high and low pass filters have activated, only level j data remains, representing the projection of the original signal ($f(t)$) onto the subspace of the j^{th} level as discussed with (14). The algorithm then repeats, until the final subband (i.e., the first level) is all that remains.

As was mentioned, the MRA was initially created for image processing, yet due to the orthonormal nature of the MRA bases or frequency subbands numerous applications are possible. Additional examples of early MRA implementations for signal processing topics include Percival & Mofjeld (1997) for ocean waves and Kumar & Foufoula-Georgiou (1997) for rainfall intensity.

A significant caveat for setting up an MRA involves the selection of the wavelet; three applicable wavelet functions (ψ ; panels A2-C2) with their appropriate scaling function (ϕ ; panels A1-C1) are plotted for comparison in Figure 1.7. Each of the three wavelet types (i.e., Daubechies Least Asymmetric (db4), Symlet (sym5), and Coifman (coif3) are energy preserving orthogonal wavelets with multiple forms identified by the numeric ending to the wavelet abbreviation. The numeric endings correspond to the number of vanishing moments the functions possess [MathWorks, 2019]. Of the myriad of potential orthogonal wavelets, these three were foremost chosen in recognition of their physical shape resembling that of a VGW event; wavelets better simulating the original signal ($f(t)$) will yield better MRA results as compared to those of greater variation (Figure 1.5). Additional rationale include the “db” wavelet sets concentrating their energy near the start of the support (i.e., the peak of the scaling function), “sym” wavelet sets having a nearly linear phase, and “coif” wavelet sets consisting of scaling functions ($\phi(t)$) nearly identical to the wavelet function ($\psi(t)$).

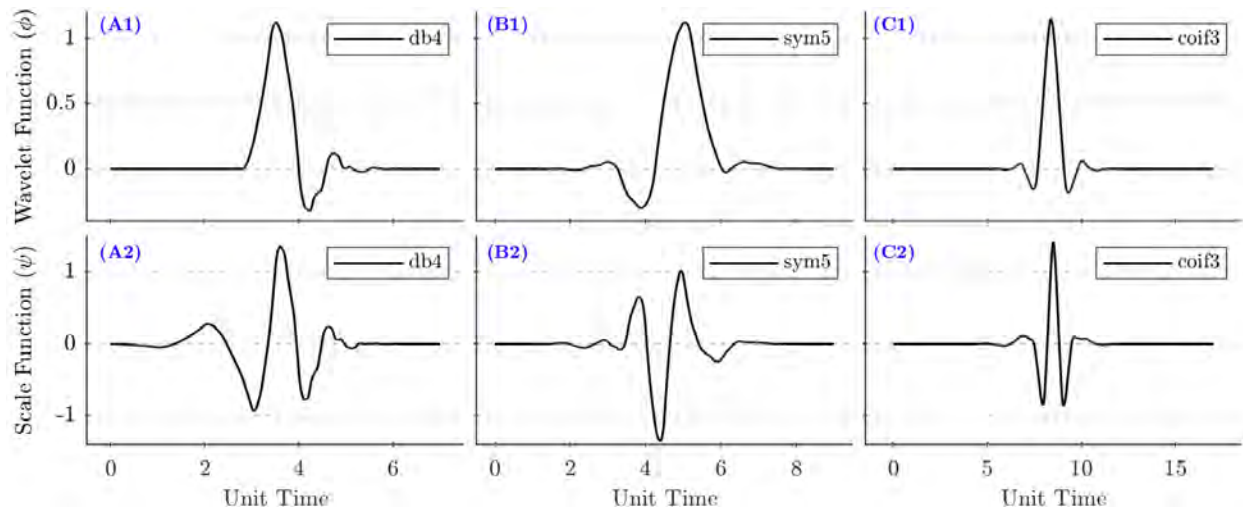


Figure 1.7: Three wavelet functions (ψ) (bottom three panels) along with their corresponding scaling functions (Φ) (top three panels) that were examined as potential wavelets for the multiresolution analysis performed in this proposal. During the discrete wavelet transform, the convolution of the wavelet function (ψ) and the data signal ($f(t)$) is scaled via multiplication of the scaling function (Φ).

After introducing wavelets and how they were constructed comes the developments leading to the acceptance of wavelet transforms as time-localized, invertible analogs to Fourier transforms of infinite periodicity. The first interpretations of wavelet coefficients as comparable to Fourier coefficients came from the last paper discussing wavelet transform bases before the final version of the bases were presented [Meyer, 1989]. Soon after Y. Meyer, Gamage & Hagelberg investigate the applicability of Parseval's theorem of signal variance in relation to the signal spectrum. They show that the power spectrum resulting from a local wavelet transform in fact constitutes a vertical slice of the entire global spectrum [Gamage & Hagelberg, 1990]. In a follow-up paper employing wavelets for the detection of microfront-related weather phenomena, the fact that an "ideal" choice of scaling and basis set for a wavelet exists and further can be deduced from a new method known as a covariance transform is presented [Gamage & Hagelberg, 1993]. Additional details on the findings are to be presented, including the discovery by the pair (and later discussion by others) that the main discrepancy between Fourier and wavelet transforms reside in how the basis function are supported; wavelet coefficients are impacted by local events as Fourier coefficients exhibit behaviors pervading the entire domain [Gamage & Hagelberg 1993; Farge, 1992; Kaiser, 1994].

Coincident to these explorations of Fourier and wavelet comparisons were the first investigations into the exact use of variance in wavelet transform analysis [Percival & Guttorp, 1994; Qiu & Meng, 1995; Percival, 1995; Percival & Mofjeld, 1997]. Percival (1995) defines decompositions of variance as a "measure of how much a weighted average of bandwidth of the process changes from one time period of bandwidth-length to the next." In the same paper he goes on to show that the "global" or complete spectrum is in fact an unbiased and consistent estimate of the true signal spectrum. Numerous findings directly impacting this thesis stemming from these three successive papers and another related paper investigating wavelet probabilities and statistical testing are to be presented [Torrence & Compo, 1998].

Wavelets and their application to directional information began with the same techniques employed during Fourier transforms [Donelan et al., 1985]. After steady growth in wavelet popularity the transition of directional techniques into the wavelet realm soon followed with the derivation of what was termed the “wavelet directional method” [Donelan et al., 1996; Donelan, 2002]. Results of the novel directional application indicated the dispersion of wave groups could be substantively captured with an array of paired wavestaff, along with providing the means for calculating newly discovered “wavenumber spectra.” Among the benefits to findings noted by the authors are the potentially life-saving impacts the increased knowledge in wave group dispersion can have for applications such as extreme value prediction [Donelan et al., 1996].

The final aspect to wavelets yet mentioned is their ability to comprise “packets.” Comparable to previously discussed quadrature mirror filters, wavelet packets can be summarized as essentially composing of “superpositioned wavelets described by short sequences of bounding linear operators” [Meyer, 1990; Coifman & Wickerhauser, 1992; Wickerhauser, 1993; Coifman et al., 1994]. The study of these wavelet packets coincidentally spurred developments of another useful wavelet tool: the technique of building a “codebook or library of predefined modulated waveforms” [Coifman & Wickerhauser, 1992]. Selection of the optimal wavelet basis from such a library was streamlined by the algorithm provided by Coifman et al., 1994).

1.4. Environmental Considerations

VGW are commonly linked with consequences palpable to local communities such as shoreline retreat and submerged aquatic vegetation destruction. Although less conspicuous than erosion or habitat loss, countless other effects with varying perceptibility are still readily observed. A comprehensive review of the pernicious VGW effects forced upon the many forms of life, habitat zones, and management practices relevant to coastal areas is assembled in Gabel et al., 2017).

From a review of marsh stability values for over 104 planted marshes in 12 states, wave climate parameters including fetch, shoreline configuration, and sediment grain size were found to be the only statistically related parameters to planting stability (i.e., roughly 30% of erosion variability attributed to these parameters alone) [Knutson et al., 1981]. Furthermore, it was found that wave stress constituted the principal factor in determining initial establishment and long-term stability rates. It was concluded that almost 85% of sites with mean grain-size values less than 0.4 mm were at least partially successful in planting while just over 80% of sites above 0.8 mm were complete failures. Additionally, no planting successes were observed if less than 20% of intertidal zone was vegetated, while areas with 60% or more intertidal vegetation experienced single-digit failure rates.

A separate review contrasting 14 dredged material marshes (anywhere from 1 to 23 years old) and 14 nearby natural “reference” marshes around Texas is initiated to try and identify general trends not apparent from smaller sample size comparisons and to also determine any linkages between the age of a placement site and various other attributes [Shafer & Streever, 2000].

Before starting the authors compile a well-rounded list of studies analyzing comparisons between different natural vs. dredged material marshes through the scope of various attributes. Paper concluded that many permanent protective structures installed on dredged material marsh projects are in reality overdesigned and overused to the detriment of the local wildlife and engineer's budget. The authors go on to note the benefits to silty-clay sediments for dredged-marsh placement projects, but also notes additional steps necessary in design stage if pumping high fine content due to even spreading of dredge outflow across the site. Notable difference between dredge material marshes vs natural are: 8/10 dredged marshes had ponds or tidal creeks missing while only 3/10 natural sites missing; significantly lower mean belowground biomass than natural (however this trend noted as disappearing with marsh age as settling processes increased biomass fraction and belowground biomass in dredged marshes shown to possibly exceed natural levels in less than 10 years after placement. Finally, the authors note implications of too large or overly permanent berm structures at dredge marsh sites. From 2000-2050, over 1700 hectares of salt marsh habitat creation expected for Galveston Bay.

To investigate the theorized existence of critical wave energy thresholds for long term marsh stability, wave climates across 8 natural and artificial wetland sites were contrasted [Shafer et al., 2003]. This paper notes that the wave height is often used as an indicator for energy studies as it is easily quantifiable, plus other relevant parameters can be folded into calculations for wave height. The main conclusion on estimating marsh stability is to use the 20th percentile exceedance wave height for the first threshold of stability approximation. Preliminary results further indicated stable marshes can be expected to emerge in wave climates of 20th percentile height exceedance of about 0.15 m, critical wave height values tended to remain between 0.15 m and 0.3 m, and a site's 20th percentile exceedance wave height dropped from 0.2 m to 0.13 m following the emergence of new vegetation. The conclusions agree with Shafer & Streever (2000) in that large structures are often overkill and discusses undesired consequences overly large structures cause. The final recommendation is presented that attenuation structures should be designed such that the peak elevation of the structure is near the elevation of the wetland sediment surface; a structure with a consistently subaerial top is unnecessarily high and should be avoided.

The unexpected blockage of a tidal creek by sediment transport associated with VGW approximately 5 kilometers (herein km) southwest of the current research site was examined from late 2005 into early 2006 [Ravens & Thomas, 2008]. Through investigations of a "siltation plug" formed in the creek, results pointed to VGW as largely culpable for the blockage event. Perhaps the strongest supporting evidence for this assertion was the finding of nearly identical median grain sizes (herein d_{50}) between the silt plug and sediments suspended by landward propagation of VGW wave crests. The study noted a precipitous rise in the rate of sediment transport as shallow depths became deeper, down to a depth of 0.6 m wherein the transport maxima was measured. It was then concluded that the most extreme transport rates would be found under already-broken VGW wave crests while at depths under 1 m. Three additional conclusions worth mentioning: friction velocity to fall velocity ratios above 5 were confirmed as indicating suspended wash load should dominate sediment transport processes (versus bedload), VGW bore heights inside the tidal creek significantly depended on the direction of the wave

packet propagation, and the sedimentary blockage of artificial tidal creeks designed to encourage circulation in artificial marshes are likely due to the erosion and subsequent transport of creek bank sediments by VGW wave events.

A three-year wave tank experiment into impacts of waves (mirroring site conditions of heavily trafficked ship channel) on bank stability in relation to emergent plant development agreed with Knutson et al., 1981) that wave stress was a severe constraint for vegetation development. Conclusion presented that vegetated profiles weren't greatly affected by 10 cm wave heights, but 23 cm wave heights were enough to completely "wash out" a plant species with minimal root systems and stem density [Coops et al., 1996]. The vegetation trends were noted as higher stem-density plants exhibiting the highest standing wave attenuation efficiencies, while lower density species hardly registered wave height changes from unvegetated control profiles. Emergent vegetations were noted as providing the most noticeable impact to erosion forces; sediment was both reinforced and waves were attenuated. A major caveat for comparing results in the paper to this thesis arise from grain size diameters – grain sizes were noted as playing a significant role in determining vegetation stability; the minimum study grain size was 0.16 mm while cohesive sediments are one or more orders of magnitude smaller.

Beginning with a reminder of why salt marshes are important to human society, the next paper attempts to resolve the effects of wave action on marsh boundaries as a function of tidal elevation across varying marsh edge configurations [Tonelli et al., 2010]. The fundamental forces noted as modulating salt marshes were: relative sea level rise, tidal regime, wave climate, sediment supply, and the presence of vegetation covers. Salt marsh evolution was noted to have a considerable relationship with the prevalence of boundary tidal flats due to links between marsh degradation and the erosion of marsh edges under natural wind waves. Conclusions include that maximum energy fluxes (i.e., erosive forces) occurred during tidal elevations such that wave crests rise to the top of the bank but stop rising before significant inundation and overtopping occur. Numerous microtidal environments were found to exist in the critical elevation range for maximizing boundary erosion, a trend confirmed by the measuring of marsh erosion conditions at peak magnitudes while the mean water level was around the marsh platform level. A notable diverging trend in marsh susceptibility found by the paper was that low-lying marshes are more likely to experience wave energy "thrusts" where wave breaking energies are transmitted directly into the bank and result in large chunks breaking off; high marshes are more likely to be affected by bottom shear stresses due to waves running across marsh. Lastly, it was concluded that wind-wave energies presented the dominant cause of salt marsh erosion, particularly in microtidal basins.

The final paper discussing ecological concepts presents a stark shift in the marsh vegetation paradigm when the presence of root-growing plants surprisingly made no statistically significant difference to the amount of erosion in the wave flume portion of the study [Feagin et al., 2009]. Even more unexpected was the finding that certain root presence may actually instigate increased erosion rates as waves "wiggle" plants and thus loosen the soil around the shifting roots. Erosion rates noted to reach max during draw down component of wave cycle, agreeing with experiences. Regarding marsh composition, restored marshes tended to contain higher

sediment fractions and less cohesive fine fraction relative to natural. This composition characteristic is key as conclusion provided that soil type was the lead factor in modulating lateral erosion in coastal wetlands. Bulk density further concluded as best indicator for erosion, but caveat raised that parameters including organic matter composition, water content, and coarse particle presence also determining predictors. Plants noted as naturally supplying organic matter to nearby soil which effectively lowers the bulk density due to organic matter having relatively light density. The detritus and finer grains accumulating around roots make sediment less dense, less coarse, and more cohesive. Relevant finding to this thesis indicates the percentage of silts/clays in the sediment does not play significant factor in determining erosion rate. Recommendation given that highest priority for engineers and designers should be acquiring the proper soil for the job and not trying to plant dense amounts of vegetation in areas subject to destructive wave exposures. Final conclusion that coastal vegetation provides optimal function during long-term modifications and other gradual processes such as accreting and building elevation as response to sea level rise. The vegetation is in reality unable to handle “punctuated disturbances” or high-energy short-term events at seaward margin of salt marshes (notably including attenuating breaking waves). Therefore, the functional ability vegetation provides to erosion control are actually indirect results of long-term processes. The caveat is raised that every paper examined prior to this presented opposite conclusions on the ability of vegetation, namely the roots, to anchor and “shore-up” nearby sediment. Reexamining past papers, all conclusions arriving at the stabilizing ability seemed to assume the property without actually testing for it.

2. RESEARCH QUESTIONS

Two investigative question-hypothesis pairs were formulated to help structure the fieldwork providing in-situ data measurements as well as the complementary analysis that followed. Research questions (RQ) and hypotheses (H) were formed for a year-long hydrodynamic data time-series composed of more than 17,000 discrete, roughly 17-minute long bursts. For this proposal, a subset of 735 successive bursts containing 200 confirmed VGW events were used to determine preliminary answers to the RQ.

RQ1: *Are there any vessel related parameters (a1-a4) that can be shown to correlate with the wake characteristics (A1-A3) measured at the research site?*

Parameters to be investigated for such long-term correlations with VGW events include:

- a1) Vessel length and draft
- a2) Hull-geometry ratios (i.e., block coefficient)
- a3) Direction of vessel transit
- a4) Variants of the Froude number

While wake characteristics quantified through collected data include:

- A1) Measured wave height (historically the most prevalent indicator)
- A2) Change in water surface elevation during drawdown
- A3) Time duration separating the beginning of a drawdown and the wake arrival

H1: *No statistically significant correlation will arise between vessel specifications (a1-a4) and the observed VGW event measures (A1-A3) at the research site.*

Rejection of null hypothesis H1 signifies one or more of the examined vessel parameters a1-a4 has a statistically significant correlation with VGW observations described by A1-A3.

RQ2: *What are the relative contributions of each wave-generating condition (b1-b3) to the total wave energy levels at the study site?*

Conditions applicable to the field site are assigned to one of the following groups:

- b1) Calm, fetch-limited winds
- b2) Storm or frontal system winds
- b3) VGW events

H2: *Each of the three wave-generating conditions (b1-b3) will equally contribute to the total long-term energy flux measured at the site.*

Rejection of null hypothesis H2 indicates a particular wave-generating condition (b1-b3) forms a dominant role in the overall shoreward energy transmissions impacting the study site.

3. FIELD SITE

3.1. General Information

3.1.1. Geography

Data measurements originated from twin elevated platforms installed in Galveston Bay, Texas, (herein GB) known as “Simon” and “Garfunkel” (Figure 3.1). The platforms are roughly 2.5 m square, stand 400 m apart, and are both around 100 m away from the adjacent dredge island shoreline. Simon afforded the closest proximity to the HSC, located just under 1.2 km eastward. A team comprised of USACE and ERDC engineers led platform design and construction in late November of 2017. Initial timelines expected dike construction would soon follow, however the active 2017 hurricane season forced 6 months of delays as dredge assets were needed for high-priority maintenance. ERDC researchers lent additional field support with periodic, as-needed platform upgrades and maintenance during the data collection phase.

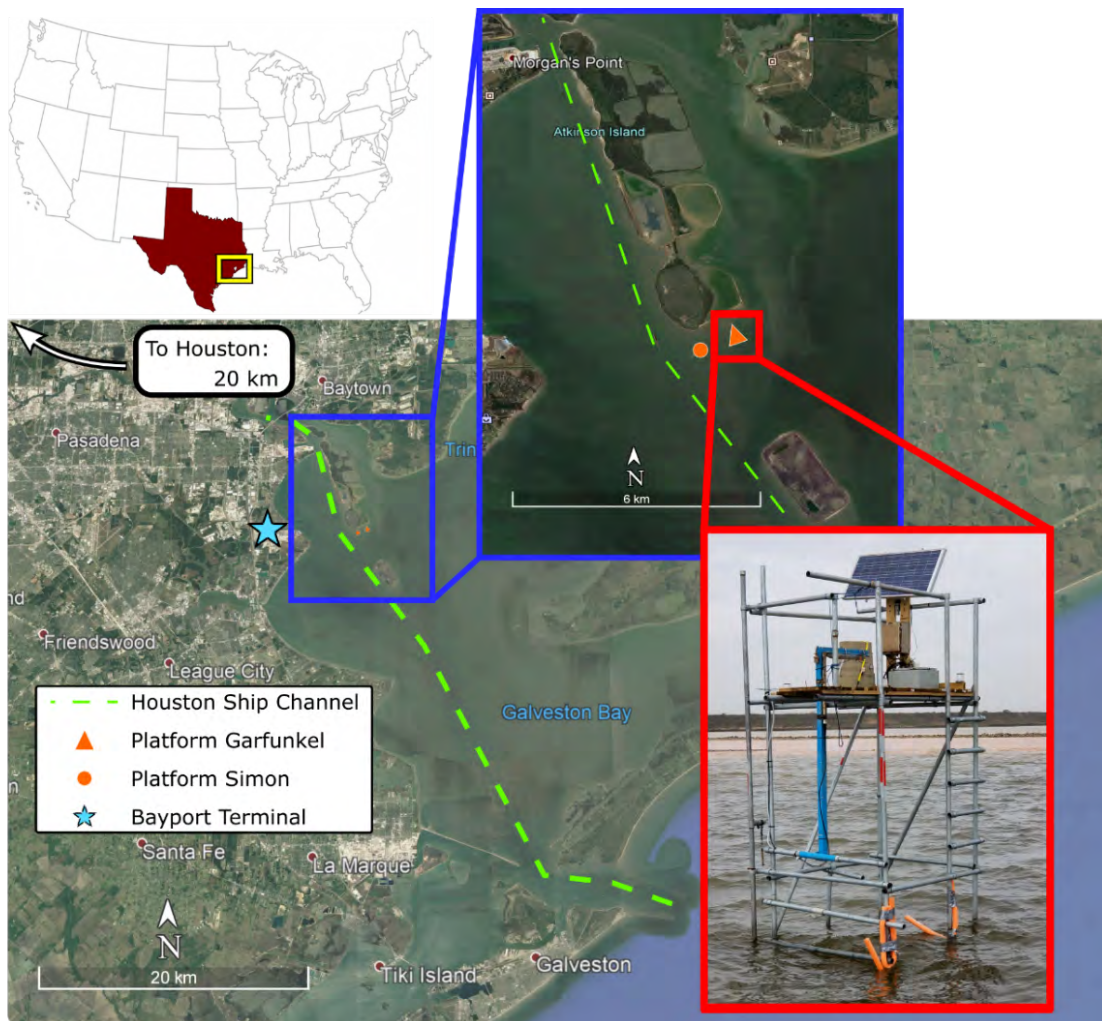


Figure 3.1: Field site location in Galveston Bay, Texas, and photo of “Garfunkel” platform.

The watershed that discharged a historic volume of freshwater outflow into GB after Hurricane Harvey flood events can be observed in Figure 3.2. The basin covers a fairly narrow swath of East Texas around 300 km wide and 600 km long, extending inland through the section of the Oklahoman border just north of the Dallas-Fort Worth area.

Although not overly impactful at this stage of the study, watershed processes will have a substantive influence on future sediment transport models. The area surrounding the site, and therefore the material dredged from HSC nearby, is predominately cohesive sediment as mentioned (i.e., roughly 40% clay, 40% silt, and 20% sand). Cohesive sediment behaviors affecting sediment transport rates such as flocculation, aggregation, and sedimentation are dependent on water chemistry parameters including pH and salinity [Hayter & Mehta, 1986; Winterwerp & van Kesteren, 2004]. The same water chemistry parameters are in-turn dependent on the freshwater/saltwater dynamic; the dynamic is determined through daily freshwater inflows and occasional flood events discharging into GB.

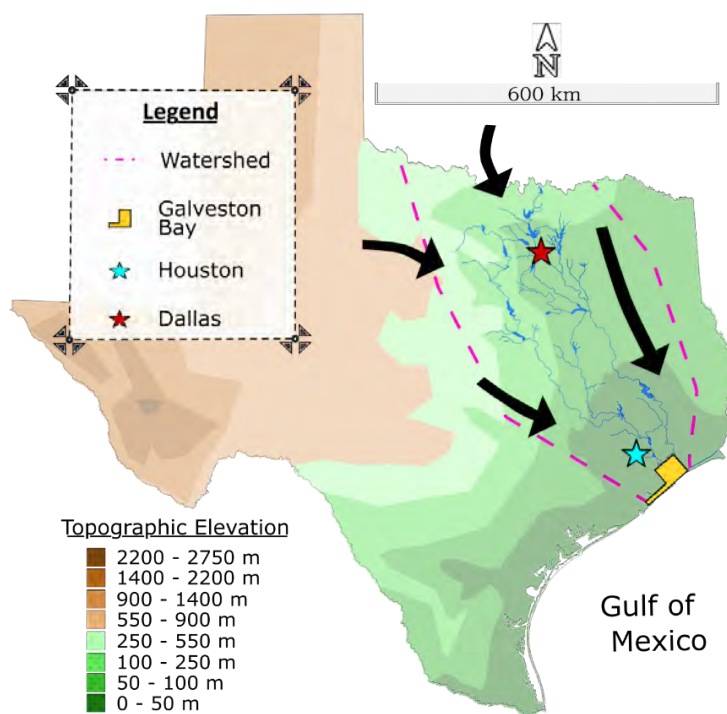


Figure 3.2: Topographic map of Texas overlaid with the delineated Galveston Bay watershed. Irrelevant waterways are neglected in this map.

GB is notoriously shallow with average and maximum undredged depths of approximately 2 m and 3 m, respectively. Such shallow depths are even more unexpected when kept in the context that GB forms the 7th largest estuarine system in the United States. Depths immediately around the project site tend to be even shallower, in part due to the raised seabed resulting from the initial dredging required to build the mixed sediment dike.

3.1.2. Vessel Traffic

The HSC remains one of the most heavily-trafficked ship lanes in America; the greater Houston port complex reported handling 260 million short tons of seaborne product in 2017, the most total tonnage of any port second only to the Port of South Louisiana [Port of Houston, 2018]. Port statistics show two liquid bulk carriers (herein tanker vessel) are expected to traverse HSC for every dry bulk carrier (herein cargo vessel). A preponderance of liquid carriers is reasonable due to nearly half the nation’s oil extraction job salaries are collected by Houston-based professionals [Gilmer, 2018].

3.1.3. Meteorological Setting

As the field site is located in the middle of a relatively large bay system (Figure 3.1), wind- and storm-driven events constitute a non-negligible influence on the local hydrodynamics. Frontal systems impinging the site are typically either maritime tropical (herein mT), maritime polar (herein mP), or continental polar (herein cP) [Henry, 1979; Schroeder & Buck, 1970]. A fourth frontal type known as continental arctic also are possible. These are, however, combined into the cP category for simplicity. Arctic fronts seldom penetrate as far south as GB, and when they do the effects are similar to the effects of the cP except with colder temperatures. Table 3-1: Details on frontal system types likely to impact the field site. briefly summarizes the relevant details from each frontal type. Abbreviations include maritime tropical (mT), maritime polar (mP), and continental polar (cP). Orientation describes the typical angle of the boundary line from due North measured clockwise (i.e., 0° is a vertical boundary running north-south). Note frontal event arrivals are not limited to the listed primary season.

Table 3-1: Details on frontal system types likely to impact the field site.

Front	Type	Boundary Orientation	Primary Season	Description	Miscellaneous Notes
mT	Warm	N/A	Summer	Warm, moist, unstable	Only front originating south of Galveston Bay
mP	Cold	40-50°	Spring	Cool, moist, unstable	Front most likely to reverse course and become warm front in winter
cP	Cold	90°	Summer	Cool, dry, stable	Front most likely to reverse course and become warm front in summer
cP	Cold	60-65°	Winter	Cold, dry, stable	N/A

Galveston Bay generally experiences the majority of fronts under winter conditions and the fewest during summer. The exact number and composition of frontal systems during any given year is a function of several climactic processes, most notably the modulation of the atmospheric

jet stream [Henry, 1979]. Another potentially significant process is the long-term pattern of the El Niño-Southern Oscillation (herein ENSO). During ENSO, phases of warming (i.e., El Niño) and cooling (i.e., La Niña) of the Pacific Ocean alter tropical air masses and, by extension, weather patterns around the world [NOAA, 2021a]. As a transition from weak La Niña to weak El Niño occurred during mid-2018 [NOAA, 2021b], impacts from ENSO on the site hydrodynamics were assumed negligible.

In addition to frontal systems, the other notable atmospheric contributors to the local weather patterns of the project site are known as the sea/bay breeze effects. Unlike the longer-term jet stream and ENSO patterns, sea/bay breeze effects are relatively short term as the timescale is linked to Earth's daily rotation. These coastal breezes are the result of stark temperature gradients forming along shorelines that then trigger a cycle of onshore-offshore airflow. This airflow is able to penetrate tens or even hundreds of kilometers inland along the Gulf Coast [Kocen, 2013]. The formation of temperature gradients stem from water having a specific heat roughly five times that of dry soil [Engineering Toolbox, 2003]. As the sun rises in the morning and begins heating the surface, the landward side of the coastline warms quicker than the seaward side, translating into the air column above the land heating faster than the air column above the water. Since air density is inversely proportional to the temperature, landward air rises at a rate exceeding that of the seaward air. The rising, less-dense landward air mass effectively creates a zone of lower pressure, prompting the denser seaward air mass to migrate inland in the form of a sea/bay breeze. At night the process will reverse into a land breeze, as now the land rapidly cools relative to the gradual heat loss of the water.

3.1.4. Tidal Hydrodynamics

GB is classified as having a diurnal tidal schedule due to its positioning along the Gulf of Mexico. The relatively confined Gulf effectively limits the tidal action to just a single daily cycle, translating to GB typically receiving only 1 high and low tide pairing each day. In actuality, there is an additional intermittent cycle of tidal constituent phase lag that operates on timescales lasting for weeks rather than a day [NOAA, 1989; Rayson et al., 2015]. The effect of this slightly longer-term process leads to only 2-3 weeks of any given month exhibiting the diurnal regime. The remaining 1-2 weeks are temporarily transformed into a mixed semidiurnal regime, often resulting in a reduced tidal range concurrent to the development of the second high and low tide pairing. Figure 3.3 provides an example of the two regimes alternating as the governing influence in GB over a 3-week period. The selected date range exhibits both of the potential tidal regime variations in Galveston Bay; a mixed semidiurnal tide is observed from March 16th – 21st while the more typical diurnal tide is present across the remaining days.

The timeseries begins as a standard diurnal tide that oscillates at a tidal range of 0.3 m for approximately a week. The single high tide peak begins the process of forming a secondary peak on March 16th, gradually culminating into the 2 distinct high tides of a mixed semi-diurnal regime 3 days later on March 19th. What was previously a 0.3 m tidal range is now observed as having lost over half of its initial magnitude, marking the start of the retransformation back into the diurnal regime. The mixed semidiurnal tide does not fully shed its second peak until March 22nd, a full 6 days after the secondary peak began showing. The diurnal tide is back to a 0.3 m tidal range within a couple of days, eventually reaching a maximum range of 0.4 m on March 25th.

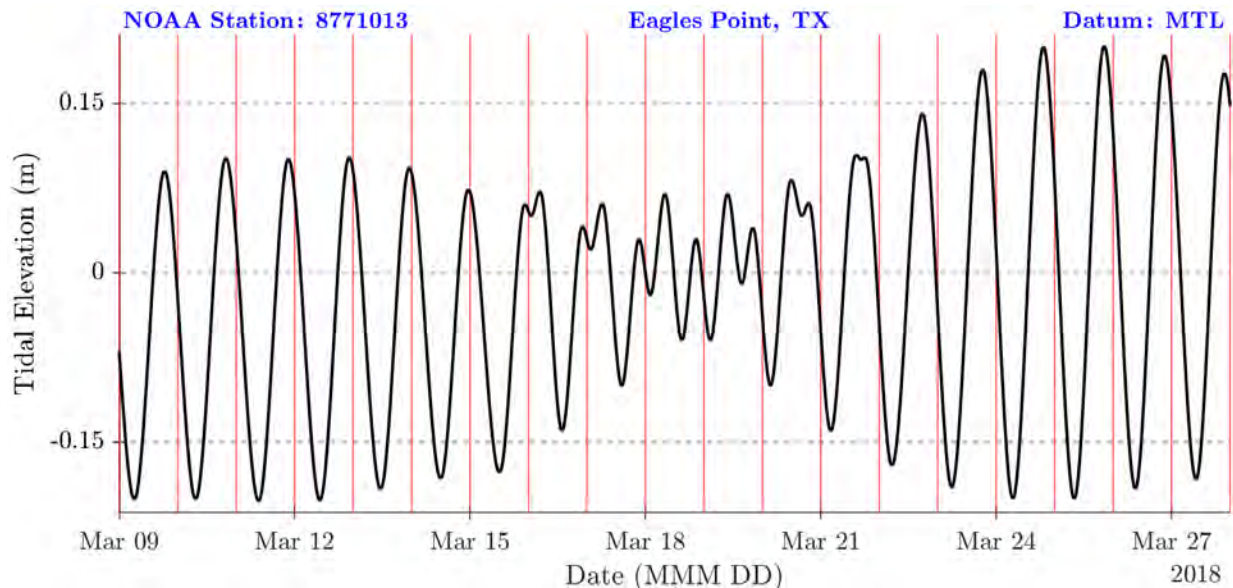


Figure 3.3: Tidal elevation time series from March 09th – 28th, 2018 as recorded by NOAA Station #8771013 located at Eagles Point, TX. The datum is set to mean tide level (i.e., the arithmetic mean of mean high water and mean low water). Vertical red lines indicate the start of a new day.

A key effect of the bay’s relatively large surface area is the variability in phase lag of the tidal constituents depending on what section of the bay is under consideration. Rayson et. al (2015) were able to estimate the tidal phase lag between the entrance channel and the northern sections near Trinity Bay/Morgan’s Point at around 5 or 6 hours. Their results further indicated the greatest phase lag shifts occur in the lower reaches of the bay, likely between the main inlet and Eagle Point, or just south of this project’s site platforms. A second notable discovery stemming from the harmonic analysis involved how the main semidiurnal tidal constituent (i.e., M_2) evolved while propagating into GB. The amplitude of the M_2 constituent was found to dampen by about 75% between the inlet entrance and Eagle Point, however it immediately rebounded - nearly doubling in amplitude as it traveled between Eagle Point and Morgan’s Point (i.e., while passing directly next to this project’s field site). As the M_2 constituent experienced amplification and phase lagging simultaneously, it was theorized that tidal reflections at the back of GB were in fact spawning standing waves along the nearby shorelines. Due to these standing waves existing relatively near the project site and the presence of the aforementioned phase lag throughout the bay, comparisons between tidal elevations and the long-term free surface elevation recorded at the platforms should keep these tidal phenomena under consideration.

3.2. Instrumentation

3.2.1. Platform Configuration

Figure 3.4 provides a labeled schematic of an installed platform that notes the location for each sensor or piece of equipment. Brief notes on the instruments such as brand, basic functionality, and measurement sampling regimes are given in Table 3-2.

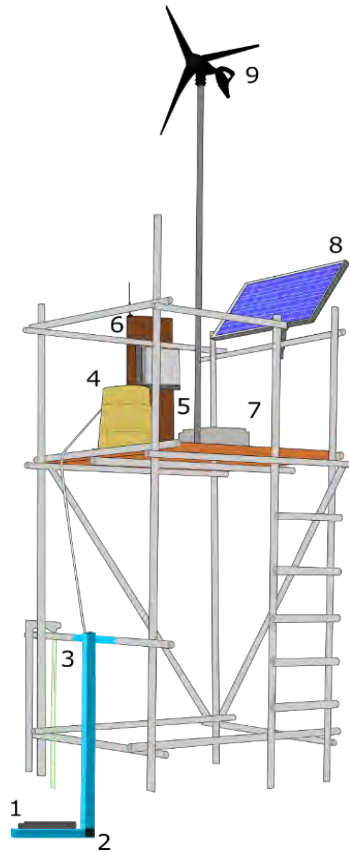


Table 3-2: Platform instrumentation.

#	Sensor	Brand	Function	Sample Rate
1	Acoustic Doppler Current Profiler	Nortek	Current velocity and pressure	17 min burst @ 2 Hz
2	Hydroacoustic Altimeter	EchoLogger	Depth to bed	Continuous @ 1 Hz
3	Wave Gage	Akamina	Water surface elevation	Continuous @ 8 Hz
4	Water Sampler	ISCO	Suspended sed. concentration	One sample per day
5	Computer Server	-	Upload data to web	-
6	Camera	MOBOTIX	Photograph vessel transits	One picture per 5 min
7	Battery Well	-	Power storage	-
8	Solar Panel	BP	Poly-crystalline	90 Watt
9	Wind Turbine	Nature Power	Blade diameter of 116.8 cm	400 Watt

Figure 3.4: Platform and instrument schematic

3.2.2. Acoustic Doppler Current Profiler Operation

Capable of recording both sea-surface elevation and current velocity timeseries, the primary instrument supporting hydrodynamic analysis was the Acoustic Doppler Current Profiler (herein ADCP) manufactured by Nortek. Sea-surface elevations and current velocities were measured via a pressure transducer housed in the sensor head (left panel of Figure 3.5) and via the 3 transducers on the sensor face (right panel of Figure 3.5), respectively.

The ADCP has two main modes of operation for current measurements, both of which are detailed in Table 4 [Nortek, 2008a; Nortek, 2008b]. Each operation mode transmits acoustic wave beams through the axial transducers and then monitors frequency changes in the acoustic waves reflected back. The reflections result from the acoustic waves rebounding off moving particles or bubbles entrained in the current. These frequency changes are known as the Doppler effect. By assuming the particles travel at the same speed and direction of the surrounding water, current velocity information is then indirectly calculated.

The sampling frequency of pressure measurements mirrors that of the active current measurement sampling regime (Table 3-3). This means that for each sampling cycle the current

profile mode will create a single pressure record, while the wave burst mode creates an entire pressure timeseries.



Figure 3.5: Photos of ADCP pressure transducer (black circle in left panel) and ADCP head with three velocity transducers (right panel).

Table 3-3: Description of ADCP operation modes.

Mode	Spatial Function	Doppler Method	Measurements per Cycle
Current Profile	Samples multiple vertically stacked cells; creates a water column “profile”	Monitor change in frequency of a single reflected acoustic pulse	A single magnitude and direction for all cells
Wave Burst	Samples a single cell; creates a high-resolution record for a point in the column	Monitor phase shift between successive acoustic pulse reflections	A timeseries of magnitudes and directions for the cell

Despite the additional spatial information provided by the vertical cell array of current profile mode, analysis only considers data from wave burst mode. Current profile mode allows a maximum sampling frequency of 1 Hz if wave burst mode is kept inactive, while wave burst mode can double this sample rate with a max frequency of 2 Hz. Each collection cycle of wave burst mode data (herein burst) lasted a maximum of 17 minutes at 2 Hz, resulting in a total burst length of 2048 datapoint. The ADCP can also only measure data in one mode at any given time, effectively extending the sampling frequency of current profile mode to one measurement per

20 minutes when using wave burst mode. As the high frequency component of VGW events typically contain waves with 1-second periods, the 2 Hz sampling frequency of wave burst mode constituted the minimum frequency necessary to resolve these short period waves. This minimum sampling frequency threshold is known as the Nyquist frequency (19):

$$f_{Nyq} = f_{max} * 2 \quad (19)$$

Wherein f_{Nyq} is the Nyquist frequency and f_{max} is the maximum resolvable wave frequency in the collected data.

Figure 3.6 illustrates the operation of an ADCP in wave burst mode above and below surface level; The left panel is an image of a deployed ADCP at platform Simon while the right panel is a schematic detailing the process of current sampling. The blue beam seen in the highlighted portion the left panel is the subaerial section of the blue “L” shaped beam anchoring the ADCP visualized in the right panel. The orange box in the right panel defines the cell volume where wave burst sampling occurs, roughly a 0.5 m wide cube centered about 1 m above the seafloor that starts 0.1 m away from the sensor (i.e., a 0.1 m blanking distance). The middle of the box was anywhere from 0.5 – 2.2 m below still water level, however given the relatively weak tides in GB, using the 10th and 90th percentile depths will shorten this range to between 0.7 – 1.9 m.

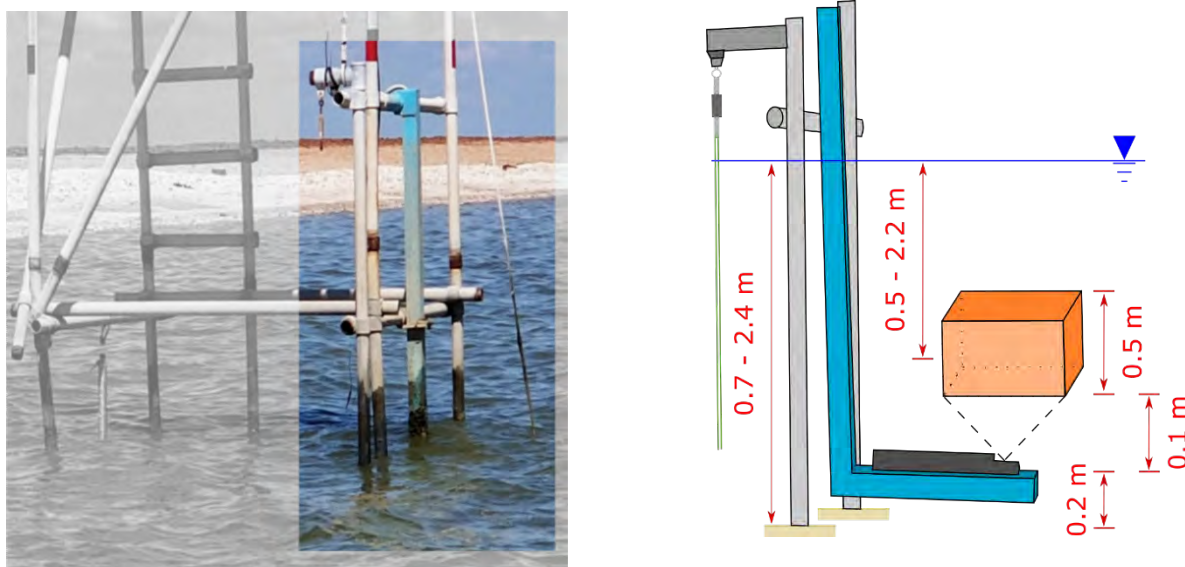


Figure 3.6: Photo (left panel) and schematic (right panel) of platform section with ADCP mounting arm. The approximate ADCP control volume for burst measurements is indicated by the orange box.

A typical ADCP deployment cycle began at the off-site lab by confirming all data from the instrument’s previous deployment was downloaded and cleared from the internal memory. Data transfers were accomplished via connecting the ADCP to a computer using a specialized cable and software provided by Nortek. Following the stored memory check, the deployment settings were then initialized in the software application using a saved setting regime that ensured deployment conditions were consistent throughout the project. Data collection was set to begin

around an hour after the instrument was expected to be deployed at the site; an ending time to stop data collection was unnecessary as the instrument could be switched off once retrieved and returned to the off-site lab. Biofouling prevention was then applied to ensure maximum fidelity of the collected data, a new internal battery was connected, and at this stage the ADCP was primed for field deployment.

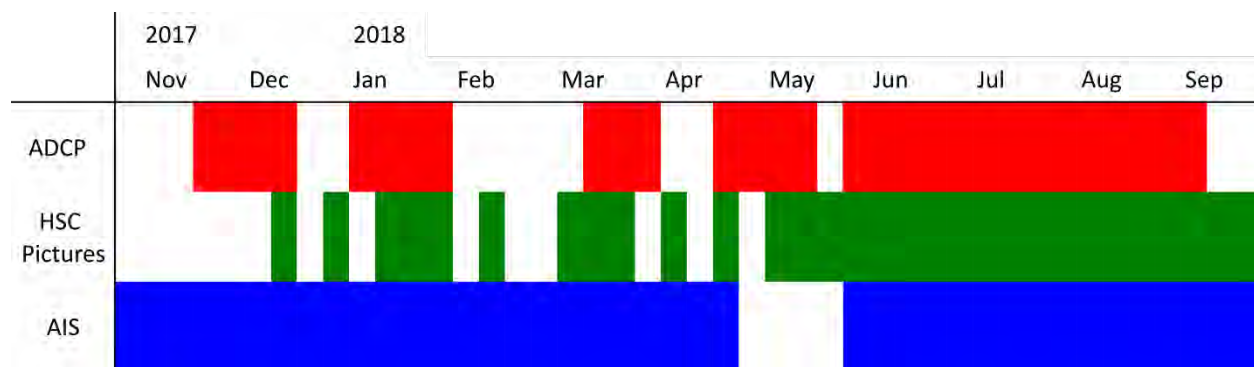
Deployments typically lasted for about a month as this stretch of time would not only drain most of the single-use internal battery, but also provide the maximum amount of time before the ADCP accumulated a problematic amount of biofouling in the warmer months. At the end of a deployment period, the ADCP would be raised from the water, swapped out for a fresh ADCP, brought back to the lab, have the data downloaded, and then undergo a full cleaning to remove any accumulated biofouling. Biofouling would typically accumulate on the 3 main acoustic transducers (right panel of Figure 3.5), inside the pressure transducer (left panel of Figure 3.5), and all along the body of the instrument. With the cleaning completed, the internal battery was at last removed, and the ADCP was stored until the next deployment.

3.2.3. Data Availability

For studies or projects that involve a fixed period of field research, the ideal outcome is naturally to have complete and uninterrupted data collection throughout the allotted time span. Reality often prevents such ideal coverages, however, as is seen in the data collection summary seen in Table 3-4. Reasons for periods of missing data include:

1. Periodic sensor maintenance (i.e., pulling ADCP from the site for battery exchanges, data downloads, memory wipes, and biofouling removal)
2. Sensor failure (i.e., wave gauge lines snapping and water sampler pump failure)
3. Corrupted measurements (i.e., the raised bed level post-dredging covering the altimeter, covering the water sampler tube intake end, and preventing the ADCP mount arm from fully extending)
4. Power loss (i.e., batteries powering the camera and server dying after overnight freezes and build-up of bird waste on solar panels preventing requisite battery charging)
5. Unavailable data (i.e., incomplete timeseries of USCG provided AIS data)

Table 3-4: Availability of quality-controlled data used in this report



3.3. Measured In-Situ Conditions

The following summaries of in-situ wind, hydrodynamic, and vessel traffic information each correspond to a subset of 735 successive data bursts taken from the roughly 17,000 bursts in total. All time stamps are noted as following UTC reference time unless otherwise stated. The first burst begins on March 13th, 2018 at 20:06:01, while the last burst ends on March 26th, 2018 at 14:13:04.

3.3.1. Wind

Wind-generated waves are the product of surface-level wind shears imparting energy into a body of water. The straight-line distance the wind travels along the water body's free surface, known as the fetch, is therefore a key determinant for how much energy transfer the shear force ultimately engenders. Fetch lengths for irregularly shaped shorelines can be calculated using the effective fetch method proposed by ERDC in the Shore Protection Manual [ERDC, 1977]. This method is performed via delineating 15 radials spaced 6° apart with the central radial matching the predetermined direction of wind propagation. As there are 7 radials to either side of the central radial, a 90° wide zone radiating from the site is created. It is assumed that any energy transmission by the wind will occur within this 90° zone (i.e., within 45° to either side of the primary propagation direction). Each radial is extended outward until the shoreline is reached, and after the radial distances are calculated they are then multiplied by the cosine of the corresponding angle made with the primary direction. The product of each radial length and angle cosine are then summed and divided by the sum of all the angle cosines, resulting in the effective fetch (20):

$$F_{eff} = \frac{\sum X_i \cos(\alpha_i)}{\sum \cos(\alpha_i)} \quad (20)$$

Wherein X_i is the distance from the site to the shoreline along radial i and α_i is the angle between the central radial and radial i . Figure 3.7 shows an example of radial delineations in GB for wind propagating in both north-northeasterly and west-southwesterly directions. These directions were chosen due to each providing the maximum effective fetch to either side of the bay; the site is notably located leeward of the dredge disposal island to the southeast.

Reported wind values are as measured by the National Oceanic and Atmospheric Administration (herein NOAA) station "MGPT2" located at Morgan's Point (Figure 3.1). The magnitude and direction of a sustained velocity value are the average over a 6-minute span, while the gust magnitude and direction record the single highest measurement during that same 6 minutes. The 6-minute timespans are centered around the reported timestamp. A timestamp of 12:00 thus represents measurements from 11:57 – 12:03.

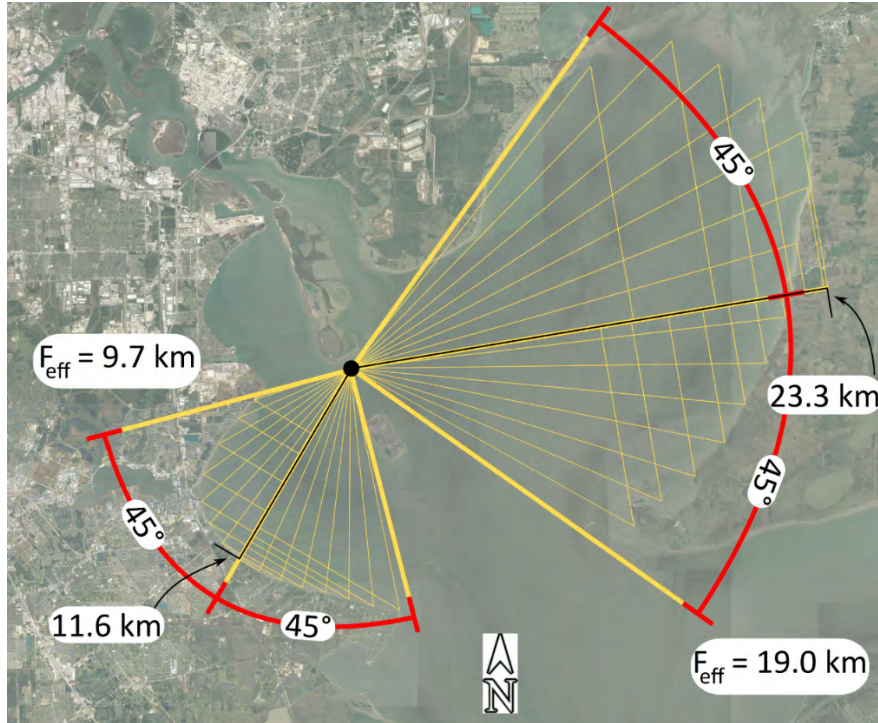


Figure 3.7: Illustration of how the maximum effective fetches were calculated for the irregular shoreline of Galveston Bay using the method recommended by ERDC (1977).

Wind directions are noted to have undergone two translations: first, a shift from the clockwise meteorological axis orientation (i.e., North at 0° and East at 90°) to a counterclockwise engineering orientation (i.e., East at 0° and North at 90°) followed by a second shift from directions defined by the heading of origin to directions defined by the heading of travel (i.e., a direction that was 270° is now 90°). These translations synchronize the wind direction axis with the axis orientation used during hydrodynamic analysis.

Figure 3.8 highlights the variability present throughout the year of data collection via partitioning the verified NOAA wind record by season. The subplots are organized into directional bins with widths of 22.5° and are centered around either a cardinal (i.e., north), intercardinal (i.e., northeast), or secondary intercardinal (i.e., east-northeast) direction. Two key data streams are overlaid: the bin measurement frequency (i.e., the left, black ordinate) and the corresponding average velocity of each bin (i.e., the right, red ordinate).

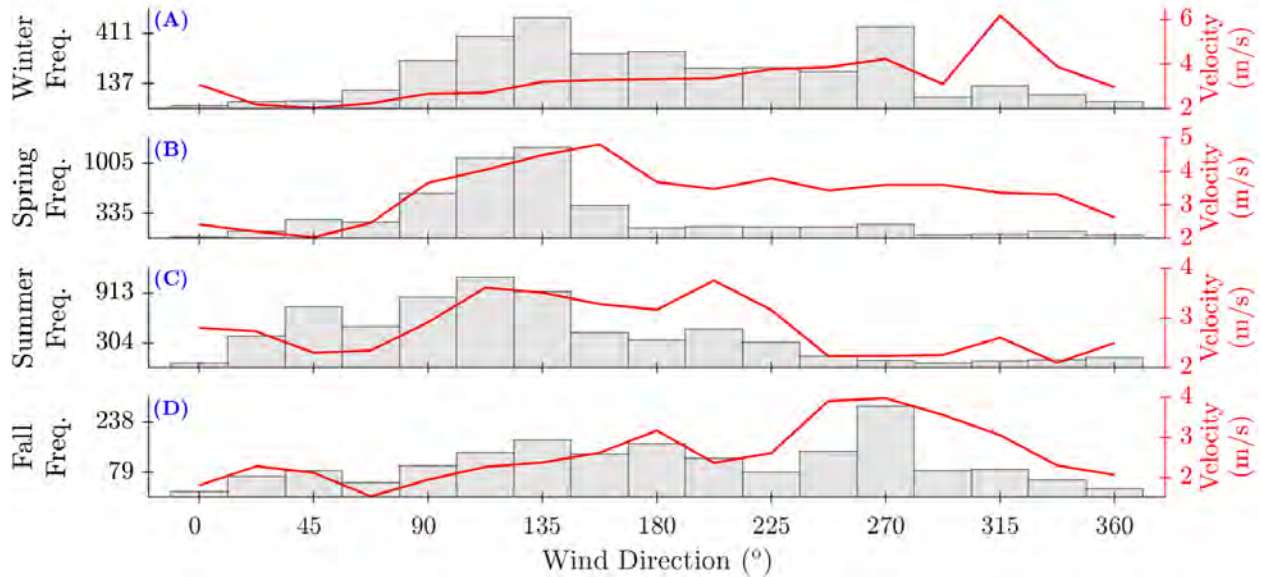


Figure 3.8: Seasonal histograms of the wind direction at the site overlaid by the corresponding mean wind velocity for each directional bin. Values recorded by NOAA meteorological station MGPT2, located near Morgan’s Point, Texas.

Table 3-5 delves deeper into the frequency distributions via aggregating the directional bins into 5 nonuniform groups based off the expected frontal and sea/bay breeze processes discussed in Section 3.1.3. Cell shades correspond to direction frequency with darker shades indicating greater frequency. Shade changes occur at 0.2, 0.4, and 0.6 frequency counts per degree. As an example, group 2 ranges from 78.8 – 168.8° and encompasses winds blowing anywhere between north and west-northwest, or roughly onshore at the site. Onshore-directed winds may be the product of sea/bay breezes, mT fronts moving inland from the Gulf of Mexico, or cP/mP fronts reversing direction northwards after penetrating into the Gulf.

Table 3-5: Distribution of binned seasonal wind directions normalized to frequency per bin degree.

Group #	Seasonal Frequency Distribution (Group Frequency / Deg.)				
	1	2	3	4	5
Group range (Group size)	0.0 – 78.8° (78.8°)	78.8 – 168.8° (90°)	168.8 – 236.6° (67.8°)	236.6 – 303.8° (67.2°)	303.8 – 360° (56.2°)
Winter	0.08	0.48	0.33	0.31	0.13
Spring	0.15	0.74	0.14	0.12	0.07
Summer	0.32	0.55	0.24	0.06	0.08
Fall	0.15	0.34	0.30	0.42	0.17

To arrive at a single seasonal value for each grouping, the individual measurements were first partitioned into sets bounded by the starting and ending timepoints of the ADCP bursts. A single averaged value was calculated for each burst and typically consisted of 2 or 3 values. A maximum of 3 values (i.e., 18 minutes of measurements) were potentially able to occur during a 17.5-minute ADCP burst due to the NOAA timestamps reporting the 6-minute collection period midpoint as previously discussed. With each burst now reporting a single average wind direction and velocity magnitude value, the middle time index of each burst was used to determine what season the burst belonged to. The seasonally categorized values then underwent one final sorting relative to the 5 directional bin groupings to give the tabulated results.

Directional observations from Figure 3.8 and Table 3-5 include:

1. The directional frequencies across the grouped bins show similar behavior during the fall/winter seasons and to a lesser extent during the spring/summer seasons.
2. Group 2, or the directions between the north bin minimum (i.e., 78.8°) and the west-northwest bin maximum (i.e., 168.8°), were the most consistent directional grouping throughout the year.
 - a. The largest grouping as it represents 25% of the total bin range
 - b. The dominate wind direction during the winter (43.2%), spring (66.6%), and summer (49.5%), also the second most dominate direction during the fall (30.6%).
 - c. There is a moderate overlap between group 2 directions and several of the radials drawn for the western reach's effective fetch in Figure 3.7 (i.e., just under half of the radials).
3. Group 3, or the directions between the west bin minimum (i.e., 168.8°) and the southwest bin maximum (i.e., 236.3°), were the second most consistent directional grouping during the year.
 - a. Group 3 wind directions have nearly complete overlap with the radials drawn for the eastern reach's effective fetch in Figure 3.7.

Wind velocity magnitudes are organized in Table 3-6 using the same approach of aggregating the directional bins into 5 groupings as was done for the directional frequencies in Table 3-5. Cell shades corresponds to velocity magnitude with darker shades indicating greater magnitude. Shade changes occur at 2.5, 3.5 and 4.5 m/s for the mean velocity magnitudes and at 7, 9, and 11 m/s for the maximum velocity magnitudes. The mean and maximum values reported in Table 3-6 correspond to the seasonally sorted mean and maximum magnitudes from each group of binned wind directions. As an example, the burst with the second highest maximum wind magnitude in the fall (i.e., 11.6 m/s) was found to propagate in a direction corresponding to group 3, yet the average value of all bursts associated with group 3 (i.e., 2.8 m/s) remains below the 50th percentile average velocity magnitude (i.e., 3.0 m/s).

Table 3-6: Seasonal velocities (mean and maxima) in each directional bin grouping.

Group #	Seasonal Velocities (m/s)				
	1	2	3	4	5
Group range (Group size)	0.0 – 78.8° (78.8°)	78.8 – 168.8° (90°)	168.8 – 236.6° (67.8°)	236.6 – 303.8° (67.2°)	303.8 – 360° (56.2°)
Winter Mean	2.3	3.0	3.5	4.0	4.9
Spring Mean	2.2	4.2	3.7	3.5	3.2
Summer Mean	2.4	3.4	3.4	2.2	2.4
Fall Mean	2.0	2.3	2.8	3.9	2.6
Winter Max	5.5	7.5	8.2	8.8	12.1
Spring Max	5.2	9.7	11.5	8.8	9.8
Summer Max	9.2	8.9	8.7	6.7	4.9
Fall Max	5.1	6.6	11.6	8.9	8.2

Velocity magnitude observations from Figure 3.8 and Table 3-6 include:

- Group 5, or the directions between the southeast bin minimum (i.e., 303.8°) and the east bin midpoint (i.e., 360°), recorded the largest average burst velocity (i.e., 4.9 m/s) and the burst with the largest maximum velocity (i.e., 12.1 m/s) during the winter season.
 - Frontal activity peaks in the winter months [Henry, 1979].
 - The front creating the 12.1 m/s maximum burst magnitude was likely of the mP variety.
 - mP fronts often constitute the majority of frontal systems in winter months
 - mP fronts usually enter the Gulf of Mexico west of Galveston while cP fronts enter from the east [Henry, 1979]. As group 5 propagates east-southeasterly, there is a strong indication the frontal system would perform arrive from the west.
 - Notably, group 5 was essentially the least frequent direction of wind propagation (Table 3-5). This implies there is a relatively considerable wind-wave energy divergence in this group of binned directions that is dependent on the presence of frontal activity.
- Not only were group 1 bins the second least frequent directions of propagation (Table 3-5), but these directions also consistently reported the weakest average velocity magnitudes (i.e., 2.2 m/s \pm roughly 0.2 m/s, Table 3-6).
 - Indicates frontal systems seldom propagated in a northeasterly direction.

- The maximum burst velocity magnitudes were extremely consistent throughout the year (i.e., 5.3 m/s \pm roughly 0.2 m/s) with the notable exception of Summer (i.e., 9.2 m/s), potentially indicating the presence of a strong mT system
 - mT fronts most commonly active during the summer [Schroeder & Buck, 1970].

Figure 3.9 organizes the measured wind data by timestamp, plotting the direction of the max sustained velocity (panel A), magnitude of the peak gust velocity (panel B), and magnitude of the max sustained velocity (panel C) from each burst. The directions and sustained velocities are the averaged values over the 6-minute period bounding each data point while the maximum gust is the peak velocity during the 6-minute period. The red highlighted period (morning of March 19th) provided the only period of storm conditions during the subset of bursts. As the data subset occurs in March, relatively one of the driest months of the year [rssWeather, 2013], just a single weak storm event was recorded during this period.

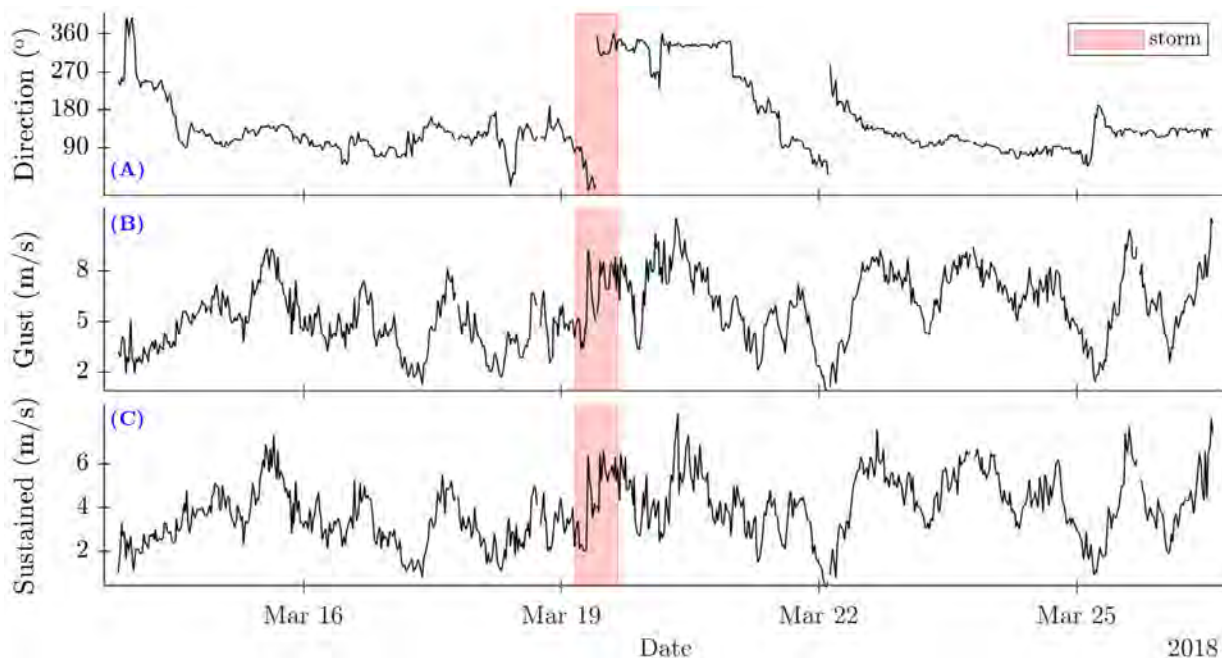


Figure 3.9: Average wind directions (panel A), maximum gust velocities (B), and mean sustained velocities (C) during the subset of bursts organized by measurement timestamp. Values recorded by NOAA meteorological station MGPT2, located near Morgan’s Point, Texas.

From the red region of Figure 3.9 it is observed that wind directions shift from blowing northerly to east-southeasterly (panel A) while also jumping 3 – 4 m/s in velocity (panels B – C). Considering the evidence of:

1. The onset of a roughly 3-day period exhibiting altered wind directions and velocity magnitudes coincides with the only precipitation of the month;
2. The wind direction shifts into an east-southeasterly direction;
3. The period occurs around the spring equinox.

It can be inferred that the event causing the disrupted weather pattern is a front arrival, specifically a front of the mP variety. It is possible to confirm this inference by using the NOAA National Forecast Chart for the morning of March 19th (Figure 3.10).

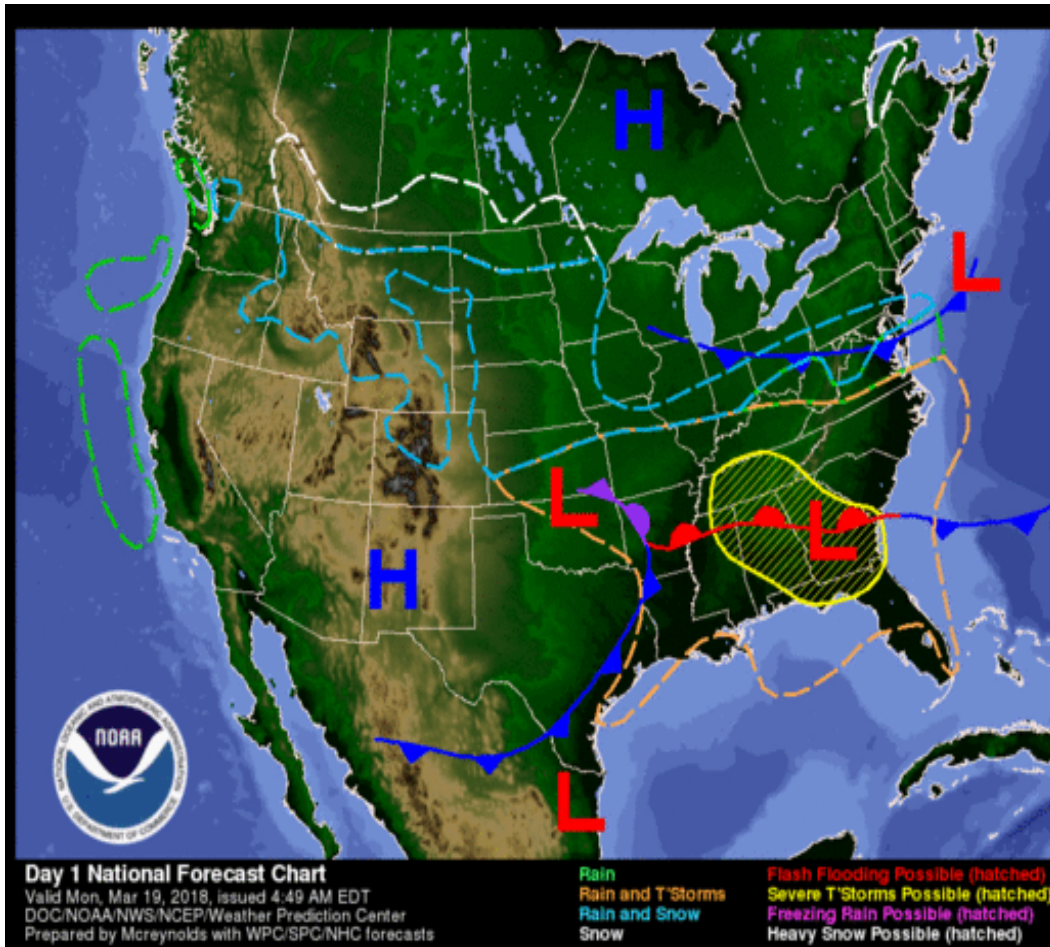


Figure 3.10: Archived forecast from the morning of March 19th showing the arrival of a marine polar frontal system at the project site.

Combining the forecast chart with the data in Figure 3.9, confirmation of the mP front includes that it:

- Is a cold front bringing precipitation;
- Arrives from the expected direction;
- Arrives at the start of the spring season;
- Presents a boundary line matching the expected 40-50° orientation (Table 3-1);
- Instigates a sudden change in wind direction into the expected east-southeasterly direction.
- Figure 3.11 plots the same NOAA data points except now organized by directional heading and also showing the average sustained velocity (panel C) in addition to the max sustained (panel B). The directions and sustained velocities are the averaged value over the 6-

minute period bounding each data point while the maximum gust is the peak velocity during the 6-minute period. During this nearly 12.75-day period, wind statistics include:

- The max sustained velocity was 8.3 m/s.
- The mean sustained velocity was 3.9 m/s with a standard deviation of 1.5 m/s.
- 65% of velocities were between 75° (north-northeast) and 165° (west-northwest).
 - These velocities are within 45° of the positive onshore (approximately 120°).
- 12% of velocities were between 300° (south-southeast) and 360° (east).
- 24% of magnitudes were at or above velocities of 5 m/s.
 - 71% of records above 5 m/s were between 60° and 150°.
 - 25% of records above 5 m/s were between 300° and 360°.

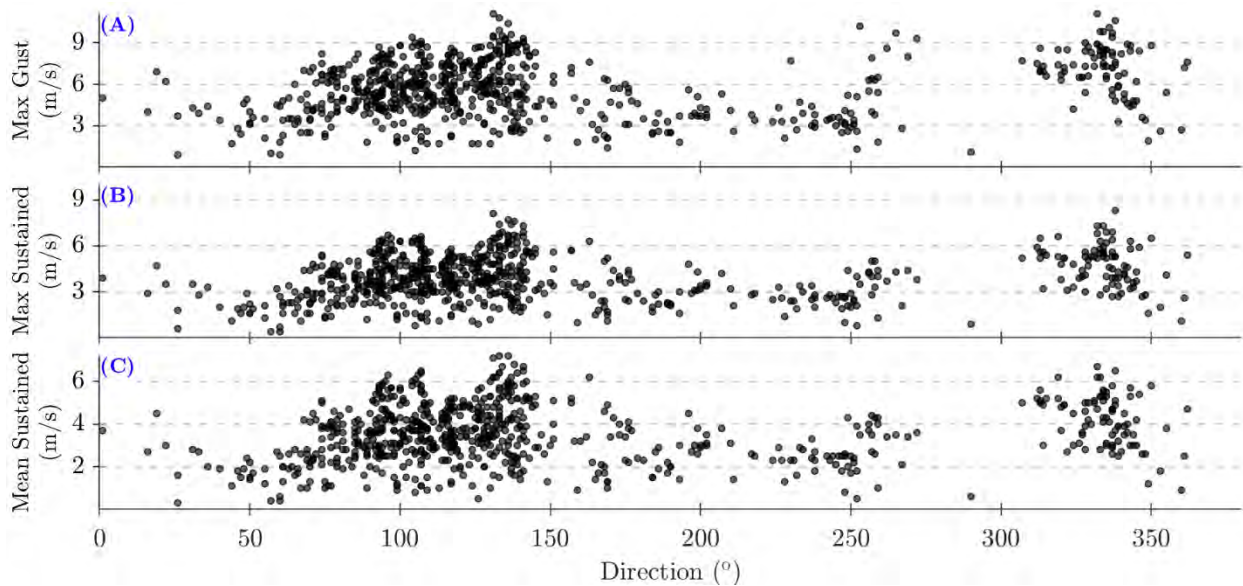


Figure 3.11: The maximum wind gust velocity (panel A), maximum sustained velocity (B), and mean sustained velocity (C) during each burst organized by wind direction. Values recorded by NOAA meteorological station MGPT2, located near Morgan’s Point, Texas.

3.3.2. Hydrodynamics

VGW event hydrodynamics are defined to include the free-surface elevations and magnitudes/directions of current velocity components observed during the wake events. A visual summary of the measured current velocity magnitudes and directions during the 735-burst subset is found in the right panel of Figure 3.12 with the corresponding wind record to the left. The approximate headings of the +u (i.e., perpendicular onshore) and +v (i.e., parallel alongshore towards the HSC) axes are also shown in red. The subset hydrodynamic record includes a total of 1,429,504 timepoints; each timepoint details the instantaneous water surface elevation, current velocity magnitude, and current velocity direction.

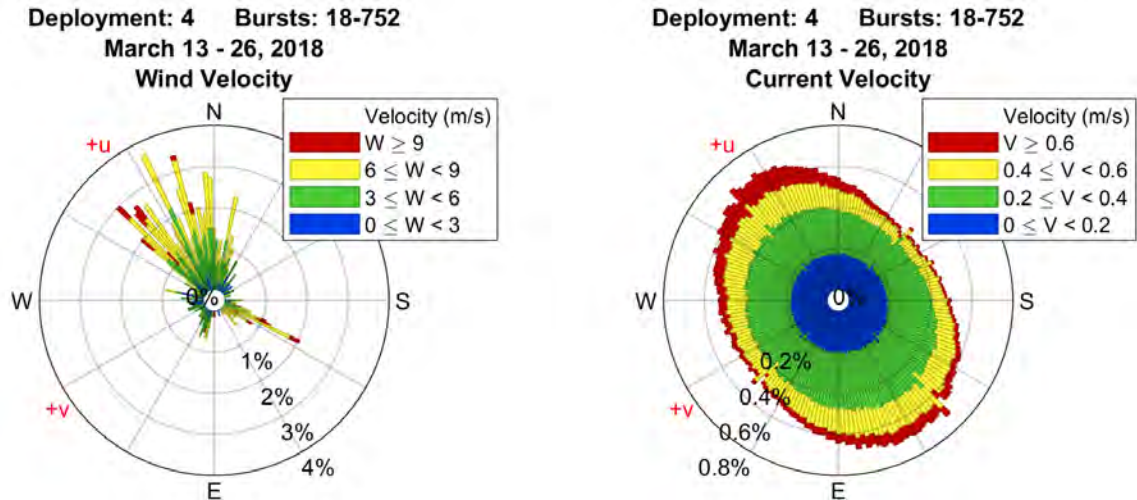


Figure 3.12: Wind rose styled plots of the wind (left) and current (right) measurements during the subset of bursts.

Due to the local March weather patterns, 65% of recorded wind directions were within 45° of +u, translating into 56% of all current directions oscillating within 45° of +u or -u. Further summaries for the current statistics include:

- 25% of magnitudes were at or above 0.4 m/s
 - 65% of magnitudes at or above 0.4 m/s were within 45° of +u or -u
- 0.6% of magnitudes were at or above 1 m/s
 - 83% of magnitudes at or above 1 m/s were within 45° of +u or -u

3.3.3. Vessel Traffic

Investigations into RQ1 (i.e., whether trends in VGW event hydrodynamics can be explained through correlations with vessel parameters) first necessitated linking individual wake events to the specific vessel responsible for generating the event. As the hydrodynamic data were time-localized, a similarly time-dependent history of vessel traffic could be used to establish such linkages. The vessel traffic information used in this project was recorded via the internationally recognized marine tracking system known as the automatic identification system (herein AIS, Figure 3.13). AIS functionality is summarized by the International Maritime Organization as needing to [IMO, 2019]:

- Provide information automatically to appropriately equipped shore stations, other ships, and aircraft;
- Information to be provided include vessel parameters such as: ship identity, type, size specifications, position, course, speed, and navigational status.
- Receive automatically such information from similarly fitted ships;
- Monitor and track ships;
- Exchange data with shore-based facilities.

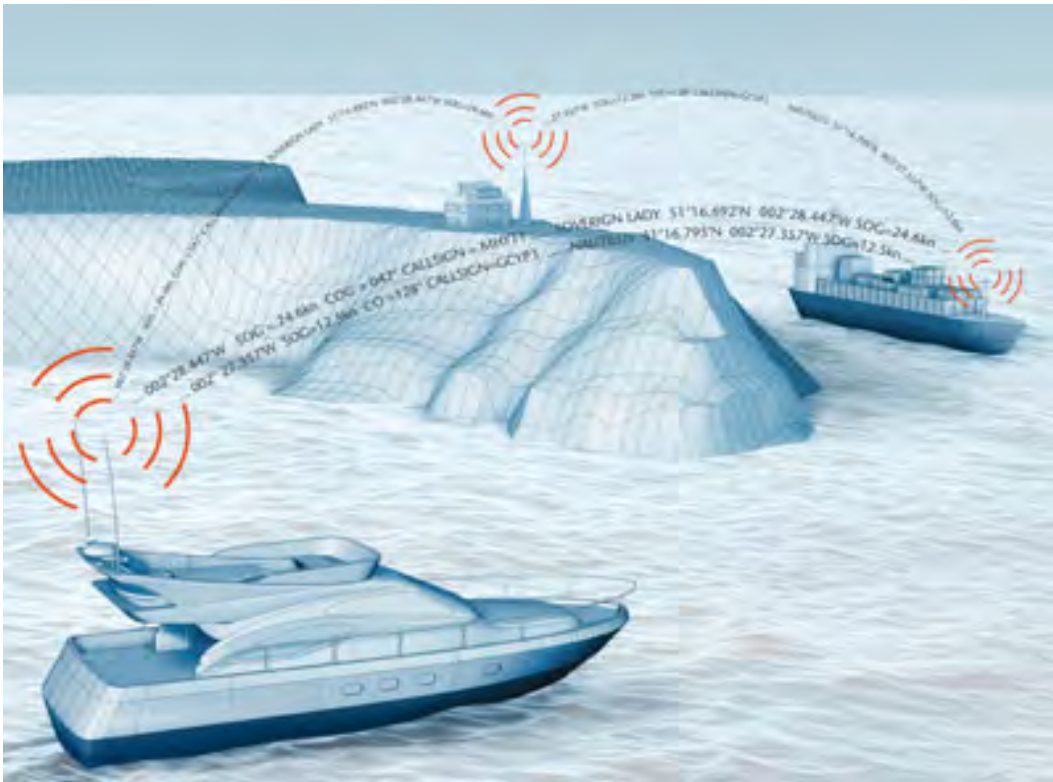


Figure 3.13: Schematic detailing the principles of AIS. Marine traffic control information can be observed passing between the vessels and shore-based station. Image adapted from IMO (2019).

AIS transponders are mandated for any passenger ship, any cargo ship 500+ gross tonnage not traveling internationally, and any ship 300+ gross tonnage traveling internationally. Vessels meeting any of these mandate guidelines are expected to maintain AIS operation at all times, with the exception of cases where the international agreements, rules, or standards allow for the protection of navigational information [IMO, 2019]. The commercial tanker and cargo vessels relevant to this project are noted as not qualifying for such protections and are thus expected to broadcast AIS information without exemption.

AIS databases are managed by both private interests and governmental entities; the database providing informational access to this project was sourced by ERDC from the United States Coast Guard (herein USCG). Contained in the USCG AIS database were 2 main data streams: the vessel traffic timeseries and a spreadsheet compiling all available parameters for each of the vessels found in the traffic timeseries. Examples of parameters from the spreadsheet data included vessel type, draft, length, and beam; examples of the information recorded in the traffic timeseries included the timestamp, position, heading, speed, and turn rate.

In order to limit the database to records potentially relevant to this project, ERDC reduced the records down to those containing spatial coordinates falling within the circumscribed box drawn in Figure 3.14. The box extents, 2.36 nautical miles vertical by 2.50 nautical miles horizontal, are set such that multiple AIS entries should be theoretically available for each transit within the project site, regardless of transit direction.

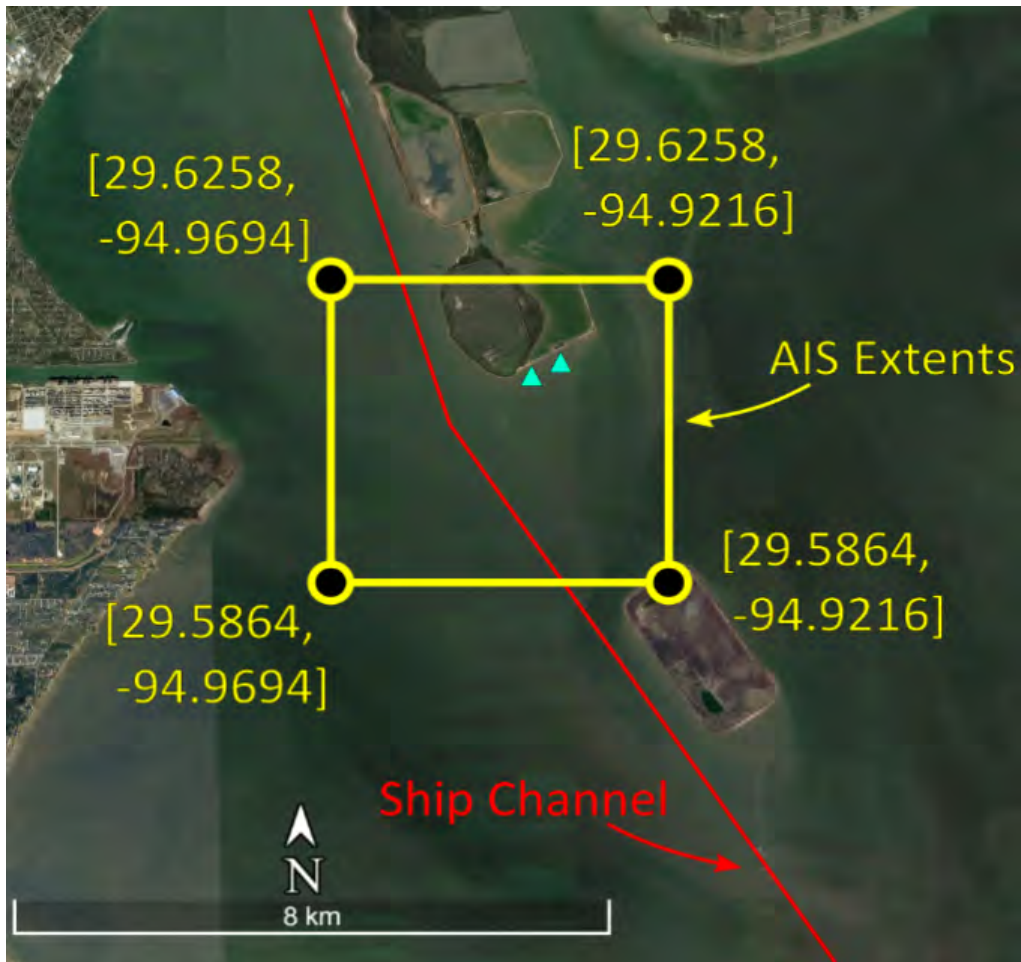


Figure 3.14: Extents of AIS data collection.

Multiple entries are expected given AIS broadcast rates are typically on the order of seconds, specifically every [MarineTraffic, 2021; USCG, 2020]:

- 180 seconds within 15 minutes prior to unmooring
- 10 seconds if sailing 0 – 14 knots;
- 6 seconds if sailing between 14-23 knots;
- 3.3 seconds if sailing 0 – 14 knots while changing course;
- 2 seconds if sailing between 14 – 23 knots while changing course.

The AIS data required minimal processing as the only adjustment was to convert the original timestamps from universal time (i.e., UTC) into local time (i.e., CST). This conversion synchronized the traffic timeseries to the time standard used in ADCP measurements, thus allowing for the desired time-dependent linkages between vessels and observed wake events to be made. The exact method for linking any given wake event to the correct generating vessel is discussed in the later methodology section (i.e., Section 4.2.8).

The size of the 735-burst period used to create the data subset was a function of how many bursts were required to find 200 VGW events. Many additional wake arrivals occurred during these 735 bursts, however scenarios preventing the inclusion of various VGW events include:

- Incomplete capture due to any portion of an event occurring outside ADCP collection periods
- Events from two ships transiting in opposite directions arriving close enough such that the wakes superimpose and cannot be individually isolated or are otherwise impacted by the interference
- Events unable to be captured during analysis due to weak hydrodynamic wake effects (i.e., transits by smaller or unloaded vessels during windy conditions and/or high tides)
- Wakes successfully captured unable to be identified due to missing AIS records (i.e., roughly 10-20% of inbound vessels seem to have had inactive AIS transponders)

Other than operator error, an explanation for inactive AIS transponders may be the vessel outfitted with outdated AIS technology. The USCG notes an additional satellite was added to the GPS constellation in February of 2008; AIS transponder models predating 2008 may be unable to recognize the newest satellite and fail to calculate positionings as a result [USCG, 2020].

Summaries of key parameters from vessels positively identified during the data subset are provided in Table 3-7 and Figure 3.15. Figure 3.16 and Figure 3.17 show example images of a tanker and cargo vessel transiting the HSC as taken by the camera mounted to platform Simon along with a higher resolution image of each ship.

Table 3-7: Statistics of selected cargo and tanker vessel parameters

Type	Count	Length (m)	Draft (m)	Block Coeff. C_{B-SDWT}	Length Froude # Fr_l
		Min/Avg/Max/SD	Min/Avg/Max/SD	Min/Avg/Max/SD	Min/Avg/Max/SD
Cargo	56	100/199/294/48.5	4.1/9.1/12.5/2.3	0.29/0.60/1.23/0.19	0.09/0.13/0.27/0.03
Tanker	144	112/186/274/35.3	5.4/9.4/14/1.9	0.42/0.73/1.19/0.16	0.08/0.12/0.21/0.02

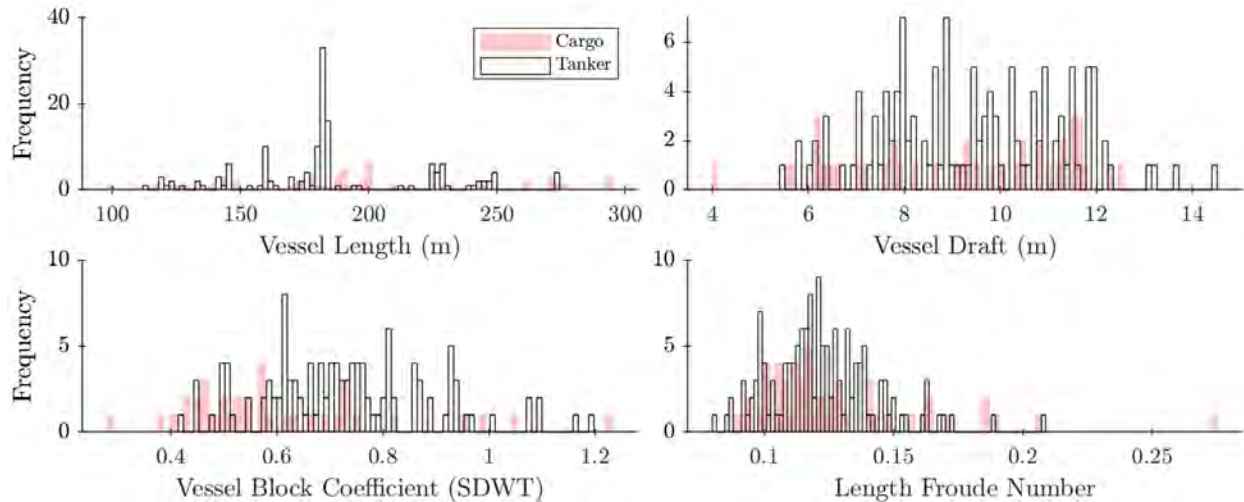


Figure 3.15: Distribution of selected cargo and tanker vessel parameters.

Although beyond the scope of this proposal's analysis, a few examples of longer-term HSC vessel traffic statistics from Nov. 1st, 2017-Oct. 31st, 2018 (keeping in mind May 2018 lacked all AIS records) include:

- 2,453 different tanker and cargo vessels made at least 14,058 total transits by the site;
 - 1,031 cargo vessels (i.e., 42% of vessels) made 4,258 of the transits (i.e., 30% of transits)
 - 1,422 tankers (i.e., 58% of vessels) made 9,800 of the transits (i.e., 70% of transits)
- On average 1,277.5 transits occurred per month
 - Monthly minimum of 1,106 transits in February and maximum of 1,504 in March
- On average 42.0 transits per day
 - Daily minimum of 37.3 transits per day in October and maximum of 49.7 transits per day in March



Figure 3.16: Inbound transit photo of cargo vessel MSC Heidi taken by the camera mounted to platform Simon on July 28th, 2018 at 15:05 (top) and high-resolution image of the same vessel for reference (bottom).



Figure 3.17: Outbound transit photo of tanker vessel Zaliv Baikal taken by the camera mounted to platform Simon on July 28th, 2018 at 14:55 (top) and high-resolution image of the same vessel for reference (bottom). The surface wake component of the event can be seen rounding the embankment as a white-capped broken wave.

4. METHODOLOGY

4.1. Data Quality Assurance and Control

4.1.1. General

Processing raw hydrodynamic data using quality assurance and quality control techniques (herein QA/QC) is imperative for confirming collected data as accurate and substantive. Numerous avenues exist whereby measurements can experience fidelity reduction or outright corruption, ranging from user errors to environmental conditions. lists several such sources of erroneous data that are particularly relevant to ADCP sensors, along with a few suggested methods for addressing each source. Note that some of the sources listed are as noted in Elgar et al. (2005) and Elgar et al. (2008).

4.1.2. Velocity Data Processing

Post-deployment QA/QC of the recorded velocity data took the form of the following steps:

1) Set the signal-to-noise ratio threshold for the specific deployment

Signal-to-noise ratio (herein SNR) is the acoustic signal strength relative to the background noise level. The background noise level is not explicitly given by the Nortek ADCP, however the strength of measurement amplitudes while the ADCP is out of water can provide a sufficient proxy [Nortek, 2019]. Each of the project deployments experienced background noise (i.e., subaerial measurements) at either the beginning or end of the collection period. Subaerial measurements occurred at the beginning of deployments if the instrument was not installed before the predetermined start time of data collection, and occurred at all deployment endings due to measurements not ceasing until after the instrument was transported from the field site to the lab for post-deployment processing. Background noise amplitudes are noted as stationary between the start and end of the deployment. The Nortek manual only notes "...data will be questionable when [amplitude] signal levels are down around the [background] noise level" [Nortek, 2008a], however a comprehensive threshold was found to be (21):

$$SNR\ Threshold = 3 * Noise\ Floor \quad (21)$$

Empirically adjusted SNR thresholds for acoustic Doppler instruments across various manufacturers have been found up to 8 times the noise floor [Elgar et. al, 2005]. With the amplitude strengths recorded as integer values known as counts, the noise floor was calculated using the mode value of the amplitude strengths below 50 counts. The 50-count value was chosen to split the background noises (i.e., typically 20-25 counts for the 2 Mhz ADCP) from the measured data (i.e., typically starting at around 60 counts). Figure 4.1 plots histograms of the amplitude strengths across the 3 ADCP axis beams (right panel of Figure 3.5) during the first deployment. The background noise level is observed via the large concentration of values at the 22- and 23-count bins while the potentially valid data are the values spread between 60 and 160 counts.

Table 4-1: Potential sources of faulty ADCP velocity data measurements and respective solutions.

Source	Effect	Solution
Rapidly moving particles within the sampling volume	Phantom or successive returns corrupting data measurements	QA/QC post-processing of the data stream
Excessive acoustic scatterers in the water column	Injects noise into the data signal	QA/QC post-processing of the data stream
Weak scatters unable to provide sufficiently strong returns	Low confidence in reported measurements	QA/QC post-processing of the data stream
Biofouling blocking acoustic beams (or clogging pressure transducers)	Degrades the accuracy and precision of measurements	Biofouling prevention steps pre-deployment; deep cleaning post-deployment; reduced deployment duration periods
Surfzone phenomena such as accreting beds, excess bubble entrainment, or subaerial exposures	Partial or total failure of the acoustic beams or pressure transducer	Cognizance of the local surfzone behavior across all conditions; appropriate deployment regimes; frequent instrument checks
Insufficient battery power supply	Nonstationarity in the collection process; outright sensor failure	Confirm battery status pre-deployments; appropriately planned deployment durations; awareness of collection settings relative to power usage
Instrument uses improperly programmed collection settings	Suboptimal data collection; data does not represent the intended collection parameters	Carefully review settings pre-deployment; fully understand how each setting option alters performance; ensure settings are optimized for the collection goals given the expected site conditions

2) Set the maximum feasible velocity threshold

As a check for unreasonably high velocity magnitudes that would otherwise pass QA/QC using the amplitude value, velocity component thresholds were set at 1.5 m/s for the northing and easting beams (i.e., the *u* and *v* components after conversion from *ENU* coordinates into *uv* coordinates) and 1 m/s for the upwards beam.

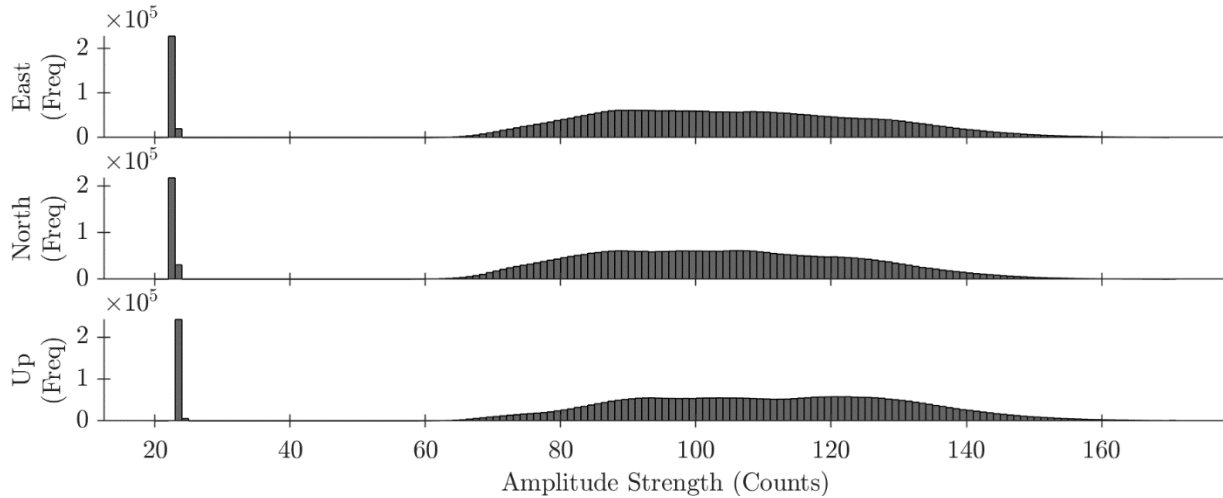


Figure 4.1: Histograms of the Easting, Northing, and Upward directed beam amplitude strengths of the ADCP during the first deployment (i.e., between November and December of 2017).

3) Determine how many measurements failed SNR or maximum velocity thresholds in each burst

To pass the velocity QA/QC, each 17-minute burst of 2048 datapoints was required to have less than 50 datapoints (i.e., 2.4% of the burst) failing either the SNR or feasible velocity magnitude thresholds across any of the 3 beams. The 50-datapoint allowance was determined using (22) [Elgar et. al, 2005]:

$$n_i = 25 * f_s \quad (22)$$

Wherein n_i is the number of allowable erroneous datapoints in the burst along beam i and f_s is the sampling frequency of the instrument.

4) Address erroneous measurements if necessary

Bursts with 1 or more beams containing between 1 and 49 instances exceeding SNR or velocity magnitude thresholds were corrected by replacing erroneous datapoints with values predicted by cubic spline interpolation. Bursts with 1 or more beams containing 50 or more erroneous points were tossed altogether as the overall burst was then considered corrupted.

5) Convert velocity component coordinates from ENU to uv

The translation of velocity components from an *ENU* coordinate system over to *uv* was accomplished using (23):

$$uv = \frac{ENU}{\cos(\alpha)} \quad (23)$$

Wherein *uv* is the cross-shore perpendicular (i.e., *u*) or alongshore parallel (i.e., *v*) component value, *ENU* is the easting (i.e., roughly alongshore) or northing (i.e., roughly cross-shore) component value, and α is the angle between the *ENU* and *uv* axes. For this site, α was 31°

(Figure 4.2). As the positive v component points alongshore parallel towards the HSC, the easting component is also noted as needing to be “flipped” via multiplying the value by negative 1.



Figure 4.2: Illustration of ENU (i.e., white arrows) and uv (i.e., red arrows) axes orientations at the site. Each set of arrows originate at one of site platforms.

4.1.3. Pressure Data Processing

The QA/QC process for the pressure data was notably different than that for the velocity data. This discrepancy was due to the velocity measurements having the ability to gauge fidelity using acoustic return amplitudes, in contrast to the pressure measurements which had no such supporting indicators. The post-deployment QA/QC of the recorded pressure data took the form of the following steps:

- Identify peaks and troughs in the pressure data for each burst
Without referencing the pressure-velocity relationship defined by LWT, invalid pressure measurements were distinguished via identifying outliers in the recorded timeseries. As single-point outliers take the form of large deviations from the surrounding values, it was assumed corrupted measurements would exist as a peak or trough in the signal. The pressure-velocity relationship derived in LWT was not utilized due to 2 main reasons: the inability of the relationship to determine whether the pressure measurement, velocity measurement, or a combination of both constituted the incorrect value(s), and the additional error introduced by the inclusion of interpolated velocity values.

- Differentiate each burst of pressure data into first and second order differentials
Single-point outliers in the pressure signal naturally present unusually strong jumps or spikes between successive points. Taking both the first differential (i.e., the rate of sea-surface elevation change) and second differential (i.e., the acceleration in the rate of sea-surface elevation change) of the pressure signal thus elucidates the corrupted pressure measurements by identifying potential instances of infeasible or unnatural first and second order rates of change.
- Determine the location of outliers in both differentials for each burst
The potential occurrences of infeasible rates of sea-surface elevation changes are confirmed via searching for outliers. The median absolute deviation (i.e., MAD) method was used for determining outliers (24):

$$MAD = \frac{-1}{\sqrt{2} * \operatorname{erfcinv}\left(\frac{3}{2}\right)} * \operatorname{median}(|A_i - \operatorname{median}(A)|) \quad (24)$$

Wherein $\operatorname{erfcinv}$ is the inverse complementary error function, A_i is the i^{th} value in the vector A , and a MAD of 3 or greater indicates A_i as an outlier.

- Correlate peak/trough locations with identified rate of change outliers
A pressure measurement must exist as a peak or trough in the recorded signal and constitute an outlier in both orders of signal differentials to be classified as invalid.
- Address erroneous measurements if necessary
Pressure transducer data is less susceptible to multi-measurement periods of unfavorable collection conditions as compared to acoustic Doppler velocity data (i.e., the majority of error sources listed in Table 4-1 are only applicable to acoustic Doppler sensors). With invalid pressure measurements therefore assumed as single-point occurrences, a limit to how many invalid measurements could be allowed per burst was rendered unnecessary; all pressure measurements classified as invalid were corrected by simply averaging the surrounding values. The per-burst limit on invalid velocity measurements is noted to serve as a proxy for identifying bursts impacted by extended periods of unfavorable collection conditions (i.e., on the timescale of tens of seconds), thus without a similar susceptibility to these periods, the pressure signal has no need to be limited using this proxy.

4.2. Wake Identification

4.2.1. Decision Algorithm Overview

The process of identifying a VGW from in-situ measurements took the form of a multifaceted algorithm that coalesced multiple data streams into a final decision on whether an event arrival was occurring at any given moment. In all, a total of 5 different analysis techniques were

eventually integrated into the algorithm, each attempting to provide an additional layer of confidence for the final outcome.

The need for numerous considerations was magnified due to a surprisingly large fraction of ships missing their travel records (i.e., approximately 10 – 20%), especially those in the inbound direction. This not only prevented the algorithm from relying on vessel transit logs, but also meant identification must occur completely independent of the AIS data, since logs were then essentially reduced to providing confirmation only.

4.2.2. Multiresolution Analysis

The initial step in the decision chain was to deconstruct the pressure into discrete frequency bins with a Multiresolution Analysis. In this technique, orthonormal bases are derived for orthogonal projections onto orthogonal complements of closed subspaces known as Hilbert spaces (14). With the orthogonal basis defined, a timeseries is able to be mathematically partitioned into scaled components that still maintain time localization. This translates in practice to a water surface elevation profile decomposing into frequency bins scaled into octaves, that, once superimposed back over one another, recreate a surface profile identical to what was initially started with. The ability to maintain time localization is especially noteworthy considering Fourier Transforms, a mainstay in signal processing and coastal engineering, are unable to preserve time dependent signal events, such as VGW.

An example of a full multiresolution decomposition is shown in Figure 4.3, where the original detrended water surface elevation profile of a complete ADCP data burst is shown in the topmost panel (panel A). The following panels then each contain the proportional amount of signal variance at any given time that originates from the corresponding range of time periods; adding the values of each scaled panel at time period $t = x$ will result in the exact same $t = x$ value found in the original signal. With each drop in bin level comes a drop in period octave, continuing until the highest frequency panel is bounded by the sampling frequency of the data series. For the second panel down, panel B, this would equate to wave energies found between the 128 to 256 second range, while the bottommost panel, panel I, designates energies between 1 and 2 seconds, the shortest periods considered during this analysis.

A unique benefit to multiresolution decomposition for VGW events in particular is the isolation of the Bernoulli and Havelock wake components. A Bernoulli pressure wave creating the large drawdown and subsequent surge is readily seen in Figure 4.3 arriving around the 02:37 timestamp in panels B-C, while the high frequency Havelock surface waves arrive soon thereafter in panels G – I.

The deconstructed water surface elevation timeseries provided in Figure 4.3 is the starting point for several of the analysis methods, including the first direct addition to the decision chain – a statistical summary of the burst. By taking the 8 individual bins and aggregating them into 3 (i.e., hi/mid/low frequencies), an indication of whether a wake is contained in the burst may be readily observed (Figure 4.4).

This indication is a result of the extreme deviation from stationarity experienced by each deconstructed frequency bin upon arrival of a VGW; notably observed just after the 02:36 timestamp when the Havelock waves reach the sensor in Figure 4.3 and Figure 4.4. The abrupt arrival of the VGW wave packet radically alters the statistical summaries of the combined high and mid frequency bins (Figure 4.4, panels D and C), especially when contrasted against equivalent bins from bursts without any VGW events.

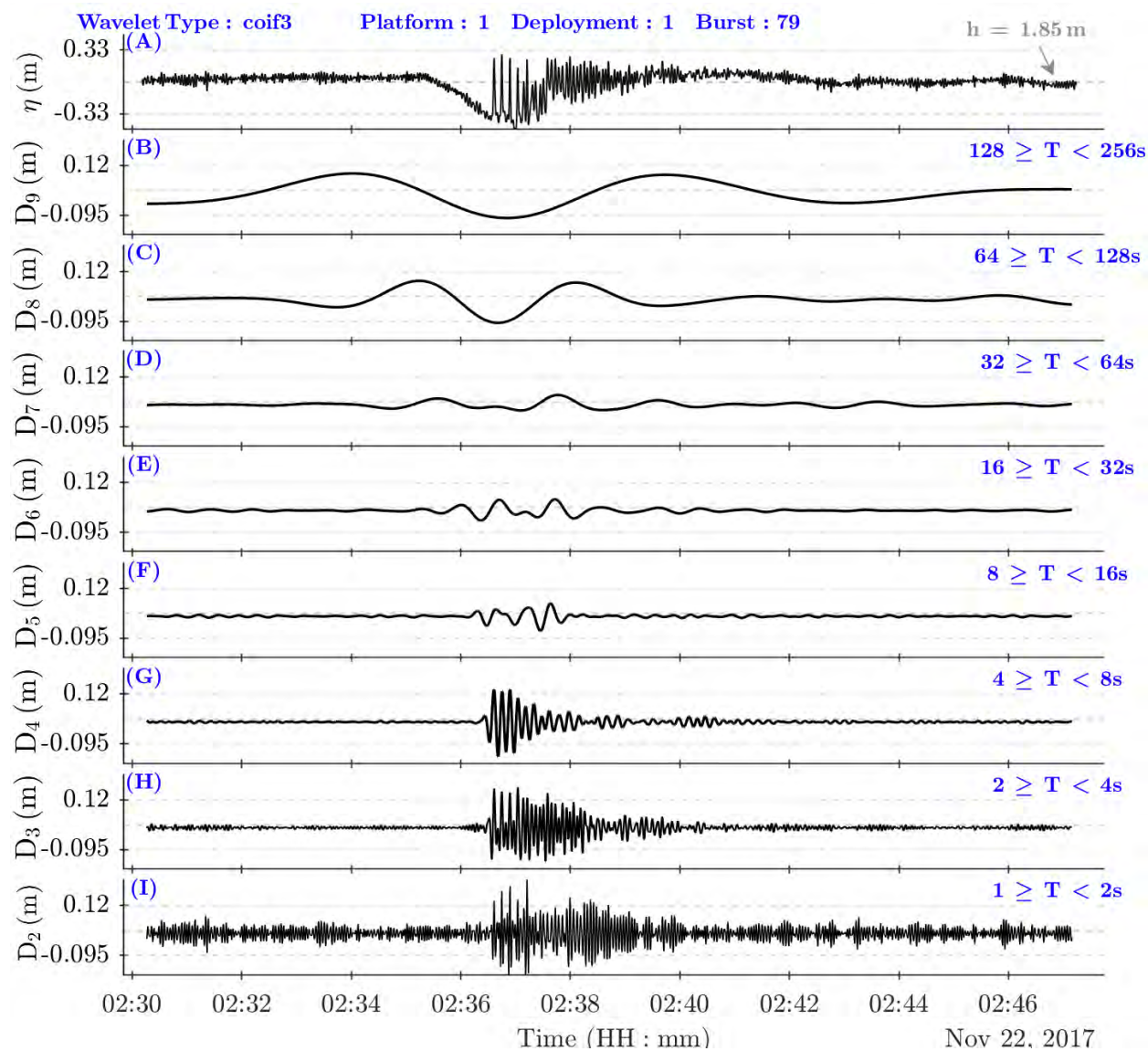


Figure 4.3: Multiresolution analysis of a water surface elevation time series containing a vessel-generated wake event arriving just after 02:36.

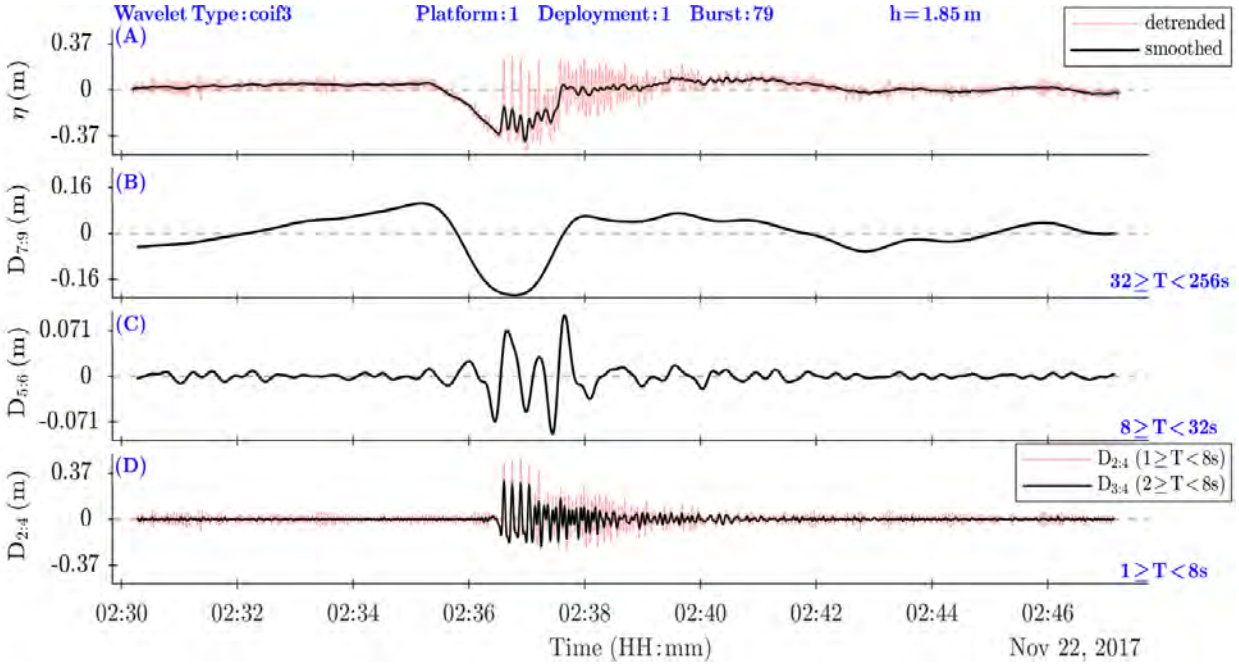


Figure 4.4: The decomposed signal regroupped into 3 main frequency bins. High frequency (panel D) now contains 1-8 second periods, mid frequency (C) contains 8-32 second periods, while the low (B) contains the remaining 32-256 second periods. Original detrended water surface elevation show on top (A).

This indication is a result of the extreme deviation from stationarity experienced by each deconstructed frequency bin upon arrival of a VGW; notably observed just after the 02:36 timestamp when the Havelock waves reach the sensor in Figure 4.3 and Figure 4.4. The abrupt arrival of the VGW wave packet radically alters the statistical summaries of the combined high and mid frequency bins (Figure 4.4, panels D and C), especially when contrasted against equivalent bins from bursts without any VGW events.

4.2.3. Burst Hydrodynamic Statistics

Figure 4.5 provides an example for the combined high and mid frequency bin (Figure 4.4, panels D and C) discrepancies observed across 22 bursts (panel A) in the 4 statistical measures forming the first direct addition to the decision algorithm. The 4 statistical measures forming the first component of the decision algorithm and their respective equations are defined as:

- 1) The total magnitude change (Figure 4.5, panels D and G) in the burst (25):

$$\Delta M_{x:y} = \max(D_{x:y}) - \min(D_{x:y}) \quad (25)$$

Wherein $\Delta M_{x:y}$ is the total change in magnitude of bin $D_{x:y}$, $D_{x:y}$ is the bin containing the combined frequencies $x:y$, and $x:y$ are the lower and upper bound indexes of the included frequencies of the bin. For example, frequency bin $D_{3:4}$ is the combination of frequency bins 3 and 4 (Figure 4.3 panels H and G), forming the combined high frequency bin.

2) Maximum variance of a 12-second sliding window (Figure 4.5 panels E and H) in the burst (26):

$$S^2_{x:y,max} = \max \left(\frac{1}{n-1} \sum_{i=t-12}^{t+12} (A_i - \mu)^2 \right) , \quad t = 1:N \quad (26)$$

Wherein $S^2_{x:y,max}$ is the maximum variance of a moving 12-second window centered about time index t , A_i is the vector of values from combined frequency bin $D_{x:y}$ corresponding to the 12-second window, μ is the sample mean of A_i , N is the total number of points in the burst (i.e., 2048), and n is the number of points contained in the 12-second window (i.e., 24 as the data was collected at a 2 Hz sampling rate).

3) The kurtosis (Figure 4.5 panels F and I) of the complete burst (27):

$$K_{x:y} = \frac{1}{N\sigma^4} \sum_{i=1}^N (A_i - \mu)^4 \quad (27)$$

Wherein $K_{x:y}$, σ , and μ are the kurtosis, standard deviation, and mean of the combined frequency bin $D_{x:y}$, respectively.

4) Bin energy as a fraction of the total energy (Figure 4.5 panels B and C) in the burst (28):

$$e_j = \sum f_j(x)^2 \quad (28)$$

$$f_j(x) = \sum_{k=0}^{N-1} d_{j,k} * 2^{(-j/2)} * \Psi(2^{-j}x - k) \quad (29)$$

Wherein e_j is the summed energy for detail bin j , $f_j(x)$ is the detail vector for bin j , k is the sample index ranging from 0: $N-1$, N is the total sample size, $d_{j,k}$ is the detail coefficient for bin j at point k , and Ψ is the function of the wavelet defining the transform.

Bursts containing a VGW exhibit statistical responses that can reach over 20x larger than those of non-VGW bursts (Figure 4.5). Thresholds that can demarcate definitive distinctions between bursts with and without VGW events on their own are still not possible for any statistical measure considered in (25-28), however. Comparing the minimum values of bursts with wakes (i.e., black and red markers in Figure 4.5) and the maximum values of the wind-only bursts (i.e., blue markers in Figure 4.5), several measures have instances of wind-only burst statistics close to or even surpassing those of bursts containing VGW events (Table 4-2 and Table 4-3). For the comparisons of the statistical measures, the minimum value for bursts with strong or weak wake events and the maximum value for bursts that are wind only have been used.

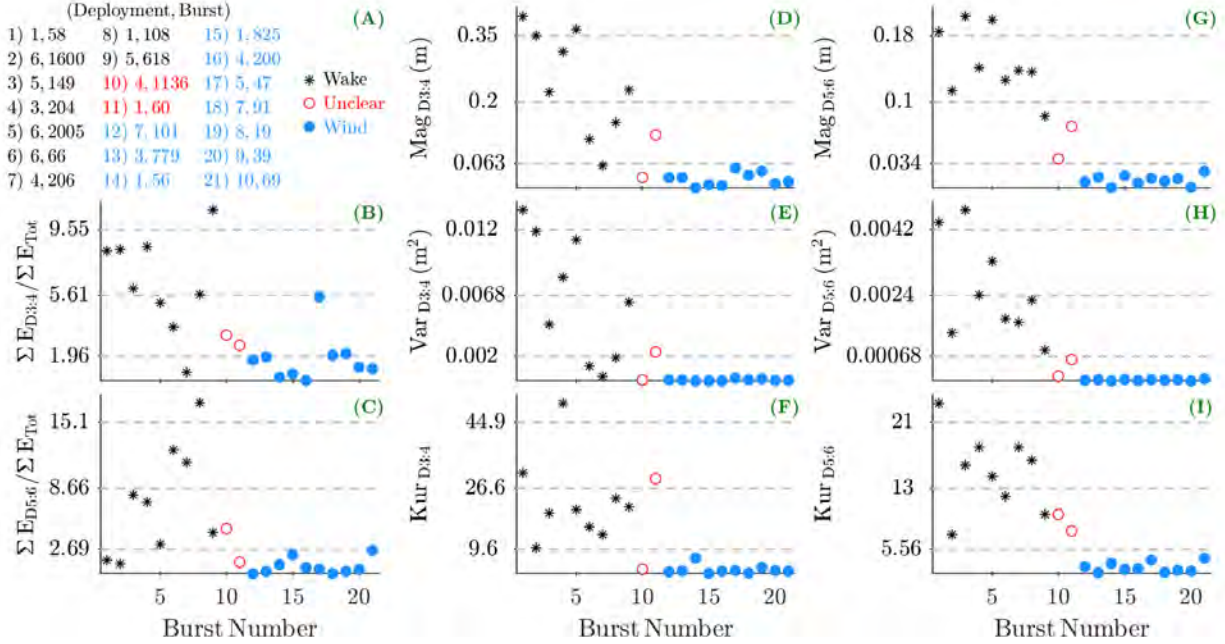


Figure 4.5: Statistical comparison of 10 bursts containing wake events (black), 10 wind-only bursts (blue), and 2 examples of bursts with unusually weak wake events (red). Summaries include total magnitude (panels D and G), maximum variance calculated from a 12-second moving window (E and H), kurtosis (F and I), and bin energies relative to the total energy of the entire signal (B and C).

Table 4-2: Comparison of 4 statistical measures for the combined high frequency bin using the minimum value for bursts with strong or weak wake events and the maximum value for bursts that are wind only.

Measure	Strong Wake	Weak Wake	Wind Only	Empirical Threshold
$\Delta M_{3:4}$	0.06	0.03	0.05	0.035
$S^2_{3:4,max}$	3.5e-4	7.7e-5	2.2e-4	1e-3
$K_{3:4}$	10.0	4.1	7.2	6
$\Sigma E_{3:4}/\Sigma E_{total}$	1.0	2.6	5.5	4

Table 4-3: Comparison of 4 statistical measures for the combined mid frequency bin using the minimum value for bursts with strong or weak wake events and the maximum value for bursts that are wind only.

Measure	Strong Wake	Weak Wake	Wind Only	Empirical Threshold
$\Delta M_{5:6}$	0.09	0.04	0.02	0.1
$S^2_{5:6,max}$	8.4e-4	1.4e-4	6.1e-5	2e-3
$K_{5:6}$	7.4	7.8	4.5	8
$\Sigma E_{5:6}/\Sigma E_{total}$	1.3	1.4	2.6	2.7

To overcome the lack of a single statistical threshold that can definitively ascertain whether a burst contains a VGW event, an aggregation of the various measures across both high and mid combined frequency bins is necessary. The empirical thresholds set for each measure and combined frequency bin are listed in Table 4-4 and Table 4-5 along with the mean value of bursts containing VGW and the maximum value of bursts containing wind only.

Table 4-4: Comparison of 4 statistical measures for the combined high frequency bin using the mean value for bursts with strong or weak wake events and the maximum value for bursts that are wind only.

Measure	Strong Wake	Weak Wake	Wind Only	Empirical Threshold
$\Delta M_{3:4}$	0.25	0.08	0.05	0.035
$S^2_{3:4,max}$	6e-3	1.2e-3	2.2e-4	1e-3
$K_{3:4}$	22.9	16.7	7.2	6
$\Sigma E_{3:4}/\Sigma E_{total}$	6.4	2.9	5.5	4

Table 4-5: Comparison of 4 statistical measures for the combined mid frequency bin using the mean value for bursts with strong or weak wake events and the maximum value for bursts that are wind only.

Measure	Strong Wake	Weak Wake	Wind Only	Empirical Threshold
$\Delta M_{5:6}$	0.15	0.06	0.02	0.1
$S^2_{5:6,max}$	2.5e-3	3.7e-4	6.1e-5	2e-3
$K_{5:6}$	15.0	8.8	4.5	8
$\Sigma E_{5:6}/\Sigma E_{total}$	7.4	3.1	2.6	2.7

The requirement set for finalizing a burst as statistically indicating a VGW event or not was to search for at least 3 threshold exceedances across the magnitude, variance, and kurtosis related measures for both combined frequency bins. If 3 or more exceedances were found out of the possible 6, the burst was labeled as positive with strong confidence. If the burst only managed 1 or 2 exceedances, then the relative energy measure was additionally consulted. If both combined frequency bins contained an energy fraction above the corresponding threshold, the burst was then labeled as positive for a wake, except now with weak confidence. Any bursts not passing this weak confidence criteria (or having 0 exceedances across the magnitude, variance, and kurtosis measures) were assumed as not containing VGW events.

4.2.4. Mid Frequency Bin Alignments

The second direct addition to the decision chain, also utilizing the multiresolution decomposition, is perhaps the most critical as the output it provides is how the algorithm indexes potential wakes for inspection. When considering the effects of the dispersion relation from linear wave theory on a VGW packet containing a wide spectrum of periods, it should be expected that longer period

waves arrive first, followed by arrivals in consecutive increases through the decomposed frequency bins (30):

$$\omega^2 = gk \tanh(kh) \quad (30)$$

$$\omega = \frac{2\pi}{T} \quad (31)$$

Wherein ω is the angular frequency of the wave.

The organization of the frequency bins in such a manner is highly unnatural, and therein presents the needed data point. Figure 4.6 illustrates this point, as the troughs of mid-range frequency bins align sequentially by bin upon the arrival of a wake. To first be considered, troughs must have a minimum relative prominence at least 5% of the most prominent trough in the corresponding bin. All troughs passing this initial threshold are then checked for alignment with the other bins; troughs are considered aligned if the 6th detail bin (D_6) arrives within 30 seconds after the 7th detail bin (D_7) and the 5th detail bin (D_5) arrives within 20 seconds after the D_6 bin. Beyond the 20 and 30 second arrival time thresholds, the exact time separating the trough arrivals between adjacent bins is not conditioned any further. This added flexibility is intended to increase the robustness of the analysis method as confirmed wake arrivals have been observed showing inconsistent separation durations between adjacent bins.

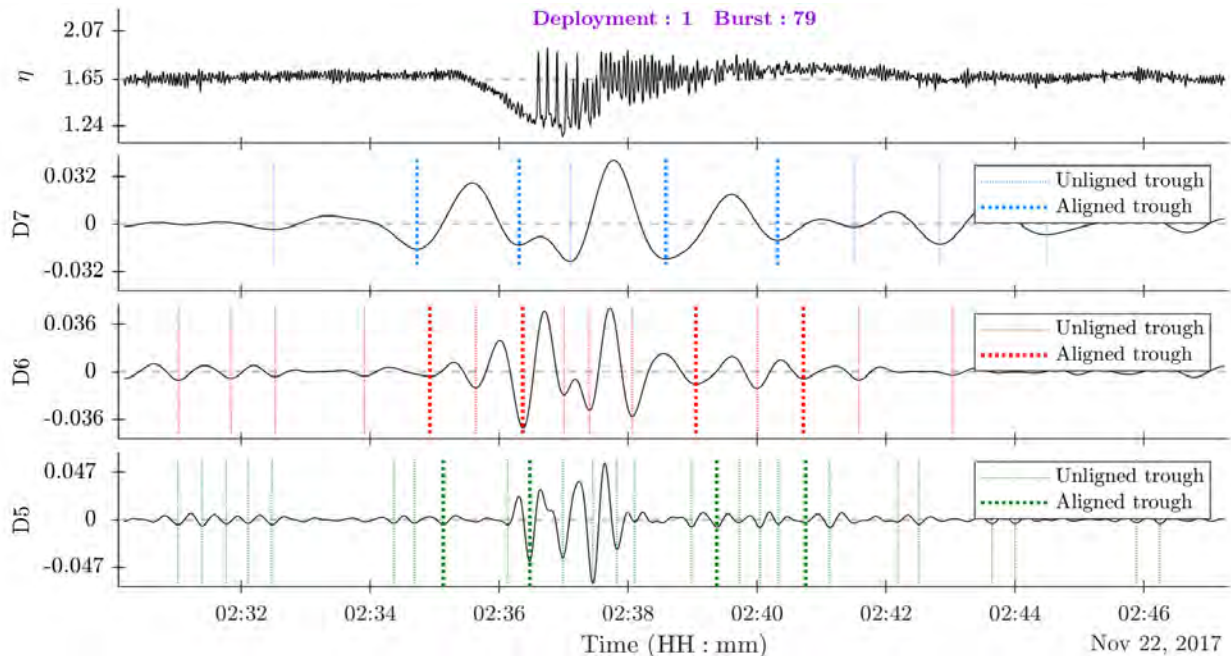


Figure 4.6: Alignments of the 5th, 6th, and 7th detail frequency bins for an arriving wake. Thin lines indicate troughs of at least 5% relative prominence, bold lines indicate trough alignments with potential linkage to a wake arrival event.

Trough alignments in the D_5 - D_7 frequency bins are considered strong indicators of wakes due to the relative scarcity of naturally occurring waves in this mid frequency range. Enclosed bodies of

water such as GB are prone to low frequency motions known as seiches in addition to the standard high frequency wind-driven waves found in nearly all waterways, however very few natural bay processes will concentrate energy into the mid-range of the frequency spectrum. Once an alignment is positively identified, the point is saved according the arrival index of the D_6 trough.

4.2.5. High Frequency Bin Moving Variance

Continuing with the decomposed pressure signal, the third analysis method attempts to locate time indexes in the combined high frequency bin where abrupt changes in signal variance occur. Searching for these spikes in windowed variance is similar to how the moving variance statistic was used during the burst statistics considerations (26).

By running a moving 12-second window, enough time to capture 2 or 3 of the waves along the leading edge of a wake envelope, any wakes that include a high frequency component are rapidly identified. Identification occurs quantitatively by employing threshold up-crossings – as the 12-second windowed variance around a wake is often 50% greater than pre-wake arrival, whenever the mean value of the moving variance window throughout the entire burst is exceeded for more than 20 seconds, the event is recorded as a potential wake (Figure 4.7).

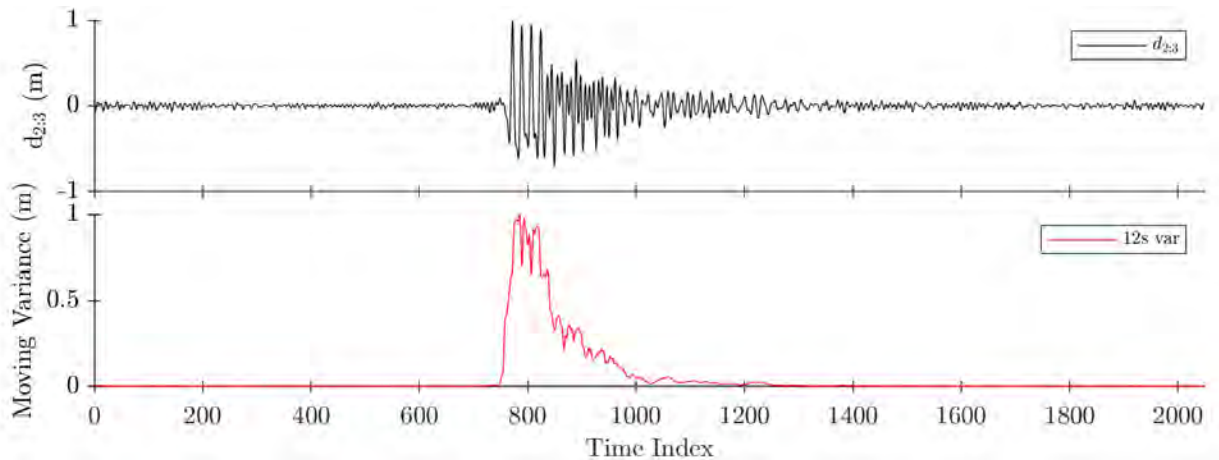


Figure 4.7: Comparing the high frequency bin with the value of a 12-second moving variance window.

4.2.6. Windowed Max Displacement of Water Surface Elevations

Rather than using a short-windowed moving variance calculation similar to the high frequency bin, the fourth criterion added to the decision processes implements a longer sliding window over the smoothed pressure signal, now calculating the total magnitude change during a 90-second window (Figure 4.8).

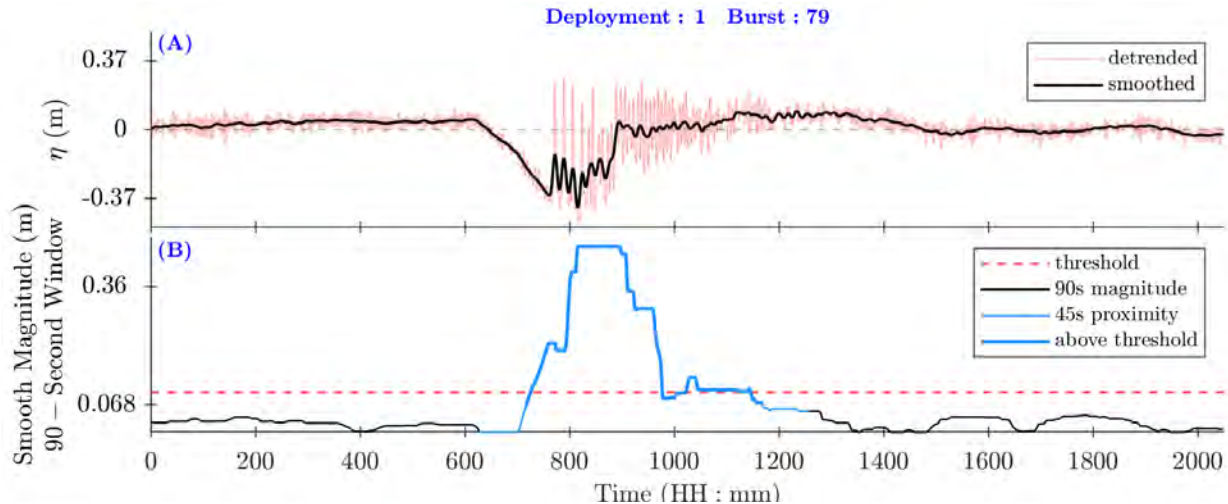


Figure 4.8: A detrended and smoothed pressure signal with a clear VGW arrival (panel A) that has undergone a 90-second moving window max magnitude threshold exceedance inspection (panel B).

By considering the total magnitude change anywhere within the 90 seconds, the goal was to allow for the entire bow component of the wake to be included. During those 90 seconds the extreme low of the drawdown contrasting with the reflexive surge and arrival of the higher frequency components will typically distinguish this timepoint as a likely VGW event arrival. Additionally, choosing to run the window around the smoothed detrended pressure signal also serves to filter out most of the noise caused by background phenomena, further intensifying the relative strength of the actual VGW arrival event.

As with the moving variance of the high frequency bin (Figure 4.7), a threshold exceedance inspection provides the quantitative means to declare the index as a valid wake. An empirical value of 0.07 m was found to successfully separate out VGW events from false positive events that may have otherwise been identified. Due to wakes occasionally presenting highly irregular bow or stern components, likely due to phase issues in the propagating wave packets destructively interacting, it was found that extending the threshold exceedance indexes by 45 seconds out to each side of the exceedance span successfully overcomes any irregularities and provides the desired outcome. Because the algorithm considers output from this inspection as a vector of indexes above or within 45 seconds of an exceedance rather than requiring only the first up crossing index (as with the high frequency variance inspection), ensuring the bow component of the wake is included in the exceedance span prompted the need for a solution to irregular wake behavior.

4.2.7. Velocity Component Span Approach

Wake arrival predictions dependent on cross shore (herein u) and alongshore (herein v) velocity components are far less reliable when compared to the associated pressure signal. Attempts of correlating peak or trough alignments in the smoothed u/v components would logically present a reasonable starting point, however irregularities in the velocity components across different

wake events prevent dependence on this straightforward approach. To overcome these consistency issues, a robust approach was needed that could balance the need for identifying wake arrivals during high uncertainty events while also avoiding overly excessive false-positive predictions.

Rather than directly seeking peaks, troughs, or otherwise large magnitudes that may exist in the signals, the primary focus was instead shifted to extracting spans where the smoothed pressure and velocity components maintained relatively extended periods of unidirectional movement (i.e., long stretches of a positive or negative slope). Spans were first constructed using pairs of consecutive peaks and troughs as shown in Figure 4.9, where green lines indicate positive slope spans and blue the negative slopes.

With the intention of avoiding repeated signal smoothing (and possible obfuscation of important details such as inflection, peak, or trough locations), the spans were instead merged when necessary, via comparisons with adjacent spans in the opposite direction. Beginning with the last span index and iterating back towards the first index, spans in each slope direction for pressure and velocity components were tested via two possible merge conditions – conditions based on a 2- or 3-span series (Table 4-6). If the current index is index “x,” then span x-1 and x-2 would be the spans 1 and 2 indexes before the current index (all with the same slope direction as span x and all in the same component). As the minimum (i.e., first) index is 1, if there is a total of “n” spans for the given slope direction in the given component, the 2-span series could only merge indexes 2:n while the 3-span series could only merge indexes 3:n. The 3-span merge test was performed first and the 2-span test was only performed if the 3-span failed. If a 3-span test resulted in a successful merging, the next iteration index would jump forward by 2 to account for the 2 earlier spans (i.e., x-2:x-1) that were merged with the current. Otherwise, the iteration index would move forward by 1 after 2-span merges or no merges by either test.

Table 4-6: Three- and two-span test condition details.

Condition series	Indexes considered (x is current)	# of spans with matching slope considered	# of spans with opposite slope considered	Total # of spans to potentially merge as one
3-span	x-2:x	3	2	5
2-span	x-1:x	2	1	3

The specific conditions required for initial span merging by each test are as follows:

3-span test

- Positive slope (x is span with index x , $start\ x$ is first magnitude in span x , etc.)
 - $Start\ x > start\ x - 2$
 - $Start\ x - 1 > start\ x - 2$
 - $End\ x > start\ x - 2$
 - $End\ x > start\ x - 1$
 - Max relative magnitude of two associated negative slope spans = 15%
 - Relative to magnitude of max negative span in the component
 - Max duration of the two associated negative slope spans = 15 seconds
 - $\frac{\sum |Increases\ in\ the\ 3\ positive\ spans|}{\sum |Decreases\ in\ the\ 2\ associated\ negative\ spans|} > 3$
 - Ratio of gross change
 - $\frac{[Min(start\ x-1, start\ x)-(start\ x-2)] + [(end\ x)-Max(end\ x-2, end\ x-1)]}{Max(end\ x-2, end\ x-1)-Min(start\ x-1, start\ x)} > 2.5$
 - Ratio of net change

- Negative slope (x is span with index x , $start\ x$ is first magnitude in span x , etc.)
 - $Start\ x < start\ x - 2$
 - $Start\ x - 1 < start\ x - 2$
 - $End\ x < start\ x - 2$
 - $End\ x < start\ x - 1$
 - Max relative magnitude of two associated positive slope spans = 15%
 - Relative to magnitude of max positive span in the component
 - Max duration of the two associated positive slope spans = 15 seconds
 - $\frac{\sum |Decreases\ in\ the\ 3\ negative\ spans|}{\sum |Increases\ in\ the\ 2\ associated\ positive\ spans|} > 3$
 - Ratio of gross change
 - $\frac{[(start\ x-2)-Max(start\ x-1, start\ x)] + [Min(end\ x-2, end\ x-1)-(end\ x)]}{Max(start\ x-1, start\ x)-Min(end\ x-2, end\ x-1)} > 2.5$
 - Ratio of net change

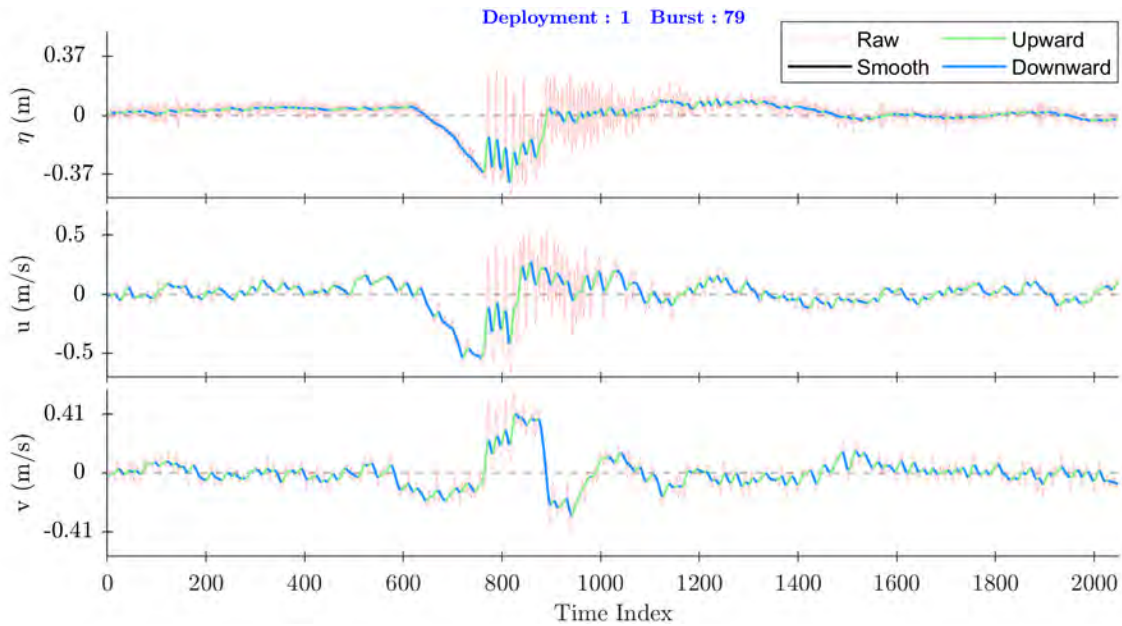


Figure 4.9: Depiction of the velocity span approach where upward moving spans are green and downward spans blue.

2-span test

- Positive slope (x is span with index x , $start\ x$ is first magnitude in span x , etc.)
 - $Start\ x > start\ x - 1$
 - $End\ x > start\ x - 1$
 - Max relative magnitude of the associated negative slope span = 15%
 - Relative to magnitude of max negative span in the component
 - Duration of the associated negative slope span = 15 seconds
 - $\frac{\sum \text{Increases in the 2 positive spans}}{|\text{Decrease in the associated negative span}|} > 3$
 - Ratio of gross change
 - $\frac{(start\ x - start\ x-1) + (end\ x - end\ x-1)}{(end\ x-1) - (start\ x)} > 2.5$
 - Ratio of net change

- Negative slope (x is span with index x , $start\ x$ is first magnitude in span x , etc.)
 - $Start\ x < start\ x - 1$
 - $End\ x < start\ x - 1$
 - Max relative magnitude of the associated positive slope span = 15%
 - Relative to magnitude of max positive span in the component
 - Max duration of the associated positive slope span = 15 seconds
 - $\frac{\sum |\text{Decreases in the 2 negative spans}|}{\text{Increase in the associated positive span}} > 3$
 - Ratio of gross change
 - $\frac{(start\ x-1 - start\ x) + (end\ x-1 - end\ x)}{(start\ x) - (end\ x-1)} > 2.5$
 - Ratio of net change

The relative magnitudes of each span were updated following the primary merging processes, and then a series of 6 secondary merging and trimming operations was performed in the following order:

For all pressure and velocity components

1. Trim spans with magnitudes under 15%, the max magnitude in the given slope direction
2. Merge 2 adjacent spans of same slope direction if:
 - separated by 15 seconds or less
 - there is not a span of either slope direction between them
3. Merge 2 adjacent spans of opposite slope direction at the separation midpoint if:
 - separated by 25 seconds or less
 - there is not a span of either slope direction between them

For pressure component only

4. Trim spans of each slope direction with relative slopes less than 20%
 - Relative to the maximum span slope of the given span slope direction
5. Trim spans of positive slope direction with durations longer than 90 seconds
 - As only spans associated with VGW events are desired, pressure spans with positive slopes lasting longer than the maximum expected duration of post-drawdown surges (about 90 seconds) can be removed from further considerations
 - As drawdown durations are highly variant relative to expected post-drawdown surges, only the positive slope directions were considered for this trimming procedure

For all pressure and velocity components

6. Trim spans of either slope direction unconnected to a span of opposite slope direction
 - Connections defined as spans of a given pressure or velocity component and a given slope direction having a shared start or end point with a span of the opposite slope direction

With the span merging and trimming procedure complete, a list of span connection points in the u/v velocity components was next determined. Table 4-7 lists the connection types for wake events in each direction. The connections are noted as only considering the bow portion of an event due to the bow portion of a wake providing the greatest discrepancy between inbound and outbound wake events. This discrepancy is a function of how closely the respective u/v span connection points are aligned (bow portions are typically closer) and how strong the magnitudes of the u/v span connection points are (bow portions are typically larger). The clearer discrepancy is a result of the bow portion arriving during relatively quiescent hydrodynamic activity while the stern portion arrives as remnants of the bow portion are still present (Figure 4.10).

Table 4-7: Velocity component span connection details for the bow portion of wake events in each transit direction.

Vessel heading	Slopes of connecting spans at bow		Connection type at bow	
	u	v	u	v
Inbound	Positive-Negative	Positive-Negative	Peak	Peak
Outbound	Positive-Negative	Negative-Positive	Peak	Trough

The next step of the velocity inspection begins by indexing each span connection occurrence (i.e., a pseudo peak or trough point). Valid u/v connection indexes must meet the following criteria:

- u component peak connections:
 - have a shared point between positive span ends and negative span starts
 - have a positive slope component at least 10 seconds in duration
 - have a positive slope component with a relative magnitude of at least 20%
- Only 1 of the last 2 conditions is required for index validation
- v component peak connections:
 - have a shared point between positive span ends and negative span starts
- v component trough connections:
 - have a shared point between negative span ends and positive span starts

As VGW event arrivals are expected to exhibit aligned u/v connections, connections of a given smoothed velocity component without a corresponding connection in the other smoothed velocity component may be trimmed from consideration. For this alignment-based trimming to succeed, the location of the peak/trough connection indexes must accurately reflect the true location of peaks/troughs in the smoothed velocity component. Accurate representations of the true locations for the peak/trough are generally observed, however bursts containing velocity components that resemble a plateau after signal smoothing are not uncommon (Figure 4.11, panel B). Plateaus in the smoothed signal occur when velocity components do not exhibit the greatest magnitudes at the start of the bow/stern portions with the magnitudes then decreasing with time. Because the largest wake waves, and by extension the largest velocity component magnitudes, are expected to arrive at the onset of the bow/stern portions (Figure 4.10), instances of maximum magnitudes found later than expected indicate an issue with the recorded component signal.

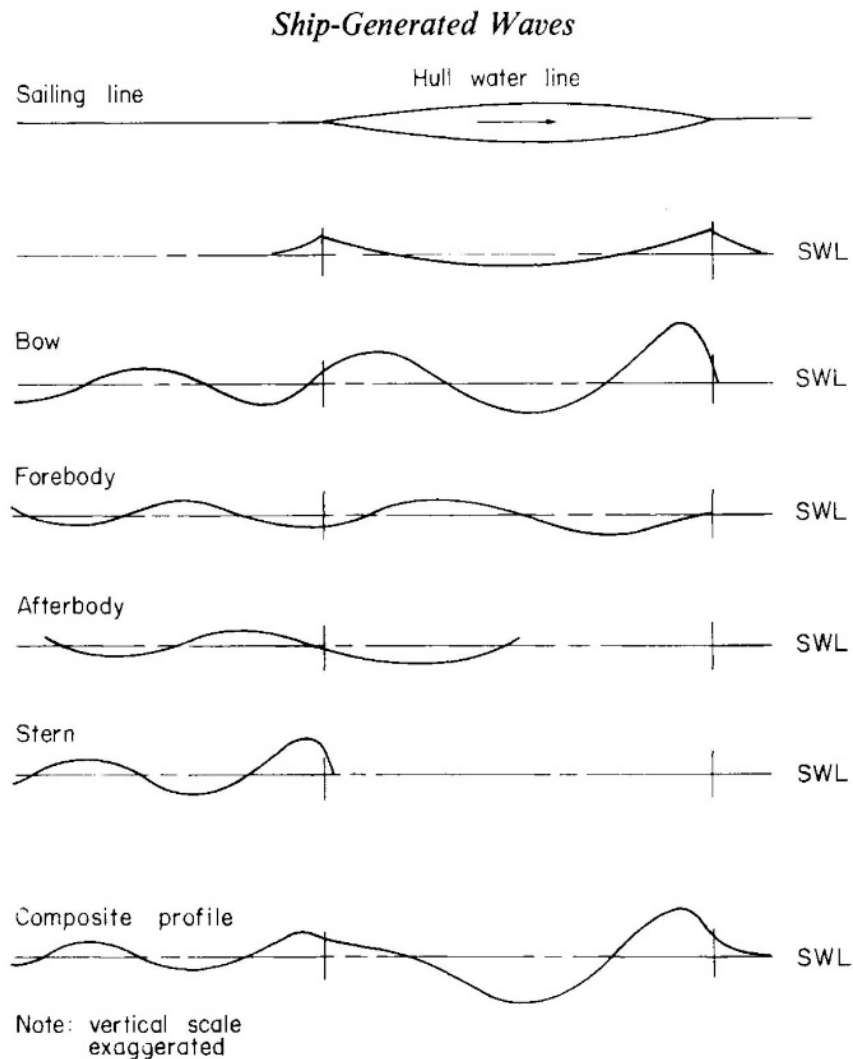


Figure 4.10: Visual representation for the various components of a vessel-generated wake event, notably the bow and stern portions. Figure adapted from Sorensen (1973).

The main instigators of such issues are attributable to:

- hydrodynamic interferences superimposing with the wake event and thereby altering the wake's true signal (i.e., interference resulting from the arrival of a different wake event);
- coincidental Doppler effect undermeasuring during the initial waves of the bow/stern portion;
- the sampling frequency is low enough to where the component magnitudes for some waves were not accurately measured after peak values occurred between successive ADCP measurements;
- wave reflections at the dike embankment spawn standing wave interferences.

Considering the ADCP wave burst mode used in data collection had a maximum sampling frequency of 2 Hz, a suboptimal sampling frequency is likely the root cause of smoothed component signal plateaus whenever a superimposed or standing wave interference is not present. Because occurrences of signal plateaus effectively shift the location of the peak/trough span connection away from its true location as noted earlier, corrections are therefore necessary.

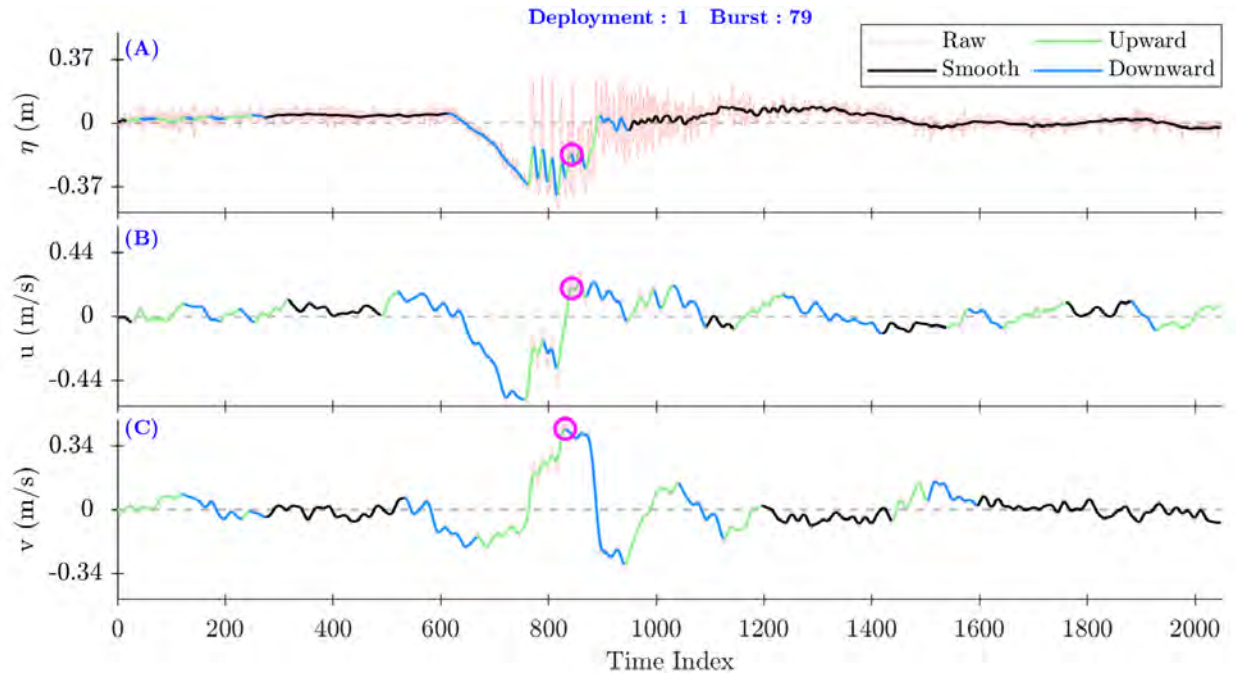


Figure 4.11: Outcome of the span merging and trimming process designed to identify periods of extended unidirectional velocity behavior. The connection point identified in the u component is noted as having been shifted backward during corrective analysis after initially appearing later than expected. The shift is observed by the mid-span location of the u component connection point (circled) instead of an end of span location as would normally be expected. The correction positions the u and v component connections within the necessary proximity to be considered a potential wake; the wake passes the inspection.

When plateaus in the slope of the smoothed velocity component are identified, the point is continually shifted backward each previous wave having a magnitude similar to that of the current wave. Shifts will begin with the last wave index of the corresponding smoothed velocity component span (i.e., at the location of the wave with peak magnitude during the span) and move earlier towards the middle of the span (Figure 4.10, panel B). Steps for determining whether to shift a connection point index backward are:

1. Isolate the waves contained in the smoothed velocity component signal span
2. Normalize peak wave magnitudes with respect to the max magnitude during the span
3. Shift the connection point pack to the peak magnitude of the previous wave while the:
 - magnitude of the previous wave is within 40% of the peak magnitude
 - normalized magnitude change from the current to previous wave is $< 25\%$

A change in smoothed velocity component wave magnitudes that fails either of the 2 conditions in the 3rd step (above) indicates the next wave is no longer part of the wake packet. The process of active index correction is a direct response for needing to overcome a velocity component signal irregularity that could otherwise derail positive identification.

Following the connection index shift corrections (if any were necessary), a sorting process then ensures only valid connection indexes that correspond to a connection index in the opposite velocity component are kept. The sorting is completed by ensuring:

- Connection indexes in one component correspond to connection indexes in the other component
 - Wake events will reach peak magnitudes in each velocity component within relatively close proximity (about 20 seconds at most, usually less than 10 seconds)
- Connection indexes must align within 30 seconds of a pressure span starting index
 - VGW events observable in the velocity components will be observable in the pressure
- Only 1 vessel per each transit direction can exist within a 3-minute span
 - Vessel traffic in the HSC is spaced to avoid vessels overtaking one another

Any velocity connection indexes remaining after the corrective procedures are completed are then passed along to the decision algorithm as potential VGW arrival times

4.2.8. Decision Synthesis

On completion of each of the 5 data analysis methods discussed in Sections 4.2.3 - 4.2.7, results were fed back into the main algorithm that then initiated the synthesis of a final decision for conclusive wake identifications. At this stage comes the first reference to the AIS records; up until now the decision chain has solely relied on measured hydrodynamic data. Vessel records timestamped between the starting and ending time index of the given ADCP burst are identified and sorted by ship MMSI into transit lists. MMSI, or Maritime Mobile Service Identity, is the internationally recognized unique identification number given to each vessel. Each transit has the heading direction gauged by general direction of travel, and with this heading, an initial prediction is made of the when the vessel's wake should manifest in the ADCP measured data. This timing prediction is created by interpolating the known path of the vessel and using the interpolation to estimate when a specific latitude threshold is reached. Although a (heading-specific) fixed point is used, predictions tend to be within 5 minutes or less regardless of ship type or speed.

Identification begins via looping through each mid frequency alignment index (Section 4.2.4). The mid frequency alignment indexes are noted as composing the "anchor" data points that guide the decision algorithm's iterations as an acknowledgement that these alignments provide the only fundamental behavior observed to occur universally across the full spectrum of wake events.

A series of attempts are then made by the algorithm to find the best matches, if any exist, from results of the various analysis methods (including AIS-generated predictions) for each alignment index. The algorithm is designed to allow results from each method to be used only once, namely by the optimally matching alignment index.

Any disagreements between data sources are found and addressed, such as AIS headings not matching the heading predicted by the velocity span method or the AIS time prediction poorly matching the other method prediction indexes (i.e., the predictions are off by more than 5 minutes). Any disagreements not resolved are then designated and set aside. Disagreements are not simply tossed to ensure wakes unable to attain positive identification are still recognized as potential events, thereby avoiding erroneously identifying 2 interfering VGW events as 1 event. These lingering disagreements may result in the over exclusion of some VGW events that truly are just a single vessel after registering possible interference with a false-positive event (i.e., the disagreeing index). Considering the data collection period lasted for nearly a year, however, the final sample size should still contain enough VGW events to where the erroneously excluded events do not impact the fidelity of conclusions made during final analysis.

A final verdict is rendered by the algorithm on the basis of how complete the agreement is between each analysis method, whether the wake was likely to have experienced truncation after arriving too close to the start or end of a burst, and whether the wake likely experienced interference from the wake of a different ship after crossing paths near the site. For a VGW event to be used in analysis, the verdict must:

- Have full agreement across all inspection methods (Sections 4.2.3 - 4.2.7)
- Recognize an AIS record corresponding to the VGW event that
 - Results in an event arrival time prediction within 5 minutes
 - Does not have any key vessel specification information missing
- Indicated that the entirety of the wake occurred within the bounds of an ADCP burst
- Indicate no chance of interference between the VGW event with another

5. RESULTS AND DISCUSSION

The following results and associated discussion are for a subset of 200 separate wake events recorded across 735 successive data bursts taken from the roughly 17,000 bursts in total. The first burst begins on March 13th, 2018 at 20:06:01, while the last burst ends on March 26th, 2018 at 14:13:04. Vessel specifications correlated to VGW events are as provided by the USCG; any specification data not contained in the USCG dataset, including all summer deadweight tonnage values, were pulled from websites hosting publicly accessible AIS information [Marinetraffic, 2019; Vesselfinder, 2019]. Two wakes, one from each heading direction, are first presented to highlight the hydrodynamic differences resulting from either event. Each of the 2 research questions are then addressed preliminarily using analysis results from the VGW event subset.

5.1. Wake Hydrodynamics of the Two Transit Directions

5.1.1. Inbound

An isolated inbound wake event is observed between about 19:13-19:17 in Figure 5.1. The wind-driven hydrodynamics provided for perspective are from the timespan between about 19:22-19:26, well after the wake event had subsided and the site had returned to quiescent conditions.

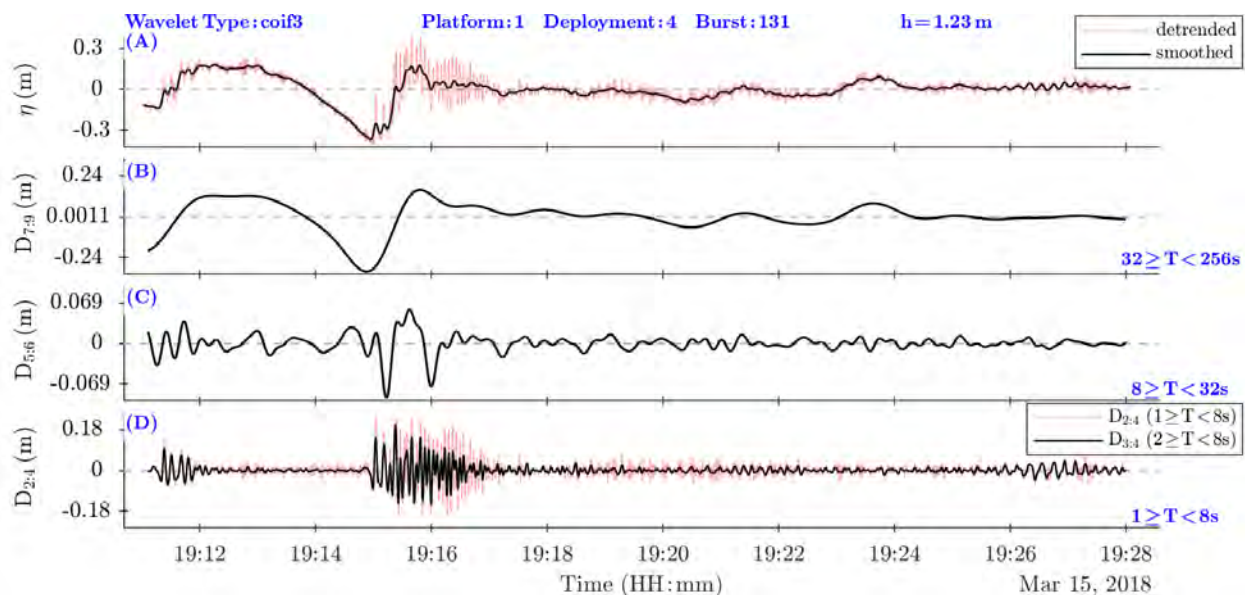


Figure 5.1: Multiresolution analysis of a burst with an inbound wake event between 19:13-19:17. For comparison to quiescent conditions, a comparable timespan between 19:22-19:26 was selected.

Figure 5.2 illustrates the contrasting current velocity directions and magnitudes observed at the site during and after the inbound wake event recorded in Figure 5.1. Table 5-1 and Table 5-2 summarize key hydrodynamic statistics from each of the velocity bins in Figure 5.2. In the “Difference” row (Table 5-1, row 4), positive velocity values (columns 2-4) indicate a greater inbound VGW event-driven current value while negative values indicate a greater wind-driven current value. In the “Difference” row (Table 5-2, row 4), positive velocity frequency values (columns 2-5) indicate a greater frequency in the inbound VGW event-driven current while negative values indicate a greater frequency in the wind-driven current. Just under 50% of the quiescent current direction measurements were between 140-230°, indicating the background current direction to be roughly parallel with the shoreline (i.e., 210°) and flowing towards the HSC.

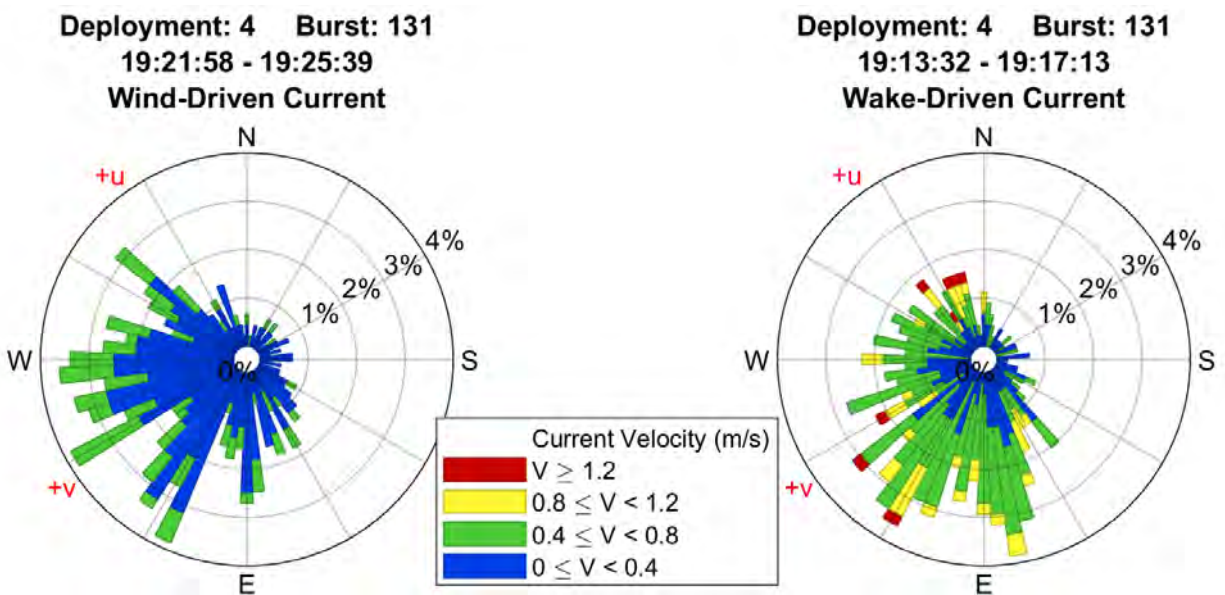


Figure 5.2: Wind rose styled plots of the quiescent wind-driven current (left) compared to the current resulting from an inbound wake event (right). Both hydrodynamic periods were recorded in the same 17-minute burst of ADCP data.

Table 5-1: Comparison of velocity statistics during and after (wind waves only) an inbound wake event.

Current Driver	Velocity (m/s)				Direction (°)		
	Max	Mean	Std. Dev.	At Max Vel.	Mean	Std. Dev.	Mode
Wind	0.79	0.29	0.15	277.6	201.5	72.8	210
Inbound VGW	1.65	0.5	0.27	109.8	212.5	74.7	280
Difference	0.86	0.21	0.12	-167.8	11.0	1.9	70

Table 5-2: Comparison of frequency of occurrence and mean direction per velocity bin during and after (wind waves only) an inbound wake event.

Current Driver	Frequency (%) per Velocity (m/s) Bin				Mean Direction (°) per Velocity (m/s) Bin			
	V<0.4	0.4≤V<0.8	0.8≤V<1.2	V≥1.2	V<0.4	0.4≤V<0.8	0.8≤V<1.2	V≥1.2
Wind	78.3	21.7	0	0	201.8	200.5	-	-
Inbound VGW	37.9	50.6	9.7	1.8	209.7	216.5	212.9	157
Difference	-40.4	28.9	9.7	1.8	7.9	16.0	-	-

A considerable strengthening in current velocity is clearly observed during the wake event, as well as a slight coincident shift in mean current directions. When split into the draw down (i.e., partial low-frequency Bernoulli wave) and surface wave (i.e., high-frequency Havelock waves) components, the inbound VGW-driven current is observed to actually consist of 2 distinct, time-dependent behaviors (Figure 5.3, Table 5-3, and Table 5-4). Splitting the wake event (Figure 5.2, right panel) into the separate components thus allows for higher resolution comparisons to be made, both when comparing the wake event with quiescent conditions and when contrasting the 2 different wake component behaviors against each other.

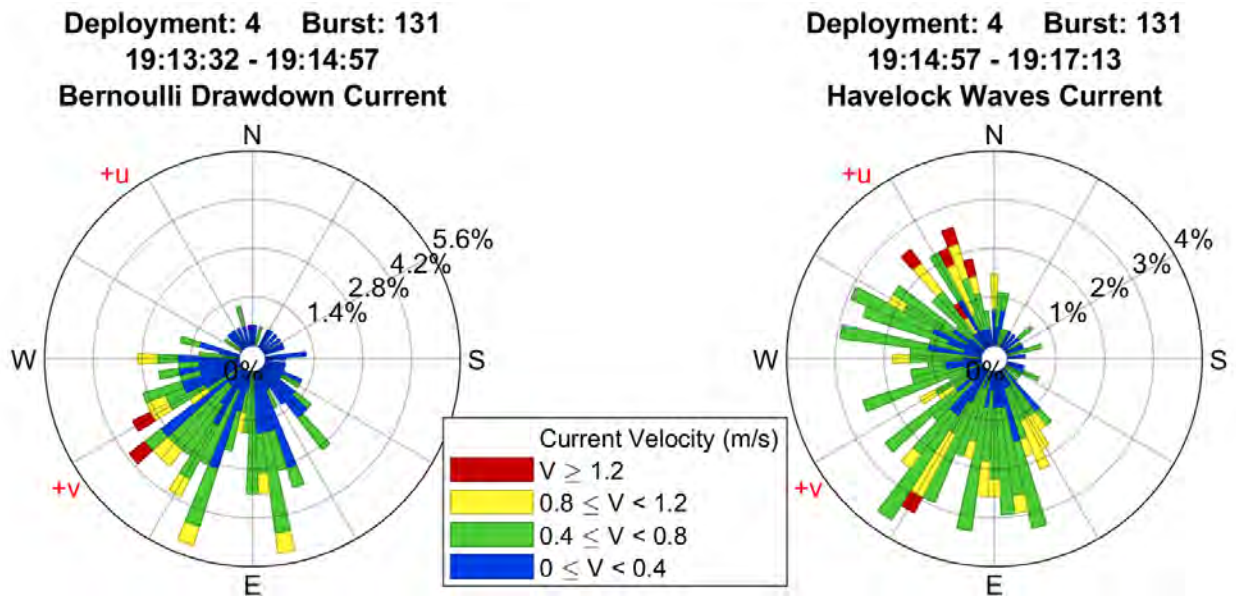


Figure 5.3: Wind rose styled plots of the current during the two main wake components, the low-frequency Bernoulli wave drawdown (left) and the high-frequency Havelock surface wave packet (right).

Table 5-3: Comparison of velocity statistics between the low frequency drawdown and high frequency surface wave components of the inbound wake event.

Current Driver	Velocity (m/s)				Direction (°)		
	Max	Mean	Std. Dev.	At Max Vel.	Mean	Std. Dev.	Mode
Wind	0.79	0.29	0.15	277.6	201.5	72.8	210
Drawdown	1.23	0.42	0.25	217.7	230.2	70.8	250
Difference	0.44	0.13	0.1	-59.9	28.7	-2.0	40
Surface Waves	1.65	0.56	0.27	109.8	201.5	75.0	235
Difference	0.86	0.27	0.12	-167.8	0	2.2	25

Table 5-4: Comparison of frequency of occurrence and mean direction per velocity bin during the low frequency drawdown and high frequency surface wave component of an inbound wake event.

Current Driver	Frequency (%) per Velocity (m/s) Bin				Mean Direction (°) per Velocity (m/s) Bin			
	V<0.4	0.4≤V<0.8	0.8≤V<1.2	V≥1.2	V<0.4	0.4≤V<0.8	0.8≤V<1.2	V≥1.2
Wind	78.3	21.7	0	0	201.8	200.5	-	-
Drawdown	53.8	38.6	6.4	1.2	223.5	239.5	233.5	214.0
Difference	-24.5	16.9	6.4	1.2	21.7	39.0	-	-
Surface Waves	27.8	58.2	11.7	2.2	193.1	207.0	205.8	138
Difference	-50.5	36.5	11.7	2.2	-8.7	6.5	-	-

Both the drawdown and surface wave phases of an inbound VGW event have considerably different current velocity magnitudes relative to quiescent conditions, and to a lesser extent between themselves:

- The maximum and mean current velocities (Table 5-3) are roughly:
 - 50% stronger than quiescent magnitudes during the drawdown phase
 - 100% stronger than quiescent magnitudes during the surface wave phase
- The proportion of current velocities under 0.4 m/s present clear contrasts (Table 5-4), as the fraction of magnitudes below 0.4 m/s compose:
 - 78% of the quiescent period
 - 54% of the drawdown phase
 - 28% of the surface waves phase
- The surface waves create magnitudes at or above 0.8 m/s at a rate twice that of the drawdown (Table 16b), as approximately:
 - 7.5% of the 90-second drawdown is above 0.8 m/s
 - 14% of the 135-second surface wave phase is above 0.8 m/s

The greatest deviation from the quiescent current direction was during the surface wave phase, however this is partly due to the quiescent current flowing towards the HSC and thus coincidentally matching the flow direction observed during the drawdown. As the drawdown is the result of water surface displacements emanating from the vessel, the current flow during this event will invariably concentrate in the direction of the HSC regardless of quiescent flow directions. Additional current direction results include:

- 49% of the quiescent current direction measurements were between 140-230°
- 72% of the drawdown phase current direction measurements were between 180-300°
- The current during the surface wave phase was split into 2 main oscillatory directional bins:
 - 34% between 90-180° (i.e., around the +u direction)
 - 46% between 210-300° (i.e., between +v and -u)
- The max cross-shore velocity magnitude, 1.65 m/s, was within 10° of shore-normal (i.e., +u) and occurred during the surface wave phase
- The max alongshore velocity magnitude, 1.23 m/s, was within 8° of shore-parallel towards the HSC (i.e., +v) and occurred during the drawdown phase

5.1.2. Outbound

An isolated outbound wake event is observed between about 16:33-16:38 in Figure 5.4. The wind-driven hydrodynamics provided for perspective are from the timespan between about 16:27-16:32, well before the wake event had started and while the site experienced quiescent conditions.

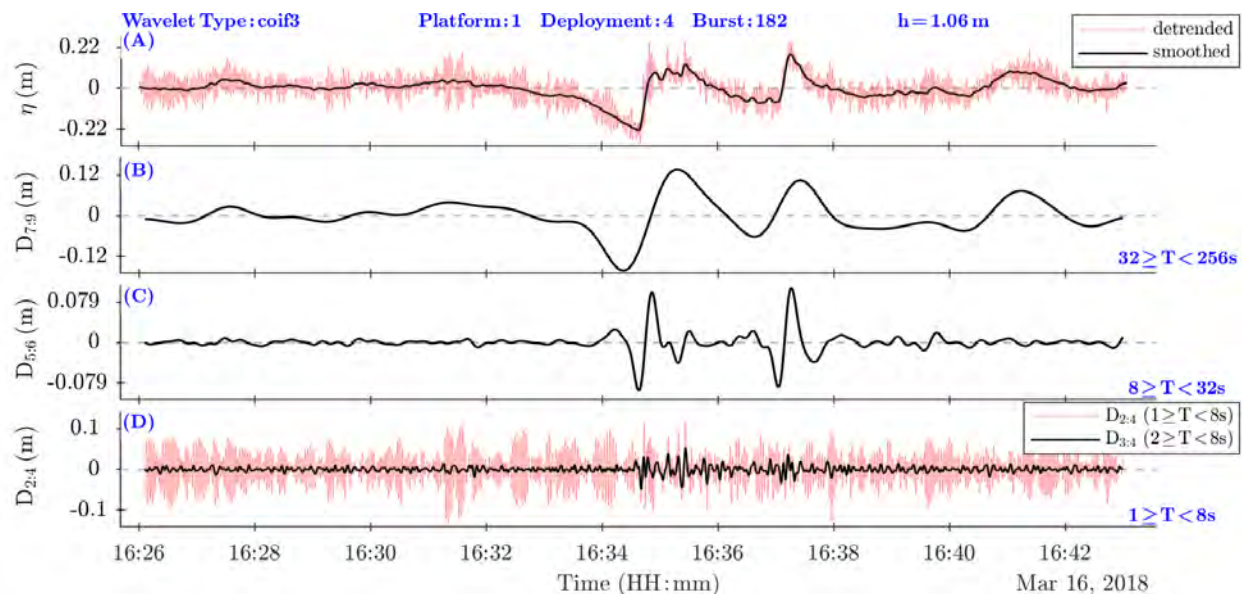


Figure 5.4: Multiresolution analysis of a burst with an outbound wake event between 16:33-16:38. For comparison to quiescent conditions, a comparable timespan between 16:27-16:32 was selected.

Figure 5.5 illustrates the contrasting current velocity directions and magnitudes observed at the site before and during the outbound wake event shown in Figure 5.4. Table 5-5 and Table 5-6 summarize key hydrodynamic statistics from each of the velocity bins in Figure 5.5. In the “Difference” row (Table 5-5, row 4), positive velocity values (columns 2-4) indicate a greater outbound VGW event-driven current value while negative values indicate a greater wind-driven current value. In the “Difference” row (Table 5-6, row 4), positive velocity frequency values (columns 2-5) indicate a greater frequency in the outbound VGW event-driven current while negative values indicate a greater frequency in the wind-driven current. Just under 40% of the quiescent current direction measurements were between 60-150°, indicating an onshore background current direction (i.e., 120°).

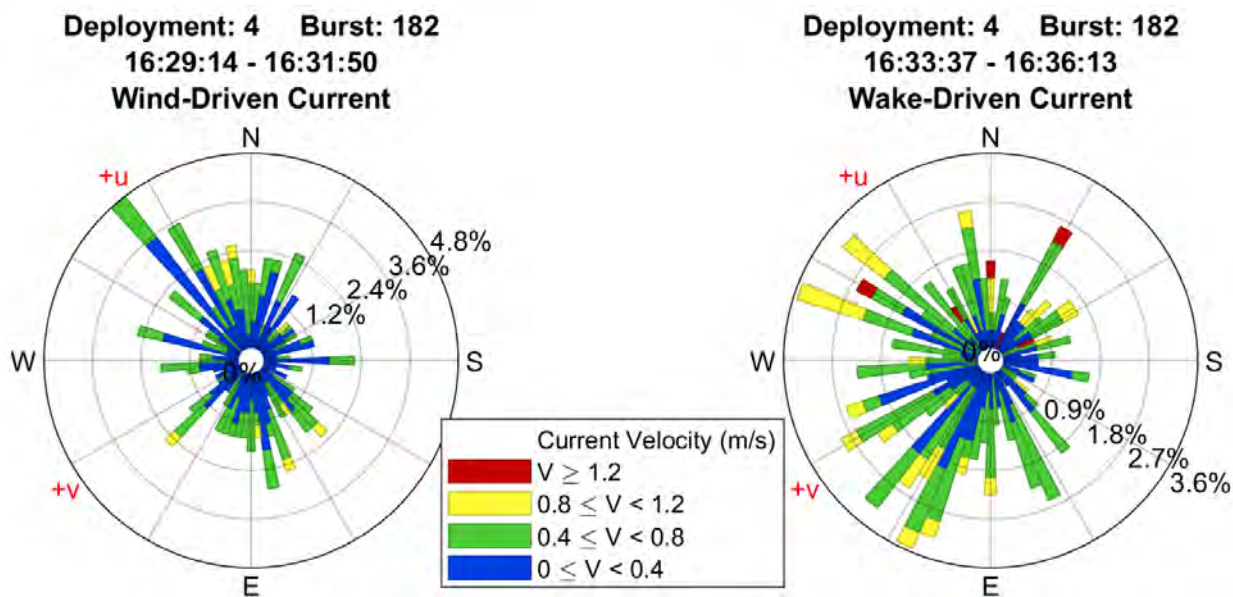


Figure 5.5: Wind rose styled plots of the quiescent wind-driven current (left) compared to the current resulting from an outbound wake event (right). Both hydrodynamic periods were recorded in the same 17-minute burst of ADCP data.

Table 5-5: Comparison of velocity statistics during and after (wind waves only) an outbound wake event.

Current Driver	Velocity (m/s)				Direction (°)		
	Max	Mean	Std. Dev.	At Max Vel.	Mean	Std. Dev.	Mode
Wind	1.04	0.39	0.2	114.1	175.8	96.8	130
Outbound VGW	1.36	0.49	0.26	92.3	181.9	90.3	160/245
Difference	0.32	0.1	0.06	-21.8	6.1	-6.5	20/120

Table 5-6: Comparison of frequency of occurrence and mean direction per velocity bin during and after (wind waves only) an outbound wake event.

Current Driver	Frequency (%) per Velocity (m/s) Bin				Mean Direction (°) per Velocity (m/s) Bin			
	V<0.4	0.4≤V<0.8	0.8≤V<1.2	V≥1.2	V<0.4	0.4≤V<0.8	0.8≤V<1.2	V≥1.2
Wind	57.8	38.3	3.8	0	175.0	177.2	173.7	N/A
Outbound VGW	39.4	48.7	9.9	1.9	187.6	185.3	161.1	85.9
Difference	-18.4	10.4	6.1	1.9	12.6	8.1	-12.6	N/A

A slight strengthening of the current velocity magnitudes is observed during the wake event, as well as a coincident shift in current direction. As with the inbound event, partitioning the outbound VGW event (Figure 5.5, right panel) into the 2 main components allows for higher-resolution insights into the different hydrodynamic conditions present during the wake (Figure 5.6, Table 5-7, and Table 5-8).

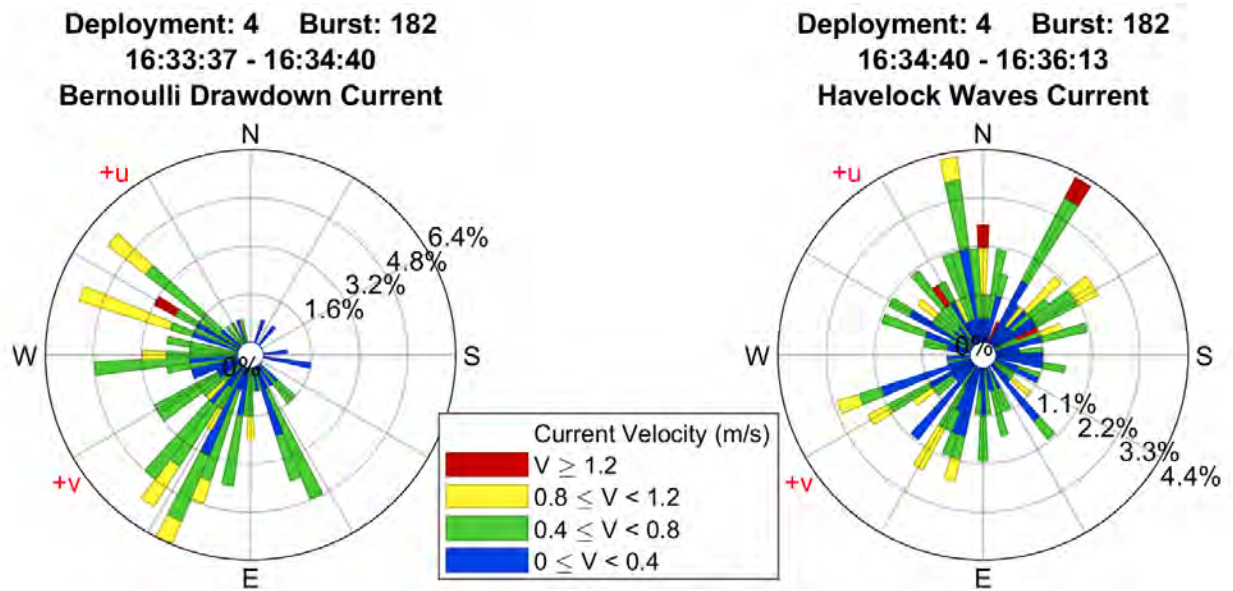


Figure 5.6: Wind rose styled plots of the current during the two main wake components, the low-frequency Bernoulli wave drawdown (left) and the high-frequency Havelock surface wave packet (right).

Table 5-7: Comparison of velocity statistics between the low frequency drawdown and high frequency surface wave components of the outbound wake event. Each component “Difference” row is relative to the quiescent, wind-driven conditions.

Current Driver	Velocity (m/s)			Direction (°)			
	Max	Mean	Std. Dev.	At Max Vel.	Mean	Std. Dev.	Mode
Wind	1.04	0.39	0.2	114.1	175.8	96.8	130
Drawdown	1.23	0.52	0.24	152.1	215.8	60.3	245
Difference	0.19	0.13	0.04	38.0	40.0	-36.5	115
Surface Waves	1.36	0.48	0.27	92.3	159.4	99.6	60/100
Difference	0.32	0.09	0.07	-21.8	-16.4	2.8	-70/-30

Table 5-8: Comparison of frequency of occurrence and mean direction per velocity bin during the low frequency drawdown and high frequency surface wave component of an outbound wake event. Each component “Difference” row is relative to the quiescent, wind-driven conditions.

Current Driver	Frequency (%) per Velocity (m/s) Bin				Mean Direction (°) per Velocity (m/s) Bin			
	V<0.4	0.4≤V<0.8	0.8≤V<1.2	V≥1.2	V<0.4	0.4≤V<0.8	0.8≤V<1.2	V≥1.2
Wind	57.8	38.3	3.8	0	175.0	177.2	173.7	-
Drawdown	30.2	57.9	11.1	0.8	217.2	219.0	199.7	152.1
Difference	-27.6	19.6	7.3	0.8	42.2	41.8	26.0	-
Surface Waves	45.5	42.2	9.6	2.7	174.3	206.1	135.4	72.6
Difference	-12.3	3.9	5.8	2.7	-0.7	28.9	-38.3	-

Each phase of the wake event was distinct from the quiescent conditions, however more so in current velocity directions than magnitudes. Comparing the quiescent and outbound VGV component velocity magnitudes and contrasting the 2 wake components against each other indicate that:

- The max velocity magnitudes were 18% and 33% greater during the drawdown and surface wave phases relative to the quiescent period, respectively (Table 5-7)
- The mean velocity magnitude was about 31% and 23% greater than the mean quiescent magnitude during the drawdown and surface wave phases, respectively (Table 5-7)
- Although the drawdown phase had a slightly greater mean magnitude, the surface wave phase had a similar fraction of magnitudes at or above 0.8 m/s (Table 5-8)
 - 11.9% of the roughly 60-second drawdown had magnitudes at or above 0.8 m/s compared to 12.3% of the roughly 90-second surface wave phase
 - Both wake phases had rates of magnitudes at or above 0.8 m/s approximately 3 times larger than the 3.8% of the 150-second quiescent period

- The surface wave phase contained the largest proportion of magnitudes over 1.2 m/s (Table 5-8)
 - 2.7% of surface waves were above 1.2 m/s, compared to 0.8% of the drawdown and no values during the quiescent conditions

The current direction patterns observed during the quiescent period, wake drawdown phase, and wake surface wave phase were highly variant, notably due to the unique hydrodynamics present during an outbound VGW event. Rather than the standard shore-normal wave approach, outbound VGW events refract around the site shoreline in a shore-parallel manner (i.e., in the -v direction). The resulting current direction observations include:

- The quiescent condition was fairly spread across all directions, however the directions with maximum frequency were in the onshore direction (Figure 5.5, left panel)
- 90% of the drawdown was within 90° of -v, shore-parallel towards the HSC (Figure 5.6, left panel)
- 61% of the surface wave phase oscillated within 45° of shore parallel headings (Figure 5.6, right panel)
 - 33% within 45° of +v
 - 28% within 45° of -v
- 100% of the current magnitudes above 1.2 m/s during the surface wave phase were between 25-125° (Figure 5.6, right panel)
 - Due to currents at the offshore platform refracting towards the shore at a -v heading

5.1.3. General Discussion

The current direction and magnitude details discussed in Sections 5.1.1 and 5.1.2 reflect the hydrodynamics expected during VGW events from transits in both inbound and outbound directions. Drawdowns from each event gravitated towards the HSC, however the outbound events resulted in an average direction just 5° over +v, 15° closer than the average direction of inbound events (left panels of Figure 5.3 and Figure 5.6 and Table 5-3 and Table 5-7). This 15° split in mean drawdown directions is a natural outcome considering the outbound vessels approach from the Northwest and inbound vessels approach from the South (Figure 3.1).

The different approach directions yield an important caveat in how the wakes were delineated, specifically due to the dissimilar nature of the bow and stern wake component interactions (Figure 4.10) during each VGW event. As can be seen in Figure 5.1, the inbound wake arrives as a relatively continuous event, with the bow and stern components only distinguishable by two prominent troughs in the mid frequency bin (Figure 5.1, panel C). These troughs arrive at around 19:15:15 and 19:60:00, and are therefore separated by about 45 seconds. Outbound wakes, in contrast, resemble 2 discontinuous events where the bow and stern components are much more clearly defined. In Figure 5.4, each panel presents a clear split in hydrodynamic impacts as the bow arrives at 16:34:40 while the stern arrives 140 seconds later at 16:37:00. This considerable change to continuity is likely due to the close proximity of the outbound vessel with the shoreline

parallel to the HSC. The interaction between the shoreline and the confined wake delays the stern arrival through shoaling and refraction processes, resulting in greater separation between the components. Figure 5.7 illustrates this interaction for an inbound vessel having already passed the platform site and traveling along the shoreline [Tate et al., 2008]. The current velocity disturbance measured in the wake section to the right of the vessel is nonsymmetric with the disturbance to the left; the trailing edge for the right half of the wake event lags behind the corresponding edge for the left half. This lag leads to a longer distance between the bow-related leading edge and stern-related trailing edge of the disturbance, yielding the additional 100 seconds observed between the outbound bow and stern components.

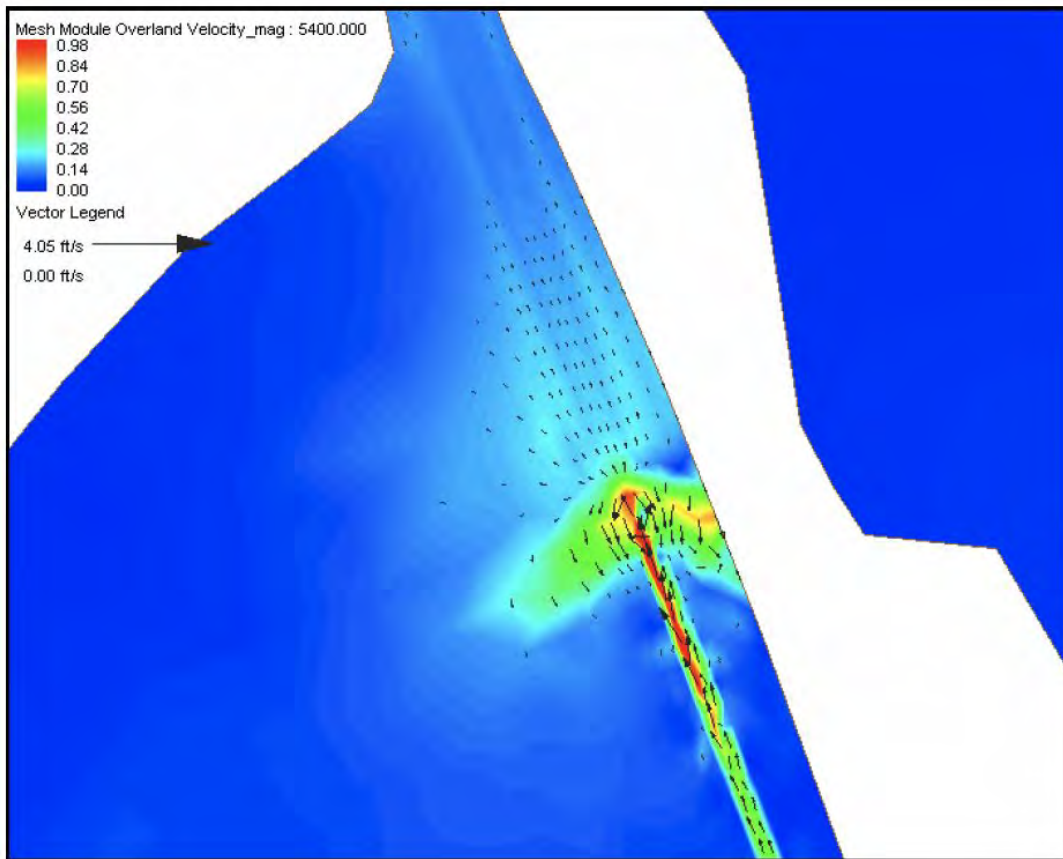


Figure 5.7: Numerical model output of a wake disturbance field for an inbound vessel defined using current velocities. The right half of the disturbance appears to lag behind the left half due to the influence of the adjacent boundary. Figure adapted from Tate et al. (2008).

Because of this discontinuity in bow and stern components of outbound wakes, the analysis in Section 5.1.2 only considers the bow portion of the wake (i.e., the event is truncated at 16:36:13 rather than 16:38:00). This truncation is intended to isolate the surface wave phase as much as possible, as the hydrodynamics of the stern component drawdown phase would otherwise obfuscate the hydrodynamics unique to the surface wave phase.

Unlike the drawdowns, the surface wave components of the VGW events impacted the site along completely different axes (right panels of Figure 5.3 and Figure 5.6 and Table 5-3 and Table 5-7). The inbound surface waves arrived on a shore-normal wave attack angle, while the refracting outbound surface waves traveled shore-parallel. A major difference between the VGW events was the form of the surface waves; inbound waves arrived unbroken from the relatively deeper offshore direction while the outbound waves, trapped and refracting along the shoreline surfzone, propagated as a disorganized packet of broken waves. The effects of this wave structure disparity can be understood by comparing the high frequency bin of the combined multiresolution analysis (i.e., 1-8 second wave periods), where the inbound event (Figure 5.1, panel D) records a surface wave component possessing considerably more wave energy relative to the high frequency bin of the outbound event (Figure 5.4, panel D). Using the ability of multiresolution analyses to quantify the signal energy present in each frequency bin (28), this translates to the high-frequency bin containing 36% of the energy measured during the inbound wake event but only 16% of the outbound wake energy.

A secondary impact of the inbound surface waves propagating as an organized and unbroken wave packet is the greater velocity magnitudes contained in the high frequency waves relative to the outbound wake surface waves (Table 5-3, Table 5-4, Table 5-7, and Table 5-8). The inbound surface waves recorded maximum and mean velocities 21% and 16% greater than the outbound surface waves, respectively. Additionally, outbound surface wave current magnitudes were only at or above 0.4 m/s for 55% of the event as compared to the 72% of inbound wakes. The extended periods of greater current velocity magnitudes during inbound VGW events results in increased erosion and corollary sediment transport rates at the site.

5.2. Correlating AIS Vessel Data with Observed Wake Characteristics

For the 200 positively identified VGW events in the burst subset, correlations were performed using vessel specifications including length, beam, draft, summer deadweight tonnage, gross deadweight tonnage, block coefficients, and Froude numbers. The specifications were correlated to hydrodynamic statistics including total energy (4), significant wave height, max wave height, mean period, drawdown duration, drawdown magnitude, max u component velocity, and max v component velocity. Only vessel specifications and statistics resulting in relatively strong correlations are presented, however the results for any of the above listed parameters are available.

The VGW events of each parametric correlation are further organized by transit directions: inbound (red) and outbound (black). Splitting the events into the different transit directions was necessary due to the drastically variant wake behaviors observed during events from each direction (Section 5.1). Correlations for outbound events drastically underperformed those of inbound events to the extent that the following results discussion should be assumed as only pertaining to inbound events unless explicitly noted otherwise. The poor regression results of outbound events likely stem from the surface wave phase propagating as disorganized, broken waves as previously discussed.

5.2.1. Vessel Length

Figure 5.8 presents the correlations between hull length and the observed VGW event hydrodynamic statistics of total energy (panel A), significant wave height (B), u component max velocity magnitude (C), and v component max velocity magnitude (D). Hull length provided the most consistent R^2 regression agreement of any vessel parameter across multiple hydrodynamic statistics, including the best fits for total wake energy ($R^2 = 0.239$), significant wave height ($R^2 = 0.252$), max u velocity component magnitude ($R^2 = 0.374$), and max v velocity component magnitude ($R^2 = 0.153$) in particular.

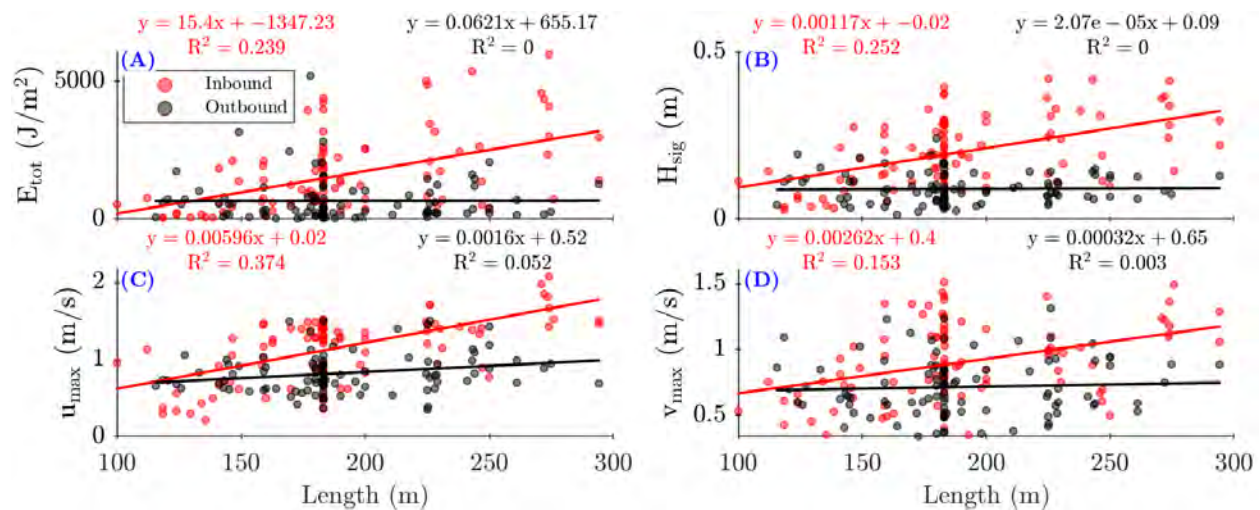


Figure 5.8: Correlations between the vessel length and hydrodynamic parameters total energy, significant wave height, max u velocity magnitude, and max v velocity magnitude (Panels A-D respectively). Inbound transits in red, outbound transits in black.

5.2.2. Vessel Draft

Hull drafts yielded the strongest correlation ($R^2 = 0.148$) to mean wave periods of any vessel parameter (Figure 5.9).

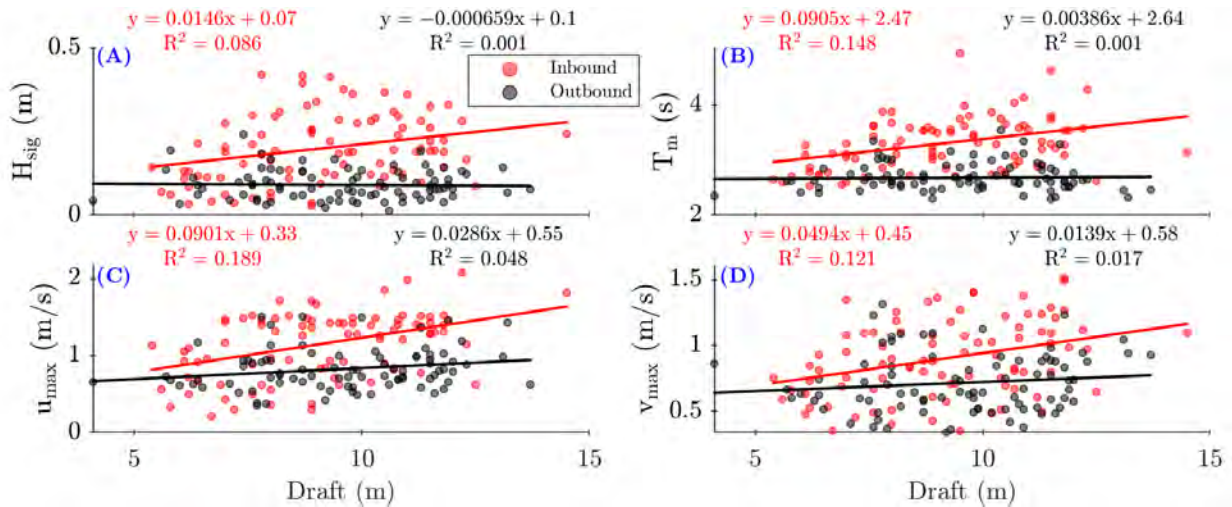


Figure 5.9: Correlations between the vessel draft and hydrodynamic parameters significant wave height, mean period of high frequency waves, max u velocity magnitude, and max v velocity magnitude (Panels A-D respectively). Inbound transits in red, outbound transits in black.

5.2.3. Vessel Summer Deadweight Tonnage

The summer deadweight tonnage values for each vessel provided strong correlations to significant wave height ($R^2 = 0.205$) and max u velocity component magnitude ($R^2 = 0.296$). Summer deadweight tonnage is a measure of how much weight a vessel can handle before the water line rises above the summer freeboard load line (Figure 5.10).

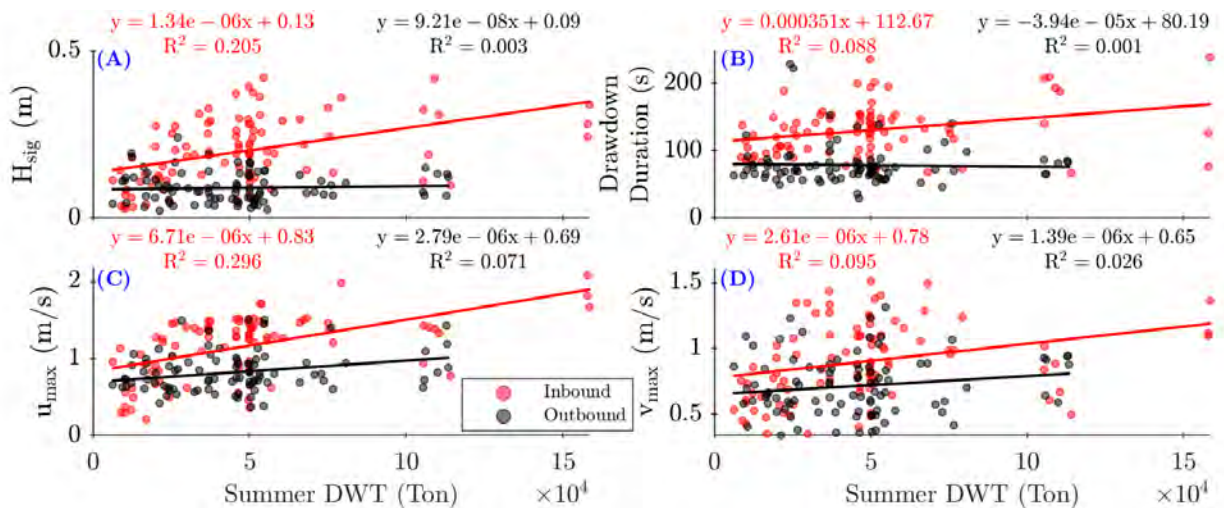


Figure 5.10: Correlations between the vessel Summer Deadweight Tonnage and hydrodynamic parameters significant wave height, drawdown duration, max u velocity magnitude, and max v velocity magnitude (Panels A-D respectively). Inbound transits in red, outbound transits in black.

5.2.4. Froude Numbers

Analyses for 3 different Froude number variants (1a, b, and d) were performed using an empirical parameter non-dimensionalized using wave height, vessel velocity, and gravitational force [Kriebel & Seelig, 2005]. The optimal form of the empirical parameter was investigated via usage of both significant wave height and max wave height in the formulation, yielding gH_{sig}/V_s^2 (Figure 5.11, left panel column) and gH_{max}/V_s^2 (Figure 5.11, right panel column).

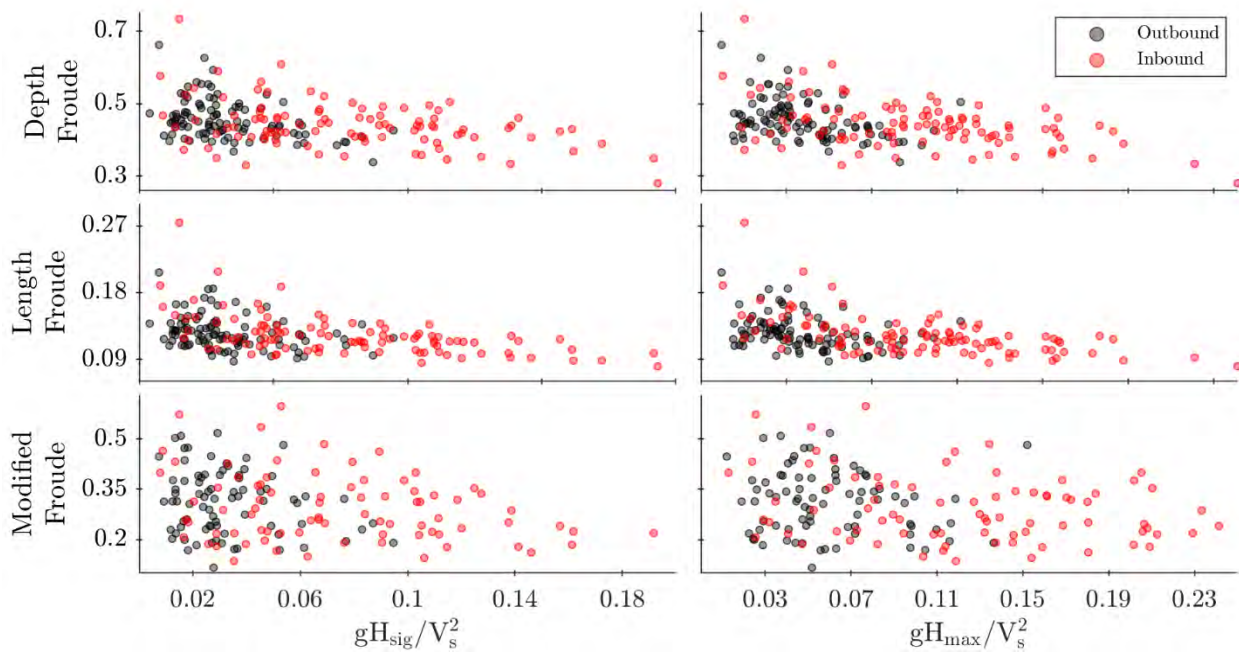


Figure 5.11: Dimensionless correlation between an empirical parameter gH/V^2 and 3 different Froude Number variants. The empirical parameter in the left column uses significant wave height while the right uses max wave height. Vessels organized by transit heading (red inbound, black outbound) and ship type (circles cargo, asterisks tanker).

As the results of the Froude number correlations were nonlinear, several best-fit functions were investigated to determine the optimal regression (Figure 5.12). The list of functions includes 1st and 2nd degree exponentials, a 2nd degree polynomial, and 1st and 2nd degree power functions. Table 5-9 to Table 5-11 summarize the results of each fit attempt.

Table 5-9: Best-fit regression results for the depth Froude number and empirical gH/V^2 parameter.

Depth Froude Number (Fr_h)				
Function	Inbound		Outbound	
	gH_{sig}/V_s^2	gH_{max}/V_s^2	gH_{sig}/V_s^2	gH_{max}/V_s^2
Exp1	0.16	0.22	0.12	0.11
Exp2	0.18	0.24	0.12	0.15
Poly2	0.16	0.23	0.12	0.12
Pow1	0.17	0.24	0.11	0.12
Pow2	0.17	0.24	0.12	0.14

Table 5-10: Best-fit regression results for the length Froude number and empirical gH/V^2 parameter.

Length Froude Number (Fr_l)				
Function	Inbound		Outbound	
	gH_{sig}/V_s^2	gH_{max}/V_s^2	gH_{sig}/V_s^2	gH_{max}/V_s^2
Exp1	0.37	0.41	0.08	0.10
Exp2	0.45	0.47	0.10	0.15
Poly2	0.41	0.46	0.10	0.14
Pow1	0.44	0.47	0.10	0.13
Pow2	0.44	0.47	0.12	0.15

Table 5-11: Best-fit regression results for the modified Froude number and empirical gH/V^2 parameter.

Modified Froude Number (Fr_m)				
Function	Inbound		Outbound	
	gH_{sig}/V_s^2	gH_{max}/V_s^2	gH_{sig}/V_s^2	gH_{max}/V_s^2
Exp1	0.22	0.18	0.04	0.03
Exp2	0.22	0.19	0.04	0.08
Poly2	0.22	0.19	0.04	0.04
Pow1	0.23	0.19	0.04	0.04
Pow2	0.23	0.19	0.05	0.05

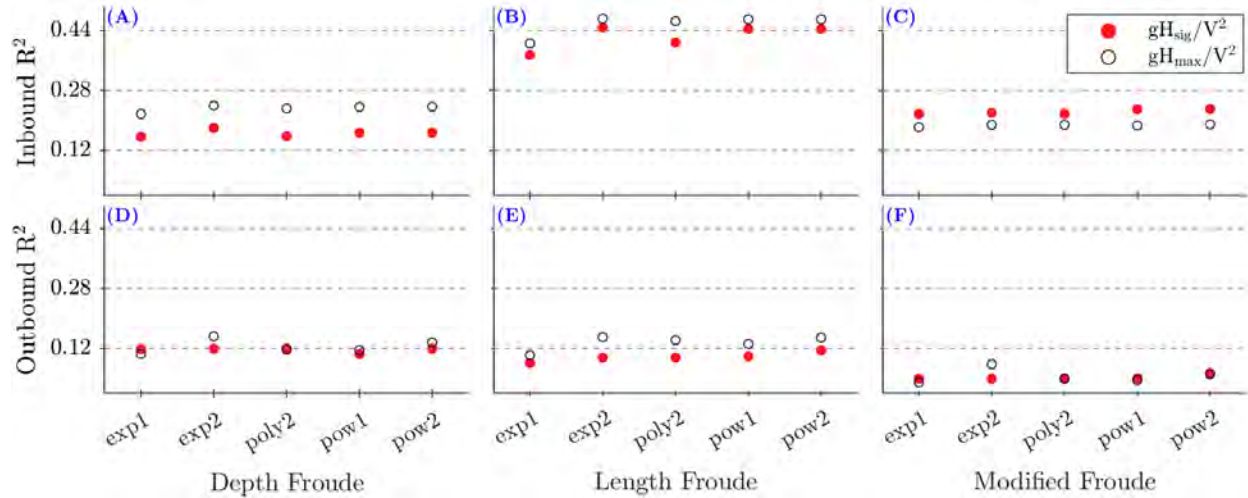


Figure 5.12: R^2 regression results for the correlations between Froude numbers and empirical gH/V^2 parameter organized by vessel heading directions and vessel types. Regression attempts included 1st and 2nd degree exponential fits, a 2nd degree polynomial fit, and 1st and 2nd degree power function fits.

Of the various attempts, the strongest regression correlation for inbound VGW events came from correlating the length Froude number with the gH_{max}/V_s^2 empirical coefficient using a 2nd degree exponential fit (Figure 5.12, panel B), resulting in an R^2 of 0.47 (Table 5-10). For the outbound VGW events, the strongest correlation was the combination of using the depth Froude number with the gH_{max}/V_s^2 empirical coefficient also using a 2nd degree exponential fit (Figure 5.12, panel D), giving an R^2 of 0.15 (Table 5-9). The equations for each of these regressions are given in (32a-b):

$$y = 0.09772 * \exp(-17.04x) + 0.1053 * \exp(-0.01656x) \quad (32a)$$

$$y = 0.5123 * \exp(-2.034x) + 1.436e - 9 * \exp(120.5x) \quad (32b)$$

5.2.5. General Discussion – Research Question 1

From the subset of bursts used in this analysis, attempts to link vessel parameters with measured wake event hydrodynamics resulted in moderately correlated inbound events at best. The vessel parameters providing the most useful correlations included hull length, hull draft, and the manufacturer designed summer deadweight tonnage. Table 5-12 summarizes these parameters along with the corresponding hydrodynamic statistics they correlate with and the associated coefficient of determination.

Although providing an R^2 of 0.47, the strongest regression coefficient found, results from the length Froude number and gH_{max}/V_s^2 correlation have the caveat of requiring measured wake data in order to achieve this relatively strong correlation value. The implication translates to this relationship likely presenting weaker correlations if wave heights are calculated empirically rather than from recorded hydrodynamic data, which is typically the case when studies are conducted using theoretical, forward-looking changes in vessel size or traffic patterns. A potential

addition to this segment of the correlation analysis is to perform several different methods for empirically estimating VGW event wave heights and determine how accurate the Froude number and estimated gH_{max}/V_s^2 correlation can be relative to the results from measured data.

Table 5-12: Summary of noteworthy correlations between vessel parameters and hydrodynamic statistics for wake events generated by inbound vessel transits.

Vessel Parameter (Inbound Transits)	Correlated Statistics		R ²
Hull Length	Total Wake Energy	E _{Tot}	0.239
	Significant Wave Height	H _{sig}	0.252
	Max Cross-shore Velocity Magnitude	u _{max}	0.374
	Max Longshore Velocity Magnitude	v _{max}	0.153
Hull Draft	Mean Wave Period	T _m	0.148
Summer Deadweight Tonnage	Significant Wave Height	H _{sig}	0.205
	Max Cross-shore Velocity Magnitude	u _{max}	0.296

5.3. Determining Wave-Condition Contributions Towards the Total Energy Budget

5.3.1. Wave Conditions Normalized as Max Total Energy Per Minute

Figure 5.13 illustrates the high frequency wave energies measured during inbound VGW events, outbound VGW events, and periods of only wind-driven wave action. Values are defined by calculating the maximum amount of wave energy summated over a 30-second window (top panel) and over a 2-minute window (bottom panel) during each event. These values are then normalized into an energy per minute timescale.

Table 5-13 lists the maximum and average energy found during full inbound and outbound VGW events, along with the resulting maximum energies per minute for all event types across both window durations.

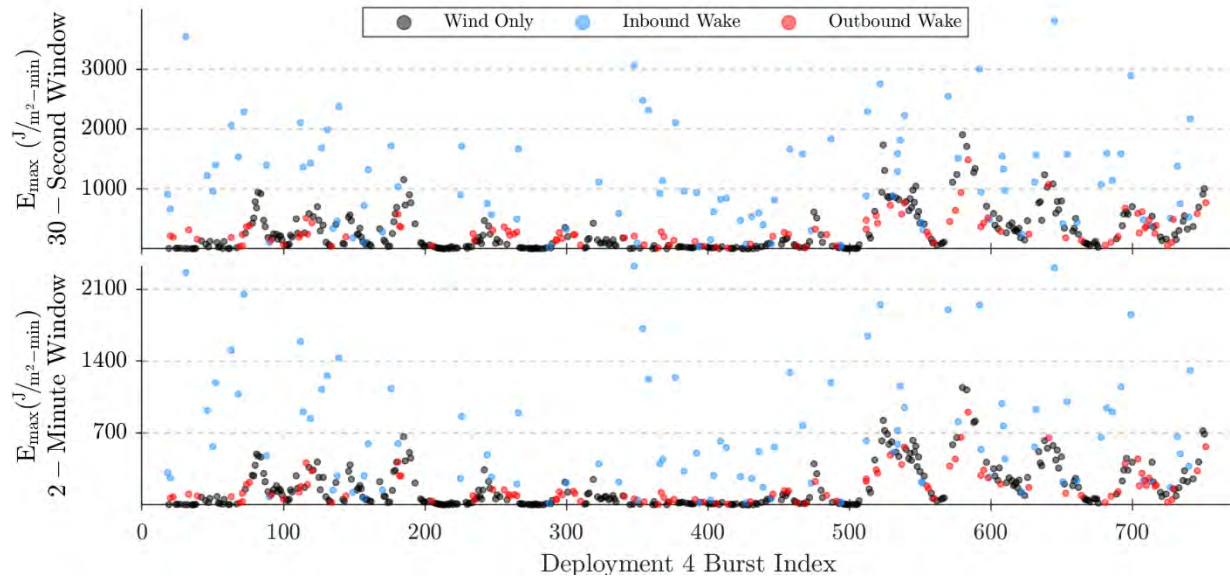


Figure 5.13: The maximum amount of wave energy measured during wind only (black), inbound wake events (blue), and outbound wake events (red) using a 30-second window (top panel) and 2-minute window (bottom panel). Wave energies are normalized into a per minute timescale.

Table 5-13: Summary of the maximum and average total wave energies found during full inbound and outbound wake events along with the maximum and average wave energy measured per inbound wake, outbound wake, and wind-only events using a 30-second and 2-minute window duration normalized into a per minute timescale.

Energy Statistic	Inbound VGW	Outbound VGW	Wind-Only	Unit
Max Total Event Energy	5,977	2,033	N/A	J/m^2
Average Total Event Energy	1,594	439	N/A	J/m^2
Max Energy per Minute with 30 Second Window	3,812	1,485	1,907	J/m^2min
Max Energy per Minute with 2 Minute Window	2,325	903	1,143	J/m^2min
Average Energy per Minute with 30 Second Window	1,158	301	265	J/m^2min
Average Energy per Minute with 2 Minute Window	702	179	164	J/m^2min

Figure 5.13 and Table 5-13 confirm that inbound VGW events contain a disproportionate amount of wave energy relative to outbound VGW events and periods of wind-only wave action. Inbound wake events are found to deliver a maximum total event energy 3 times larger than that of outbound events, as well as an average total event energy 5 times larger.

When considering the wave energy measured during 30-second and 2-minute periods, it can be seen that:

- Outbound VGW energies are closer in magnitude to wind-driven waves than inbound VGW events
 - Wind-driven max energies are about 25% stronger than outbound VGW max energies
 - Outbound VGW average energies are 10-15% stronger than wind-driven average energies
- Inbound VGW energies dominate the energy delivered per minute comparisons
 - Inbound VGW max energies are 2 times larger than wind or outbound VGW max energies
 - Inbound VGW average energies are 4 times larger than wind or outbound VGW average energy
 -

5.3.2. General Discussion – Research Question 2

Preliminary energy budget results shown in Figure 5.13 and Table 5-13 indicate a clear disparity between inbound VGW event wave energies relative to outbound VGW event or wind-driven wave energies. Outbound VGW events contain wave energy magnitudes approximately similar to non-wake conditions, likely due to the outbound surface waves propagating with broken waveforms as previously discussed.

High frequency wave energies are a primary source for sediment erosion at the site, however do not provide the complete picture on their own. Sediment entrainment by the “scraping” action of bed-level shear stresses during VGW drawdown phases must also be kept in mind; although the wave energies during outbound VGW and wind-wave events seem roughly equivalent, a greater sediment transport potential exists for outbound VGW events than for wind-only conditions. This greater potential is a direct consequence of the wake-generated surface waves arriving immediately after grain entrainment by the wake drawdown.

The final energy budget is expected to provide a total fractional summation for each wave condition (i.e., percent of the total wave energy that was recorded during inbound VGW events, outbound VGW events, and non-wake events). The remaining analysis component required to create this final energy budget summary is a more accurate delineation of whether a wake event is occurring at any given time, namely during periods of weak VGW effects, instances of incomplete wake event capture at the start or end of an ADCP burst cycle, or instances of interfering wakes from multiple ships.

6. ACKNOWLEDGMENTS

This study was supported in part by a collaborative research agreement between the Department of Defense/U.S. Army Corps of Engineers and Texas A&M University (No. W912 HZ-17-2-0023).

The contents of this report have been adapted from the M.Sc. thesis proposal document with the same title written by William P. Fuller.

7. REFERENCES

- Addison, P.S., (2017). "The Illustrated Wavelet Transform Handbook: Introductory Theory and Applications in Science, Engineering, Medicine, and Finance," 2nd ed. CRC Press, Boca Raton, FL., 446 p.
- Allenstrom, B., Andreasson, H., Leer-Andersen, M., and Da-Qing, L. (2003). "Amplification of ship generated wake wash due to coastal effects," Transactions of the Society of Naval Architects and Marine Engineers 111. pp 61-77.
- Bauer, B.O., Lorang, M.S., Sherman, D.J., (2002). "Estimating boat-wake-induced levee erosion using sediment suspension measurements," *Journal of Waterway, Port, Coastal, and Ocean Engineering* 128(4). pp 152–162.
- Becker, M., Schrottke, K., Bartholomä, A., Ernstsen, V., Winter, C., Hebbeln, D., 2013. Formation and entrainment of fluid mud layers in troughs of subtidal dunes in an estuarine turbidity zone: Dynamics of fluid mud in dune troughs. *Journal of Geophysical Research: Oceans* 118, 2175–2187.
- Bilkovic, D., Mitchell, M., Davis, J., Andrews, E., King, A., Mason, P., Herman, J., Tahvildari, N., Davis, J., (2017). "Review of boat wake wave impacts on shoreline erosion and potential solutions for the Chesapeake Bay," *STAC Publication* 17-002. Edgewater, MD. 68 p.
- Coifman, R.R. & Wickerhauser, M.V., (1992). "Entropy-based algorithms for best basis selection," *IEEE Transactions on Information Theory* 38(2). pp 713–718.
- Coifman, R.R., Meyer, Y., Quake, S., Wickerhauser, M.V., (1994). "Signal processing and compression with wavelet packets," *Wavelets and their Applications*, Proceedings of the NATO Advanced Study Institute on Wavelets and Their Applications, Italy, 1992. pp 363–379.
- Coops, H., Geilen, N., Verheij, H.J., Boeters, R., van der Velde, G., (1996). "Interactions between waves, bank erosion, and emergent vegetation: An experimental study in a wave tank," *Aquatic Botany* 53. pp 187-198.
- Daubechies, I., Grossman, A., Meyer, Y., (1986). "Painless non-orthogonal expansions," *Journal of Mathematics and Physics* 27. pp 1271-1283.
- Daubechies, I., (1988). "Orthonormal basis of compactly supported wavelets," *Communications on Pure and Applied Mathematics* 41. pp 909-996.
- Daubechies, I., (1990). "The wavelet transform time-frequency localization and signal analysis," *IEEE Transactions on Information Theory* 36(5). pp 961–1004.
- Daubechies, I., (1992). "Ten lectures on wavelets," *Wavelets and Their Applications*, Lecture given at the Conference Board of the Mathematical Sciences Conference on Wavelets and Their Applications, Regional Conference Series in Applied Mathematics. Lowell, MA, 1990.
- Donelan, M.A., Hamilton, J., Hui, W.H., (1985). "Directional spectra of wind-generated waves," *Philosophical Transactions of the Royal Society* 315. pp 509–562.

- Donelan, M.A., Drennan, W.M., Magnusson, A.K., (1996). "Nonstationary analysis of the directional properties of propagating waves," *Journal of Physical Oceanography* 26. pp 1901–1914.
- Donelan, M.A., (2002). "A new method for directional wave analysis based on wavelets," *Ocean Wave Measurement and Analysis 2001*. Presented at the Fourth International Symposium on Ocean Wave Measurement and Analysis, American Society of Civil Engineers, San Francisco, CA. pp 310–317.
- Donoho, D.L., & Johnstone, I.M., (1994). "Ideal spatial adaptation by wavelet shrinkage," *Biometrika* 81. pp 425–455.
- Elgar, S. & Raubenheimer, B., Guza, R.T., (2001). "Current meter performance in the surf zone," *Journal of Atmospheric and Oceanic Technology* 18. pp 1735–1746.
- Elgar, S., Raubenheimer, B., Guza, R.T., (2005). "Quality control of acoustic Doppler velocimeter data in the surfzone," *Measurement Science and Technology* 16. pp 1889–1893.
- Elgar, S. & Raubenheimer, B., (2008). "Wave dissipation by muddy seafloors," *Geophysical Research Letters* 35. 5 p.
- Elsayed, M., (2010). "An overview of wavelet analysis and its application to ocean wind waves," *Journal of Coastal Research* 26(3). pp 535–540.
- Engineering Research and Development Center (ERDC), (2019). "Engineering With Nature," Webpage. URL <https://ewn.el.erdcdren.mil/>
- Engineering Research and Development Center (ERDC), (1977). "Chapter 3.4: Wind Information Needed for Wave Prediction," *Shore Protection Manual*. Vol. 1, 3rd ed, U.S. Army Corps of Engineers Coastal Research Center, Vicksburg, MS. 541 p.
- Engineering Toolbox, (2003). "Specific Heat of Some Common Substances," Webpage. URL https://www.engineeringtoolbox.com/specific-heat-capacity-d_391.html
- Erikson, L., Larson, M., and Hanson, H., (2005). "Prediction of swash motion and run-up including the effects of swash interaction," *Coastal Engineering* 52. pp 285-302.
- Farge, M., (1992). "Wavelet Transforms and their applications to turbulence," *Annual Review of Fluid Mechanics* 24. pp 395–457.
- Feagin, R.A., Lozada-Bernard, S.M., Ravens, T.M., Moller, I., Yeager, K.M., Baird, A.H., (2009). "Does vegetation prevent wave erosion of salt marsh edges?" *Proceedings of the National Academy of Sciences* 106. pp 10109–10113.
- Fenical, S., Bermudez, H., Shepsis, V., Krams, D., Carangelo, P., (2001). "Vessel-generated long-wave measurement and prediction in Corpus Christi Ship Channel, TX," *Ocean Wave Measurement and Analysis 2001*. Presented at the Fourth International Symposium on Ocean Wave Measurement and Analysis, American Society of Civil Engineers, San Francisco, CA. pp 1634–1643.

- Fenical, S., MacDonald, N., and Yang, F., (2002). "Vessel Hydrodynamic Investigations," *Proceedings from the 1st Onshore and Offshore Pollution Prevention Symposium and Teaching Exhibition*. Long Beach, CA. 11 p.
- Fonseca, M.S. & Malhotra, A., (2012). "Boat wakes and their influence on erosion in Atlantic Intracoastal Waterway, North Carolina," *NOAA Technical Memorandum* No. NOS NCCOS #143. 24 p.
- Froude, W., (1874). "Experiments with H.M.S. Greyhound," *Transactions of the Society of Naval Architects and Marine Engineers* 15(1). pp 36-73.
- Froude, W., (1877). "Experiments upon the effect produced on the wave-making resistance of ships by length of parallel middle body," *Transactions of the Society of Naval Architects and Marine Engineers* 18. pp 77–87.
- Gabel, F., Lorenz, S., Stoll, S., (2017). "Effects of ship-induced waves on aquatic ecosystems," *Science of the Total Environment* 601-602. pp 926-939.
- Gamage, N.K.K., (1990). "Detection of coherent structures in shear induced turbulence using wavelet transform methods," *Ninth Symposium on Turbulence and Diffusion*, American Meteorological Society. pp 453-454.
- Gamage, N.K.K. & Hagelberg, C.R., (1993). "Detection and Analysis of Microfronts and Related Events," *Journal of the Atmospheric Sciences* 50(5). pp 750–756.
- Garel, E., Lopez-Fernandez, L., Collins, M., (2008). "Sediment resuspension events induced by the wake wash of deep-draft vessels." *Geo-Marine Letters* 28. pp 205-211.
- Gilmer, B. (2018). "Proximity Counts: How Houston Dominates the Oil Industry," *Forbes*, Webpage. URL <https://www.forbes.com/sites/uhenergy/2018/08/22/proximity-counts-how-houston-dominates-the-oil-industry/#7964a8261078>
- Grinsted, A., Moore, J.C., Jevrejeva, S., (2004). "Application of the cross wavelet transform and wavelet coherence to geophysical time series," *Nonlinear Processes in Geophysics* 11. European Geosciences Union. pp 561–566.
- Grossmann, A. & Morlet, J., (1984). "Decomposition of Hardy functions into square integrable wavelets of constant shape," *SIAM Journal on Mathematical Analysis* 15. pp 723–736.
- Grossman, A., Morlet, J., Paul, T., (1985). "Transforms associated to square integrable group representations," *Journal of Math and Physics* 26. pp 2473-2479.
- Grossman, A. & Morlet, J., (1985). "Decomposition of functions into wavelets of constant shape and related transforms," *Mathematics and Physics: Lectures on Recent Results*. pp 135-165.
- Hagelberg, C.R. & Gamage, N.K.K., (1994). "Structure-preserving wavelet decompositions of intermittent turbulence," *Boundary-Layer Meteorology* 70. pp 217–246.
- Hayter, E.J. & Mehta, A.J., (1982). "Modeling of estuarial fine sediment transport for tracking pollutant movement", Corvallis Environmental Research Laboratory & Univ. of Florida Dept. Coastal Oceanographic Engineering, Gainesville, FL, 205 p.

- Hayter, E.J. & Mehta, A.J. (1986). "Modelling Cohesive Sediment Transport in Estuarial Waters," *Applied Mathematical Modelling* 10. pp 294–303.
- Havelock, T.H., (1908). "The propagation of groups of waves in dispersive media, with application to waves on water," *Proceedings of the Royal Society* 81. pp 398–430.
- Henry, W.K. (1979). "Some Aspects of the Fate of Cold Fronts in the Gulf of Mexico," *Monthly Weather Review, Notes and Correspondence* 107. pp 1078–1082.
- Herbich, J.B. & Schiller Jr., R.E. (1984). "Surges and waves generated by ships in a constricted channel," *Coastal Engineering Proceedings 1984*. pp 3212–3226.
- Houser, C., (2010). "Relative importance of vessel-generated and wind waves to salt marsh erosion in a restricted fetch environment," *Journal of Coastal Research* 26(2). pp 230–240.
- International Maritime Organization (IMO), (2019). "AIS Transponders," Webpage. URL <https://www.imo.org/en/OurWork/Safety/Pages/AIS.aspx>
- Jensen, R.E., (1985). "Shallow-water spectral wave modeling," *Coastal Engineering* 1984. Presented at the 19th International Conference on Coastal Engineering, American Society of Civil Engineers, Houston, TX. pp. 547–560.
- Kaiser, G., (1994). "A Friendly Guide to Wavelets," Birkhäuser. 300 p.
- Kevlahan, N.K.-R., Dubos, T., Aechtner, M., (2015). "Adaptive wavelet simulation of global ocean dynamics," *Geoscientific Model Development Discussions* 8(7). pp 5265–5313.
- Kocen, M., (2013). "Observations of Sea-Breeze Fronts Along the Houston Gulf Coast," Master of Science Thesis for the Department of Earth and Atmospheric Science, University of Houston. 76 pp.
- Kriebel, D.L. & Seelig, W.N., (2005). "An empirical model for ship-generated waves," *Proceedings of the 5th International Symposium on Ocean Wave Measurement and Analysis*, Madrid, Spain. 19 p.
- Knutson, P.L., Ford, J.C., Inskeep, M.R., Oyler, J., (1981). "National survey of planted salt marshes," *Wetlands* 1(1). pp 129–157.
- Krone, R.B., (1962). "Flume studies of the transport of sediment in estuarial shoaling processes: Final Report," Report prepared for San Francisco District Corps of Engineers. Hydraulic Engineering Laboratory, Univ. of California Berkley. 129 p.
- Krone, R.B., (1978). "Aggregation of suspended particles in estuaries," *Estuarine Transport Processes* 7. Belle W. Baruch Library in Marine Science, Univ. of South Carolina Press, Columbia, SC. pp 177–190.
- Kumar, P. & Foufoula-Georgiou, E., (1997). "Wavelet analysis for geophysical applications," *Reviews of Geophysics* 35(4), American Geophysical Union. pp 385–412.
- Liu, P.C., (1994). "Wavelet Spectrum Analysis and Ocean Wind Waves," *Wavelets in Geophysics, Wavelet Analysis and Its Applications* 4. pp 151–166.

- Mallat, S.G., (1989a) "Multiresolution approximation and wavelet orthonormal bases of $L^2(\mathbb{R})$," *Transactions of the American Mathematical Society* 315(1). pp 69-88.
- Mallat, S.G., (1989b). "A theory for multiresolution signal decomposition: the wavelet representation," *IEEE Transactions on Pattern Analysis and Machine Intelligence* 11(7). pp 674–693.
- MarineTraffic, (2019). "How often do the positions of the vessels get updated on MarineTraffic?" Webpage. URL <https://help.marinetraffic.com/hc/en-us/articles/217631867-How-often-do-the-positions-of-the-vessels-get-updated-on-MarineTraffic->
- Massel, S.R., (2001). "Wavelet Analysis for Processing of Ocean Surface Wave Records," *Ocean Engineering* 28. pp 957–987.
- Maynard, S.T. (2001). "Boat waves on Johnson Lake and Kenai River, Alaska," *Coastal and Hydraulics Engineering Technical Note TR-01-31*, Coastal Hydraulics Lab, U.S. Army Corps of Engineers Engineer Research and Development Center. Vicksburg, MS. 148 p.
- Maynard, S.T., (2005). "Wave height from planing and semi-planing small boats," *River Research and Applications* 21. pp 1–17.
- McAnally, W.H. & Mehta, A.J., (2002). "Significance of aggregation of fine sediment particles in their deposition." *Estuarine, Coastal and Shelf Science* 54. pp 643–653.
- McConchie, J.A. & Toleman, I.E.J., (2003). "Boat wakes as a cause of riverbank erosion: a case study from the Waikato River, New Zealand," *Journal of Hydrology* 42(2). pp 163-179.
- Mehta, A.J., Parchure, T.M., Dixit, J.G., Ariathurai, R., (1982). "Resuspension potential of deposited cohesive sediment beds," *Estuarine Comparisons: Proceedings of the sixth biennial international Estuarine Research Conference*. Gleneden Beach, OR. pp 591-609.
- Mehta, A.J., Barber, R.T., Mooers, C.N.K., Bowman, M.J., (1986). "Estuarine cohesive sediment dynamics," *Lecture Notes on Coastal and Estuarine Studies* 14. Springer. 473 p.
- Meyer, Y. (1989). "Orthonormal Wavelets," *Wavelets, Inverse Problems and Theoretical Imaging Series*. Springer. pp 21-37.
- Meyer, Y.F., (1990). "Wavelets and Applications," *Proceedings of the International Congress of Mathematicians*. pp 1619–1626.
- Meyers, S.D., Kelly, B.G., O'Brien, J.J., (1993). "An Introduction to Wavelet Analysis in Oceanography and Meteorology: With Application to the Dispersion of Yanai Waves," *Monthly Weather Review* 121. pp 2858–2866.
- Morlet, J., Arens, G., Fourgeau, I., Giard, D., (1982). "Wave propagation and sampling theory," *Geophysics* 47. pp 203-236.
- Nairn, R.B. & Willis, D.H., (2002). "Chapter III-5 Erosion, Transport, and Deposition of Cohesive Sediments," *Coastal Engineering Manual*. U.S. Army Corps of Engineers Coastal Research Center, Vicksburg, MS. 67 p.

- NOAA, (1989). "Galveston Bay: Issues, Resources, Status, and Management," NOAA Estuary-of-the-Month Seminar Series No. 13, NOAA Estuarine Programs Office. U.S. Department of Commerce. 114 p.
- NOAA, (2019a). "El Nino & La Nina (El Nino-Southern Oscillation)," Webpage. URL <https://www.climate.gov/enso>
- NOAA, (2019b). "El Nino-Southern Oscillation Cold & Warm Episodes by Season," Webpage. URL https://origin.cpc.ncep.noaa.gov/products/analysis_monitoring/ensostuff/ONI_v5.php
- Nortek, (2008a). "Aquadopp Current Profiler User Manual," Nortek Doc. No. N3009-103 Revision C. 83 p.
- Nortek, (2008b). "Aquadopp HR Current Profiler User Manual," Nortek Doc. No. AHR00-0101-0508. 39 p.
- Nortek, (2019). "How is SNR given in Storm?" Nortek Support Center Online FAQ, Webpage. URL <https://support.nortekgroup.com/hc/en-us/articles/360029829711-How-is-SNR-given-in-Storm->
- Partheniades, E., (1962). "A Study of Erosion and Deposition of Cohesive Soils in Salt Water," Doctoral dissertation for the University of California, Berkely.
- Percival, D.B., & Guttorp, P., (1994). "Long-memory processes, the Allan variance and wavelets," *Wavelets in Geophysics*. pp 325- 344.
- Percival, D.P., (1995). "On estimation of the wavelet variance," *Biometrika* 82(3). pp 619–631.
- Percival, D.P. & Mofjeld, H.O., (1997). "Analysis of subtidal coastal sea level fluctuations using Wavelets," *Journal of the American Statistical Association* 92(439). pp 868–880.
- PIANC, (2018). "Guide for applying working with nature to navigation infrastructure projects," *Environmental Commission* Report No. 176. World Association for Waterborne Transport Infrastructure, Brussels, Belgium. 100 p.
- Port of Houston, (2018). "Port Statistics," Webpage. URL <https://porthouston.com/about-us/statistics/>
- Ravens, T.M., & Thomas, R.C., (2008). "Ship wave-induced sedimentation of a tidal creek in Galveston Bay," *Journal of Waterway, Port, Coastal, and Ocean Engineering* 134. pp 21–29.
- Rayson, M.D., Gross, E.S., Fringer, O.B., (2015). "Modeling the Tidal and Sub-Tidal Hydrodynamics in a Shallow, Micro-Tidal Estuary," *Ocean Modelling* 89, pp 29–44.
- rssWeather, (2013). "Climate for Houston, Texas," Webpage. URL <https://www.rssweather.com/climate/Texas/Houston/>
- Sanford, L.P. & Halka, J.P., (1993). "Assessing the paradigm of mutually exclusive erosion and deposition of mud, with examples from upper Chesapeake Bay," *Marine Geology* 114. pp 37–57.

- Schroeder, M.J. & Buck, C.C., (1970). "A Guide for Application of Meteorological Information to Forest Fire Control Operations," U.S. Department of Agriculture Forest Service Handbook 360, Webpage. URL <https://www.nwcg.gov/publications/pms425-1/air-masses-and-fronts>
- Shafer, D.J. & Streever, W.J., (2000). "A comparison of 28 natural and dredged material salt marshes in Texas with emphasis on geomorphological variables," *Wetlands Ecology and Management* 8. pp 353–366.
- Shafer, D.J., Roland, R., Douglass, S.L., (2003). "Preliminary evaluation of critical wave energy thresholds at natural and created coastal wetlands," *Engineering Technical Note* No. TN-WRP-HS-CP-2.2. U.S. Army Corps of Engineers Engineer Research and Development Center, Vicksburg, MS. 12 p.
- Scully, B.M. & McCartney, A.C., (2017). "Use of AIS and AISAP for analysis of vessel wakes in Charleston Harbor: A case study," *Coastal and Hydraulics Engineering Technical Note CHETN-IX-46*, Coastal Hydraulics Lab, U.S. Army Corps of Engineers Engineer Research and Development Center. Vicksburg, MS. 11 p.
- Soomere, T., (2007). "Nonlinear Components of Ship Wake Waves," *Applied Mechanics Reviews* 60. pp 120-137.
- Sorensen, R.M., (1973). "Ship-generated waves," *Advances in Hydrosience* 9. pp 49-83.
- Sorensen, R.M. & Weggel, J.R., (1985). "Development of ship wave design information," *Coastal Engineering* 1984. Presented at the 19th International Conference on Coastal Engineering, American Society of Civil Engineers, Houston, TX. pp. 3227-3243.
- Sorensen, R.M., (1997). "Prediction of vessel-generated waves with reference to vessels common to the Upper Mississippi River system," *ENV Report 4*, Prepared for the Rock Island, St. Louis, and St. Paul U.S. Army Engineer Districts. 50 p.
- Stumbo, S. & Fox, K., (1998). "Prediction, measurement, and analysis of wake wash from marine vessels," *Marine Tech* 36. pp 248-260.
- Tate, J.N. & Berger, R.C., (2006). "Houston-Galveston Navigation Channels, Texas Project: Navigation Channel Sedimentation Study, Phase 1," Report No. ERDC/CHL TR-06-8. Coastal Hydraulics Lab, U.S. Army Corps of Engineers Engineer Research and Development Center, Vicksburg, MS. 126 p.
- Tate, J.N., Berger, R.C., Ross, C.G., (2008). "Houston-Galveston Navigation Channels, Texas Project: Navigation Channel Sedimentation Study, Phase 2," Report No. ERDC/CHL TR-08-8. Coastal Hydraulics Lab, U.S. Army Corps of Engineers Engineer Research and Development Center, Vicksburg, MS. 183 p.
- Tchamitchian, P. & Torr sani, B., (1991). "Ridge and skeleton extraction from the wavelet transform," *Wavelets and their Applications*, Lecture given at the Conference Board of the Mathematical Sciences Conference on Wavelets and Their Applications, Regional Conference Series in Applied Mathematics. Lowell, MA, 1990. 16 p.
- Thomson, W. (Lord Kelvin), (1887). "On ship waves," *Transactions of the Institute of Mechanical Engineers* 8. pp 409–433.

- Todd, F.H., (1967). "Resistance and propulsion," *Principles of Naval Architecture*, Society of Naval Architects and Marine Engineers. Chapter 7.
- Tonelli, M., Fagherazzi, S., Petti, M., (2010). "Modeling wave impact on salt marsh boundaries," *Journal of Geophysical Research* 115. 17 p.
- Torrence, C. & Compo, G.P., (1998). "A practical guide to Wavelet analysis," *American Meteorological Society* 79(1). pp 61–78.
- Torsvik, T., Dysthe, K., Pedersen, G., (2006). "Influence of variable Froude number on waves generated by ships in shallow water," *Physics of Fluids* 18. 11 p.
- Torsvik, T. & Soomere, T., (2008). "Simulation of patterns of wakes from high-speed ferries in Tallinn Bay," *Estonian Journal of Engineering* 14(3). pp 232-254.
- Torsvik, T., Soomere, T., Didenkulova, I., Sheremet, A., (2015). "Identification of ship wake structures by a time-frequency method," *Journal of Fluid Mechanics* 765. pp 229-251.
- United Nations (UN) (2017). "Review of Maritime Transport," *United Nations Conference on Trade and Development*. United Nations Publications. 114 p.
- United States Coast Guard (USCG), (2019). "AIS Frequently Asked Questions," United States Coast Guard Navigation Center, Department of Homeland Security, Alexandria, VA. Webpage. URL <https://www.navcen.uscg.gov/?pageName=AISFAQ>
- Velegrakis, A.F., Vousdoukas, M.I., Vagenas, A.M., Karambas, T., Dimou, K., Zarkadas, T., (2007). "Field observations of waves generated by passing ships: A note," *Coastal Engineering* 54. pp 369-375.
- Weggel, J.R. & Sorensen, R.M., (1986). "Ship Wave Prediction for Port and Channel Design," *Proceedings of the Ports '86*, ASCE Specialty Conference. Oakland, CA. pp 797-814.
- Wickerhauser, M.V., (1993). "Best adapted wave packet bases," *Different Perspectives on Wavelets: Proceedings of Symposia in Applied Mathematics* 47, American Mathematical Society. pp 155-171.
- Winterwerp, J.C. and Kranenburg, C. (1997). "Erosion of fluid mud layers II: Experiments and model validation," *Journal of Hydraulic Engineering* 123(6). pp 512-519.
- Winterwerp, J.C. and van Kesteren, W.G.M. (2004). "Introduction to the Physics of Cohesive Sediment Dynamics in the Marine Environment," *Developments in Sedimentology* 56. Elsevier, Amsterdam; Boston. 429 pp.
- Winterwerp, J.C., (2007). "On the sedimentation rate of cohesive sediment," *7th International Conference on Estuarine and Coastal Fine Sediments Dynamics*. Gloucester Point, VA, USA, Elsevier. pp 209–226.
- Wolanski, E., Chappell, J., Ridd, P., Vertessy, R., (1988). "Fluidization of mud in estuaries," *Journal of Geophysical Research* 93. pp2351–2361.